

THE DEVELOPMENT OF AN AUTONOMOUS ROBOTIC INSPECTION SYSTEM TO DETECT AND CHARACTERISE ROLLING CONTACT FATIGUE CRACKS IN RAILWAY TRACK

by

HAMED ROWSHANDEL

A thesis submitted to
The University of Birmingham
for the degree of
DOCTOR OF PHILOSOPHY

College of Engineering and Physical Sciences
School of Electronic, Electrical and Computer Engineering
University of Birmingham
September 2013

UNIVERSITY OF
BIRMINGHAM

University of Birmingham Research Archive

e-theses repository

This unpublished thesis/dissertation is copyright of the author and/or third parties. The intellectual property rights of the author or third parties in respect of this work are as defined by The Copyright Designs and Patents Act 1988 or as modified by any successor legislation.

Any use made of information contained in this thesis/dissertation must be in accordance with that legislation and must be properly acknowledged. Further distribution or reproduction in any format is prohibited without the permission of the copyright holder.

Abstract

To meet the demands of higher speed and greater axle load of trains on busy tracks, the current rail track inspection procedures across Europe need to be improved in order to minimise disruption and enhance reliability. At present, high speed dual purpose rail/road vehicles employing fixed non-destructive testing (NDT) sensors are used to inspect rails. Due to the uncertainties in characterisation of the defects when they are detected at high speed, manual re-visiting of the defects by expert operators is required before any decision regarding track maintenance is made. This research has been driven by a desire from the rail industry for a robotic system performing faster than human operators and being capable to both detect and characterise rolling contact fatigue (RCF) cracks in rails with the aim of automating the existing manual inspection and enhancing its accuracy and reliability.

This thesis combines expert systems technologies with robotic NDT to fulfil this aspiration. A great deal of effort has been spent to develop a robotic inspection trolley which can automatically detect and characterise the RCF cracks in rails using an alternating current field measurement (ACFM) sensor. It uses a rule based expert system (RBES) proposed to control the robotic trolley and more importantly process ACFM data for both detecting and sizing defects. The developed system can detect the possible presence of defects in railway tracks at high speed pass (5-20 km/h) and can automatically return to an identified defect location to perform a slower and more detailed scan (up to 20 mm/s) across a rail section to determine the size, depth and number of cracks present in that section. A novel method has been proposed which can detect both isolated and clustered RCF cracks from high speed

ACFM scans with a high probability of detection even in the presence of process noise and severe sensor lift-off change. The system was evaluated using several laboratory and field trials where many artificial and real isolated/clustered RCF cracks were studied. The trials included both static and dynamic case where the former was used to assess the performance of the robotic system in sizing defects when their locations are known while the latter was used to determine the performance of defect detection and accuracy of the system in travelling to a given defect location. In doing so, various factors that affect determination of an unknown defect (e.g. position with respect to gauge side, length, surface orientation and unpredicted rail wear) were studied. The results of static and dynamic measurements suggest that the developed robotic system has high reliability (detection probability > 90%) and accuracy (characterisation error < 20%) in automatically detecting and characterising the RCF defects, therefore, has the potential to replace the manual inspection.

تقدیم بہ

مادر، پدر و ہمسرم کہ بدون وجود آنها انجام این کار میسر نبود

Acknowledgments

Firstly, my sincere gratitude goes to my research supervisors for provision of scholarship towards tuition fees and most importantly, constructive technical advice during the course of my PhD; Professor Clive Roberts for his unwavering optimism, believing in me, support and effort in making the Birmingham Railway Research Centre a friendly atmosphere by organising many social events, Professor Claire Davis for her availability and passion in dealing with my research which helped me remain motivated throughout the course.

Secondly, I am indebted to Dr Gemma Nicholson for her friendly attitude, generosity in sharing her valuable knowledge and support with my research which were quite crucial to my success.

I am also grateful to Dr Mayorkinos Papaelias for sharing his experimental data and assistance with field trials which enabled me to complete this work.

Equally, I am thankful to Mr Adnan Zentani for his friendly manner, assistance in facilitating my research, intensive lab work and field tests during my research.

I am most sincerely obliged to my wife, Sara, for her love, understanding, caring and tolerance throughout my research despite all the sacrifices. Likewise, I am indebted to my parents for their heartfelt support, positive thoughts and prayers towards my success all along.

Last but not least, I should like to thank the many friends whom I encountered en route to this juncture for their support and friendship.

Table of Contents

Chapter 1. Introduction	1
1.1. Background	1
1.2. Motivation.....	3
1.3. Aims and Objectives.....	5
1.4. Contributions	6
1.4.1. Hardware and Software Development	6
1.4.2. Novel Contributions	7
1.5. Thesis Structure	9
Chapter 2. Literature Review	11
2.1. Introduction	11
2.2. Rail Defects	11
2.2.1. RCF Cracks.....	14
2.3. NDT Methods in the Railway Industry	16
2.3.1. Visual Inspection	16
2.3.2. Ultrasonic Transducers	18
2.3.3. Laser Ultrasound	20
2.3.4. Electromagnetic Acoustic Transducers	21
2.3.5. Long-range Ultrasound	22
2.3.6. Eddy Currents.....	24
2.3.7. Magnetic Flux Leakage.....	27
2.3.8. Alternating Current Field Measurement.....	30
2.4. Robotic NDT	42

2.5. Summary	48
Chapter 3. Development of a Robotic System for Inspection of RCF Cracks in Rails	50
3.1. Introduction	50
3.2. Rule-Based Expert System	51
3.3. Software/Hardware Developments and Methods	52
3.3.1. Robot Arm Agent	56
3.3.2. ACFM Sensor Agent	61
3.3.3. Laser Sensor Agent.....	63
3.3.4. Motion Controller Agent.....	65
3.4. Functionalities of the Developed Robotic System	70
3.4.1. Calibration.....	70
3.4.2. Profile Measurement	73
3.4.3. RCF Crack Characterisation	78
3.4.4. RCF Crack Detection.....	83
3.5. Summary	85
Chapter 4. Case Study: Static Results	87
4.1. Introduction	87
4.2. Experimental Setup.....	87
4.3. Results.....	89
4.3.1. Matching Probe Angle	89
4.3.2. Non-matching Probe Angle.....	96
4.3.3. Effect of Grid Spacing.....	102
4.3.4. Effect of ACFM Sensor Lift-off and Signal to Noise Ratio.....	104
4.4. Summary	107

Chapter 5. Case Study: using the Robotic System for Automatic Detection and Characterisation of RCF Cracks.....	108
5.1. Introduction	108
5.2. CTSM Algorithm	109
5.2.1. Avoidance of Local Minima Traps	114
5.3. Experimental Setup.....	116
5.4. Results.....	118
5.4.1. Low-speed Detection Scans using the Robotic Trolley	118
5.4.2. High-speed Detection Scans using Rotary Rail Rig	124
5.4.3. Automatic Characterisation using the Robotic System.....	130
5.5. Summary	133
Chapter 6. Case Study: Extension of the CTSM Algorithm for Automatic Detection of Multiple-RCF Cracks.....	134
6.1. Introduction	134
6.2. ACFM Response to Multiple-RCF Cracks.....	134
6.3. Extended CTSM Algorithm	136
6.4. Results.....	138
6.4.1. Automatic Detection from Simulated ACFM Response to Multiple-RCF Cracks.....	138
6.4.2. Automatic Detection from Experimental ACFM Response to Multiple-RCF Cracks	143
6.5. Summary	148
Chapter 7. Conclusions and Future Work	149
7.1. Conclusions	149
7.2. Achievements and Key Findings	149
7.2.1. Case Study 1.....	149
7.2.2. Case Study 2.....	151
7.2.3. Case Study 3.....	154

7.3. Future Work and Recommendations.....	155
7.3.1. Hardware Enhancements.....	155
7.3.2. Software Enhancements.....	156
References	157
Publications	169
Appendix. Screenshot of the IUI Software.....	170

List of Figures

Figure 1.1 Standard rail track speed-tonnage curve used in the UK [5].	2
Figure 1.2 (a) Manual inspection of rail using ACFM walking stick [6] and (b) portable ultrasonic flaw detector [7].	4
Figure 2.1 Tache ovale or 'kidney' rail failure [2].	12
Figure 2.2 Surface spalling of the rail surface caused by wheelburn [2].	12
Figure 2.3 Examples of RCF cracks: (a), (b) & (c) head checking (gauge corner cracking) and (d) squats [2, 11].	13
Figure 2.4 Railtrack (now Network Rail, GB) RCF crack visual length/depth guidance [12].	14
Figure 2.5 Experimental setup for automated VI used by Qingyong, et al. [18].	17
Figure 2.6 The two basic methods of transmitting and receiving ultrasound:(a) pitch-catch (separate transducers) and (b) pulse-echo (single transducer) [22].	19
Figure 2.7 Illustration of the operation of the eddy current testing; (a) variation of the receiving coil's resultant impedance in the presence of a defect (horizontal and vertical axis display the coil resistance and impedance, respectively) (b) the distribution of EC on the surface of a specimen [37].	25
Figure 2.8 Principle of operation of MFL method used for pipeline inspection [48].	28
Figure 2.9 Simulation result of magnetic flux response to a rectangular slot at different probe speeds [49].	29
Figure 2.10 Illustration of the ACFM principle [53]. The eddy currents pass around the crack ends and down the faces of the crack opening. The graphs correspond to a 1D scan along the crack length. ...	31
Figure 2.11 Illustration of ACFM signal inversion using table interpolation.	35
Figure 2.12 Variations of the real part of the crack signals, $H_{c,x}$ superposed by additive white Gaussian noise with various SNRs when scanning the cracks along $y_s = 0.5$ mm at lift-off distance $z_s = 0.1$ mm for (a) Rectangular depth profile (b) Triangular depth profile (c) Symmetrical triple-hump depth profile and (d) Asymmetrical triple-hump depth profile [62].	36
Figure 2.13 Normalized maximum change in B_x value against crack surface length at zero lift-off for semi-elliptical cracks of elliptical ratios 1:1, 1.25:1, 1.5:1 and 1.75:1 [3].	38

Figure 2.14 The sensitivity of the maximum change in Bx value at zero lift-off to changes in the orientation of the ACFM probe relative to surface crack angle for a 15 mm surface length, 5 mm pocket length semi ellipse [65].....	39
Figure 2.15 Image of the Bombardier and TSC ACFM walking stick [66].....	39
Figure 2.16 Experimental setup for the turning lathe tests using the rotary test piece [54].....	40
Figure 2.17 ACFM data plots showing the resulting signals at 20.25 and 121.5 km/h with 0.8 mm lift-off. The different signals (magnitude of A/D conversion signal change) are for machined defects of 4 mm and 2 mm depth [54].....	40
Figure 2.18 Experimental setup during the spinning rail rig tests [54].....	42
Figure 2.19 Raw and normalized filtered data plots for test rails where the 5, 10 and 15 mm spacing refers to the distance between each defect for clusters of three defects of varying depth (2, 4, 10 mm) [54]. The defects used in this experiment are later explained in Chapter 5 (Figure 5.11).....	42
Figure 2.20 Pipeline inspection robot using a UT sensor adapting to different configurations: (a) elbow and (b) branch [84].....	43
Figure 2.21 Automatic monitoring of weld quality using the EMAT technique [85].....	44
Figure 2.22 Underwater robotic system using an ACFM array probe developed by Sattar, et al. [77].	45
Figure 2.23 (a) Demonstration of the ring climbing robot prototype used for inspection of wind turbine blades (b) Conceptual design for full scale climbing robot that takes tomographic scans by using rotation capability of the turbine blade along its long axis [78].	46
Figure 2.24 Graphical illustration of automatic ACFM scan for crack sizing.	48
Figure 3.1 Structure of a rule-based expert system [92].....	52
Figure 3.2 Screenshot of the developed IUI software. Labels: 1→ explanation facility, 2→ function for aligning the robot's tool centre point with the global coordinate system (manual mode), 3→ function for moving the tool centre point to a predetermined reference point (manual mode), 4→ function for setting the current location as a reference point (manual mode), 5→ functions for changing the alignment of the robot's tool centre point relative to its current pose defined by three rotational components (manual mode), 6→ function for translating the tool centre point relative to its current location defined by three linear components (manual mode), 7-11→ see Appendix, 12→ function for switching between manual and automatic mode, 13→ function for measuring the rail head profile (manual & automatic), 14→ function for performing a 3D ACFM grid scan following the rail head profile at a constant lift-off (manual & automatic), 15→ function for performing an ACFM detection scan along a rail at a constant speed using the motorised trolley (automatic mode).....	53
Figure 3.3 Image of the developed robotic trolley at the University of Birmingham. Labels: 1→ Motion Controller Agent, 2→ Robot Arm Agent, 3→ ACFM Sensor Agent, 4→ Laser Sensor Agent, 5→ IUI Software.	54

Figure 3.4 The block diagram representation of the IUI software communicating with the sensor and actuator agents. RS232 is the standard protocol used for serial communication with a PC.	54
Figure 3.5 Illustration of the Kawasaki FS02N robot arm and its coordinate system.	58
Figure 3.6 Illustration of compound transformation.	59
Figure 3.7 Graphical representation of the ACFM probe's conditions being: (a) normal to rail surface and (b) parallel to the crack opening.	59
Figure 3.8 (a) The ACFM 5 kHz micro pencil probe and (b) the ACFM AMIGO instrument [99].	62
Figure 3.9 Image of the Micro-Epsilon ILD 1302-20 laser triangulation displacement sensor [106]. ...	64
Figure 3.10 Illustration of the motion controller agent and its components. Labels: 1→ Developed position/speed controller, 2→ position feedback signal from odometer, 3→ RS232 serial I/O port, 4→ Analogue output, 5→ emergency stop signal, 6→ ABB VFD inverter, 7→ three-phase AC motor used to propel the trolley.	65
Figure 3.11 Block diagram of the closed loop motion controller agent.	66
Figure 3.12 Quadrature encoder interface signals [108].	67
Figure 3.13 Flow chart demonstration of the control sequences implemented on the microcontroller running at 20 MHz (using external clock).	69
Figure 3.14 Two-point based calibration approach for the orientation angle. The robot's tool angle for points P2 and P3 has been set to -90° to make the laser sensor face the field side of the rail.	71
Figure 3.15 Two-point based calibration approach for the attitude angle.	71
Figure 3.16 Process flow chart representation of the "Calibrate" function in the IUI.	72
Figure 3.17 Rail head profile of in-service rails (BS113A) subject to different amount of wear. Rail A represents a new rail.	73
Figure 3.18 Process flow chart representation of the "MeasureProfile" function in the IUI.	74
Figure 3.19 Comparison between the robot and MiniProf measurement on UIC54 rail.	74
Figure 3.20 Demonstration of a 16 th degree polynomial fitted to the measured rail profile.	77
Figure 3.21 Plot of standard deviation of residuals against order of polynomial.	77
Figure 3.22 Comparison between the numerical and analytical approach for calculating the ACFM probe's tangent angle t	77

Figure 3.23 Illustration of the scan region on the rail profile. Labels: 1→ start of recording, 2→ end of recording. 78

Figure 3.24 The process flow diagram of the “RScan” function in the IUI. 79

Figure 3.25 The sensitivity of the maximum change in B_x value at zero lift-off to changes in the orientation of the ACFM probe relative to surface crack angle for a 15 mm surface length, 5 mm pocket length semi ellipse [65]. 80

Figure 3.26 Demonstration of the searching algorithm and the B_x waveforms developed in the middle and near the ends of the crack. The location of maximum B_x signal indicates the crack ends in each of the searching windows. 81

Figure 3.27 Illustration of 1D ACFM scan for crack sizing. 82

Figure 3.28 The process flow representation for the 1D ACFM scan for crack sizing. 83

Figure 3.29 The process flow representation for an automatic detection scan. 85

Figure 4.1 3D representations of the robotic ACFM scans over UIC54 calibration rail at 2 mm lift-off, matching probe angle, 0.5 mm spacing between scan lines and scan speed of 10 mm/s. 90

Figure 4.2 Direction of the magnetic flux components as measured by the ACFM sensor. 90

Figure 4.3 Response of a first order low-pass filter using a cut-off frequency of 1 rad/s corresponding to $v = 10$ mm/s and $d = 10$ mm. 92

Figure 4.4 Relationship between the normalised B_x signal and crack pocket length obtained from COMSOL simulations of the ACFM signal for semi-elliptical cracks of different aspect ratios and dimensions [65]. 93

Figure 4.5 (a) Contour plots for the ACFM scan over multiple cracks 5-8 and (b) comparison between single scan line data showing the maximum change in B_x signal for the multiple cracks and single cracks (1-4). 95

Figure 4.6 Comparison between experiment and simulation of 2D ACFM scans at two probe angle offsets for crack 1. The offset angles are measured relative to the crack. The white and black lines show the direction of crack length based on B_x and B_z signals, respectively. 97

Figure 4.7 Comparison between experiment and simulation of 2D ACFM scans at two probe angle offsets for crack 2. The offset angles are measured relative to the crack. 98

Figure 4.8 Comparison between experiment and simulation of 2D ACFM scans at two probe angle offsets for crack 3. The offset angles are measured relative to the crack. 99

Figure 4.9 Comparison between experiment and simulation of 2D ACFM scans at two probe angle offsets for crack 4. The offset angles are measured relative to the crack. 100

Figure 4.10 Effect of grid spacing on crack angle calculation by the searching algorithm for different probe angle offsets.....	103
Figure 4.11 Reduction of B_x signal due to increasing probe lift-off. The measurements were taken on UIC54 rail using the robot arm at different probe lift-offs and in the absence of a defect.....	104
Figure 4.12 Demonstration of the repeatability of the ACFM point measurement (transverse scan from left to right) using the robot arm for three different locations along the UIC54 rail: (a) first (b) second and (c) third location.....	106
Figure 4.13 Comparison of B_x signal for different lift-off values for robotic scans along the opening of three semi-elliptical cracks having aspect ratio of 1:1.....	107
Figure 5.1 Demonstration of thresholding method for low speed detection of defects using the developed robotic system at the Long Marston Railway line. The dashed lines show the thresholds used for defect detection. See Table 5.1 for the detailed explanation of the defects.....	110
Figure 5.2 Demonstration of thresholding method for detection of defects from high speed ACFM measurements on rotating rail rig at 48 km/h using a 50 kHz probe [54]. Labels: RG → Rail Gap, ID → Isolated Defect, CD → Clustered Defect. The dashed lines show the thresholds used for defect detection.	111
Figure 5.3 Representation of the analytical signature for a B_x signal due to a single RCF type defect (top) and its analytical derivative ΔB_x (bottom).	113
Figure 5.4 The process flow representation of the CTSM algorithm.....	115
Figure 5.5 Photograph of the developed robotic system at Long Marston railway.	116
Figure 5.6 The artificial defects of varying geometries on the rail track. The numbers represent the order in which the defects appear relative to the fixed datum.....	117
Figure 5.7 The results of detection scan with the robotic system at 5 km/h with an initial ACFM probe lift-off of 3 mm and angle of 52° with respect to the running direction for the first trial. The top graph represents the B_x signal, the middle graph represents the relative change of B_x signal with respect to its local background (ΔB_x) and the bottom graph represents the instantaneous position of the trolley.	121
Figure 5.8 The results of the detection scan with the robotic system travelling at 5 km/h with an initial ACFM probe lift-off of 3 mm and angle of 52° with respect to the running direction for the second trial.....	122
Figure 5.9 Plot of ΔB_x data in the vicinity of each CS for the (a) first and (b) second trials. The accepted and rejected crack candidate signals are marked in green and brown, respectively.	123
Figure 5.10 Illustration of the rotary rail rig at the University of Birmingham used for high speed ACFM measurements [56].....	124

Figure 5.11 Plan view representation of artificially induced defects on rotary rail rig used for the high speed ACFM measurements [56]. 125

Figure 5.12 Performance of the CTSM algorithm in the detection of artificial defects from high-speed ACFM scans at 16 km/h using a 50 kHz probe. Labels: RG → Rail Gap, ID → Isolated Defect. 127

Figure 5.13 Performance of the CTSM algorithm for the detection of artificial defects from high speed ACFM measurements on rotating rail rig at 32 km/h using a 50 kHz probe. Labels: RG → Rail Gap, ID → Isolated Defect, CD → Clustered Defect. Some defects were missed due to excessive lift-off. 128

Figure 5.14 Performance of the CTSM algorithm in the detection of artificial defects from high speed ACFM measurements on rotating rail rig at 48 km/h using a 50 kHz probe. Labels: RG → Rail Gap, ID → Isolated Defect, CD → Clustered Defect. 129

Figure 5.15 The real-time position and velocity plot of the robotic system travelling to the location of the second defect which is 8.65 m relative to the datum. 130

Figure 5.16 (a) The normalised contour plot of automated ACFM scans over the second defect (see Table 5.1) at a constant lift-off of 3 mm and orientation angle of 45° relative to the running direction. The white line shows the crack orientation (32.5°) as calculated by the automatic crack surface angle detection algorithm. (b) The rail profile measured by the robot arm using the laser distance sensor in the vicinity of the second defect. (c) Comparison of the COMSOL simulation and experimental result of the ACFM scan over the second defect at 3 mm lift-off and relative angle offset of 10°. 132

Figure 6.1 COMSOL simulation results of ACFM response to multiple-RCF cracks at different crack spacing using 5 kHz probe at zero lift-off [113]. 135

Figure 6.2 Result of CTSM algorithm on the ACFM measurements over multiple-RCF cracks at a range of crack spacings based on an isolated crack signature. In each graph, the blue curve represents the derivative of the normalised Bx signal while the green/brown curve represents the best fit after optimisation. 136

Figure 6.3 Demonstration of the first derivative of the Bx signal and the zero crossings. 137

Figure 6.4 Result of using the extended CTSM algorithm on simulated ACFM responses to multiple-RCF cracks of varying spacing. 139

Figure 6.5 Result of the extended CTSM algorithm for the simulated ACFM response to multiple-RCF cracks of varying spacing. The data were superposed by additive white Gaussian noise of SNR of 10 dB. 141

Figure 6.6 Result of the extended CTSM algorithm for the simulated ACFM response to multiple-RCF cracks of varying spacing. The data were superposed by additive white Gaussian noise of SNR of 5 dB. 142

Figure 6.7 Results of the robotic ACFM measurements over rail samples 1-7 at constant lift-off of 2 mm and matching probe angle. The data shown correspond to scan lines where the Bx signal

reduction is a maximum. Only the portion of the scan lines containing multiple-RCF crack signatures have been used for the analysis. 146

Figure 6.8 *Result of the extended CTSM algorithm on robotic ACFM measurements over rail samples 1-7 at constant lift-off of 2 mm and matching probe angle. In each graph, the data shown correspond to the scan line where the Bx signal reduction is a maximum. 147*

List of Tables

Table 1.1 Frequency of rail track inspection using Ultrasonic. The intervals indicate months between tests [5].	2
Table 2.1 Summary of the NDT methods and their associated signal processing.	49
Table 3.1 Explanation of the software agents (routines) used to communicate with the hardware (sensor and actuator) agents. Parallel blocks represent the multi-threading characteristics.	56
Table 3.2 Explanations of the DOFs required by the ACFM sensor for automatic RCF crack characterisation.	57
Table 3.3 The representation of ACFM sensor data format.	63
Table 3.4 Summary of the hardware registers used in the QEI module for PIC18F4431.	68
Table 4.1 Schematic diagram and details of the calibration block.	88
Table 4.2 Comparison between the estimated and real crack parameters.	93
Table 4.3 The numerical results of crack surface angle calculation based on the experimental measurements for cracks 1-4 using uniform grid spacing of 0.5 mm.	102
Table 4.4 The numerical results of crack surface angle calculation based on the COMSOL simulation for cracks 1-4 using a uniform grid spacing of 0.5 mm.	102
Table 5.1 Quantitative information on the artificial defects/rail joints.	117
Table 5.2 Performance of the CTSM algorithm in automatic detection of faults (i.e. artificial defects and rail joints) based on the ACFM measurements taken at Long Marston Railway line using the robotic system.	120
Table 6.1 The rail samples taken from in-service rails containing a number of real RCF cracks at a range of spacings and surface angles. The rail profiles were measured prior to ACFM grid scans.	145

List of Abbreviations

AC	Alternating Current
ACFM	Alternating Current Field Measurement
AI	Artificial Intelligence
ANN	Artificial Neural Network
CS	Candidate Signals
CTSM	Combined Threshold and Signature Match
DOF	Degree of Freedom
EC	Eddy Current
EMAT	Electro Magnetic Acoustic Transducer
FEM	Finite Element Method
FT	Fourier Transform
HIL	Hardware in the Loop
IUI	Intelligent User Interface
LAHUT	Laser-air Hybrid Ultrasonic Transducer
LRU	Long Range Ultrasound
LUT	Laser Ultrasonic Transducer
MAS	Multi Agent System
MFL	Magnetic Flux Leakage
NDT	Non-destructive Testing
PEC	Pulsed Eddy Current

PIC	Programmable Interface Controller
QEI	Quadrature Encoder Interface
QOF	Quality of Fit
RBES	Rule-Based Expert System
RCF	Rolling Contact Fatigue
SD	Standard Deviation
SNR	Signal-to-Noise Ratio
SSPE	Steady State Position Error
SVM	Support Vector Machine
TOF	Time of Flight
UT	Ultrasonic Transducer
VI	Visual Inspection
WT	Wavelet Transform

Chapter 1. Introduction

1.1. Background

The increased traffic on the rail network and the growing demand for high speed and high capacity trains across the Europe means that the maintenance of railway assets is a significant concern to the railway industry [1, 2]. The maintenance should be carried out on a regular basis to minimise the threats associated with failure of both tracks and wheels (e.g. rail track breaks and/or train derailments). One of the common causes of rail track failure is due to the rolling contact fatigue (RCF) crack which is a known threat to the rail industry. After the Hatfield accident in 2000, rail industries around the world have begun to treat rail track inspection, in particular RCF cracks, more seriously than before [3, 4].

Increases in train speed and axle load intensify the risk of track failure due to RCF cracks. Although there have been considerable improvements in maintenance in the past few decades due to employing novel non-destructive testing (NDT) methods to detect defects (e.g. guided waves, non-contact ultrasonic etc.), there are large areas for potential improvement through increasing the reliability and accuracy of the current NDT inspections and hence optimising the maintenance schedule. At present, rail inspection is carried out manually using hand-held systems (e.g. ultrasonic Sperry sticks) or by high speed dual purpose rail/road vehicles equipped with various NDT sensors. The frequency of inspection is dependent on the track category which is obtained from a standard speed-tonnage curve (Figure 1.1). The inspection frequency is summarised in Table 1.1. Following the track

inspection (either manually or by using high speed trains), the defects found are coded (classified) according to an existing standard. Each code contains information about the minimum action to be taken and also the time scale. Different codes signify a different defect type and severity (size) which is determined based on the amplitude of the measured signal. The maintenance action to be taken is then determined from the code. The time scale may change from one day to a couple of weeks depending on the size of the defect.

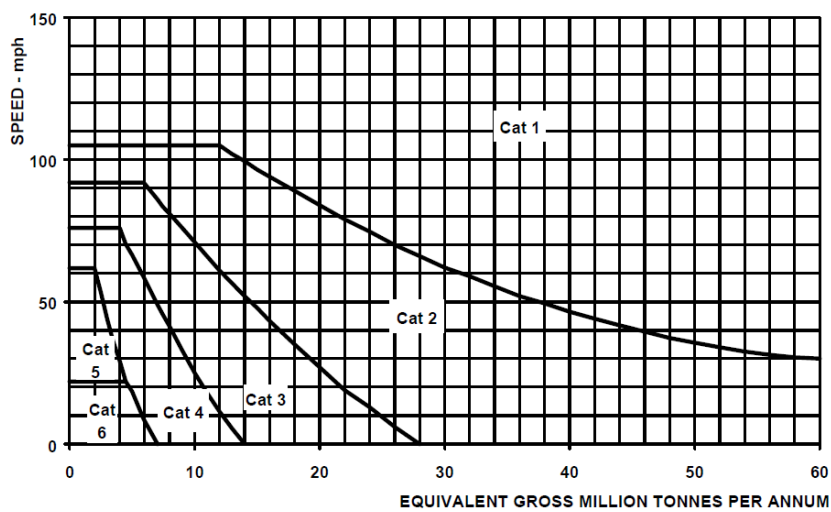


Figure 1.1 Standard rail track speed-tonnage curve used in the UK [5].

Table 1.1 Frequency of rail track inspection using Ultrasonic. The intervals indicate months between tests [5].

Category	Within Fishplate limits Within switches and crossings At adjustment switches In Tunnels		Standard Intervals	
	Nominal Interval	Maximum Interval	Nominal Interval	Maximum Interval
1	3	3.5	6	7
2	6	7	12	13
3	12	13	24	26
4	12	13	24	26
5	12	13	24	26
6	24	26	24	26

The reliability of these types of inspections is affected by factors such as human uncertainty about defect orientation/location which may cause a large offset in the inspection data (e.g. the reduced disturbance to the background signal due to an increased angle offset between the defect and eddy current direction, in the electromagnetic case) and low signal-to-noise ratio (SNR) due to mechanical vibration in the high speed case (e.g. in ultrasonic transducers).

The nature and time of the maintenance action is directly influenced by the severity of the defect. Decision based solely on the high speed inspection data may result in misclassification of the defect's severity which has potential to cause unpredicted catastrophic failures. Also, the false detection of defects would mean an unnecessary maintenance action which deteriorates efficiency of the maintenance. Therefore, there is a need for further manual inspection of the defects found at the high speed inspection stage by a highly skilled operator prior to taking any maintenance action.

1.2. Motivation

In manual inspection of rail tracks, expert operators (Figure 1.2) are used to interpret the inspection data and to distinguish the difference between defect signals from defect-like signals. They are also employed to increase the accuracy and reliability of the inspection data which is of prime importance when sizing the defect. The collected data is subject to human interpretation. Moreover, the operators are subject to factors such as fatigue and unpredicted problems. Further, training skilled operators is a time consuming and costly process which may impose large constraints on the maintenance strategy. Another major issue is the speed at which the operators can inspect the rail (getting them to the right

place). In this research AI and robotics are combined together to offer large benefits in minimising the use of human operators for rail inspection.



(a)



(b)

Figure 1.2 (a) Manual inspection of rail using ACFM walking stick [6] and (b) portable ultrasonic flaw detector [7].

The idea behind this research is to implement the human expert knowledge in a computer program so that an automated system could be constructed which can perform the same task as an expert operator. In doing so, a great deal of effort has been put to develop a robotic rail inspection trolley, which can be used to autonomously inspect the rail tracks for RCF cracks.

1.3. Aims and Objectives

The main aim is to develop a fully automated system that at a first high speed pass detects the possible presence of defects in railway track due to fatigue caused by high speed and heavy train axles. It is then required to autonomously return to an identified defect position(s) to perform a second slower pass to scan a rail section and determine (without human operator intervention) the size, depth and number of cracks in that section. The scanning arm should have the ability to calibrate its position relative to a rail that (a) may be misaligned with respect to the next rail at a joint gap and (b) have a worn cross-sectional profile. It should then raster scan a rail section with a grid pattern by following a possibly worn contour (profile) of the rail while maintaining the ACFM probe at a constant lift-off from the rail surface and normal to it to optimize the quality of NDT data. In addition, the probe angle should be oriented to align it with the direction of a given crack to obtain accurate crack length and depth. The optimized NDT data should be processed by an intelligent expert system to characterize the defects (i.e. length, depth, orientation and position from a datum point) without human intervention. The following summarises the objectives of the research:

- Investigate the state-of-the-art of rail inspection systems and NDT techniques;
- Develop an experimental robotic system that is able to travel autonomously on a track at specified speeds. It should be able to measure its position from a datum point. It should also carry a scanning arm with sufficient degrees of freedom to maintain an ACFM probe normal to the rail surface at a constant lift-off despite variation of the rail profile, while holding the probe at the same orientation angle as an inspected crack. Calibration procedures should be included to position the ACFM probe in the correct way by determining the rail cross-sectional profile and crack orientation;
- Carry out a study of the static performance of the robotic NDT system in finding and characterizing artificially machine single and multiple defects in various scenarios e.g. matching and non-matching probe/crack angles, scanning grid size and spacing, effect of variation of probe lift-off, and signal noise. Extend the above methods to distinguish and size multiple closely clustered defects with an investigation of the performance of the automated defect characterising system for different spacing between individual defects.

1.4. Contributions

1.4.1. Hardware and Software Development

The author has developed a robotic inspection system which may be used to autonomously inspect the rail tracks for RCF cracks. The robotic system consists of a mechanised four-wheeled trolley, a developed motion controller unit, a six degrees of freedom (DOF) robot arm, a commercial ACFM single probe sensor with instrumentation, a commercial laser

triangulation displacement sensor and user interface software which serves as the core of the robotic system. The system is capable to both detect and characterise (size) the defects.

In detection mode, the system moves along the rail track and inspects a specified length using the settings set by the user (e.g. inspection speed, sensor lift-off etc.) and finds the position of the likely RCF cracks with respect to a fixed datum.

In characterisation mode, the position of the defects found is imported to the software so that a steady and detailed scan with the robot arm can be performed. For this purpose, the system automatically travels to the location of the defects and uses the robot arm to first measure the local rail profile in the vicinity of the crack and then to perform a user defined constant lift-off ACFM measurement over the defective area.

1.4.2. Novel Contributions

A systematic methodology for addressing the problem of automatic detection and characterisation of the RCF cracks has been proposed and supported by laboratory experiments and field trials. Autonomy has been given to the system by implementing a piece of knowledge-based intelligent software developed using C++. The software serves as the core of the robotic system where all the real-time data logging, analysis, optimisation and decision making take place. The system is able to both detect and characterise the RCF cracks on rail autonomously while human interaction is largely minimised.

1.4.2.1. Automatic Defect Detection Algorithm

In the process of detecting defects using an ACFM walking stick, currently a simple threshold approach is employed. This method performs well provided the ACFM background signal (i.e. the signal level in the presence of a defect) is steady. However, there are cases where this assumption does not hold. For instance, the inevitable ACFM probe lift-off change at higher speeds or the change in rail magnetic properties along the inspection direction (owing to residual stress) may result in an increase in the background signal which may cause some defects to go undetected if the threshold is set too low. On the other hand, setting the threshold too high may lead to several false alarms depending on the SNR. An initial investigation of both low-speed and high-speed ACFM measurements on rails has shown that it is very difficult to adjust the threshold value so as to detect all defects.

In this research, a novel combined threshold and signature match (CTSM) method has been proposed which helps to automatically detect the RCF cracks without human intervention even in the presence of severe change to the ACFM background signal.

1.4.2.2. Automatic Compensation of the ACFM Probe's Orientation and Lift-off

As the RCF crack surface angle with respect to the rail length can vary in the range of 35°-70° [3, 8-10], it is impossible for existing systems to position the ACFM sensor at an appropriate angle to obtain optimal data for sizing all defects. Moreover, wear of the railhead results in profile changes that will result in variable ACFM sensor lift-off which may significantly reduce the sizing accuracy if not taken into account. These uncertainties/ inaccuracies in crack sizing due to an unknown RCF crack surface angle has been successfully addressed by using a real-time searching algorithm which is able to closely estimate the actual RCF crack surface

angle (within 10°). Therefore the ACFM measurements over the RCF crack may be performed at close to the optimum condition (parallel to the crack, with constant lift-off, normal to the surface) which significantly improves the reliability and accuracy of RCF crack characterisation (sizing).

To summarise, the developed robotic system has shown high potential in automation of rail inspection of RCF cracks which significantly reduces potential human error and therefore, increases dependability.

1.5. Thesis Structure

The following summarises the contents of the chapters in this thesis:

Chapter 1 presents a brief background on rail inspection, motivation, the achievements presented in this thesis and the thesis structure.

Chapter 2 gives an overview of the current NDT technology being used in the rail industry and the research carried out in this field. It also presents a detailed review on the theory of the ACFM technique used in this research. Next, it justifies the need for automating the ACFM based rail inspection.

Chapter 3 starts with a brief review of the requirements of automating the ACFM technique for use in railways and proposes a robotic system using a rule based expert system (RBES), as a solution. Next the process of design and development of the robotic system in terms of both software and hardware methods along with its specifications and limitations is systematically given.

Chapter 4 presents a case study of static robotic ACFM scans on a calibration block containing several induced RCF cracks. The effects of the ACFM sensor lift-off, SNR, ACFM

probe orientation and rail profile have been investigated. Next the results of an online searching algorithm for detection of an unknown RCF crack angle have been studied and compared with simulation results.

Chapter 5 presents a case study of field trials using dynamic robotic ACFM scans on real rail tracks at the Long Marston test track. In addition, the proposed CTSM algorithm for automatic detection of RCF cracks is studied and validated.

Chapter 6 presents a case study of the CTSM algorithm extended to deal with multiple-RCF cracks. The performance of the algorithm has been studied with low speed ACFM results on real RCF cracks and also simulation results on multiple RCF cracks.

Chapter 7 draws conclusions of the presented work and the key findings of the thesis. The strengths and limitations of the proposed robotic system are discussed and the future path of the research is presented.

Chapter 2. Literature Review

2.1. Introduction

This chapter presents an overview of the current state of rail inspection and the NDT methods employed in the railway industry. Initially, a brief review of the characteristics of RCF cracks is given, as these are the main defects considered for detection in this thesis. Different NDT measurement techniques such as visual inspection (VI), ultrasonic transducer (UT), electromagnetic acoustic transducer (EMAT), eddy current (EC), magnetic flux leakage (MFL), and alternating current field measurement (ACFM) are considered. The principle of operation of these methods is discussed and their advantages and disadvantages together with the outcome of recent research on their application are summarised. More emphasis has been placed on the ACFM approach from a theoretical point of view as it is used later in this research as the primary NDT method for inspection of surface breaking defects in rail tracks. In the end, a brief review of the research undertaken in the area of robotic NDT is given and its potential for use in the rail industry is identified by arguing the issues for the ACFM technique in terms of unknown rail grade (shape), lift-off change and unknown crack surface angle which must be addressed to enable its automation.

2.2. Rail Defects

Rails experience wear and fatigue crack growth due to in-service loading. Rail failures from fatigue crack growth can be divided into three categories as follows [2]:

1. Those resulting from rail manufacturing defects – typical examples are the tache ovale or kidney defects that initiate from inclusions or hydrogen shatter cracks in the rail head as shown in Figure 2.1 [2];
2. Those resulting from improper handling, use and installation. An example of this type of defect is illustrated in Figure 2.2 [2];
3. Those resulting from structural degradation as the consequence of rolling contact fatigue (RCF) crack growth. The majority of these types of cracks originate at the rail surface from the cyclical loading and unloading of the track rail at the wheel-rail interface caused by the rolling contact stresses as shown in Figure 2.3 [2, 11].

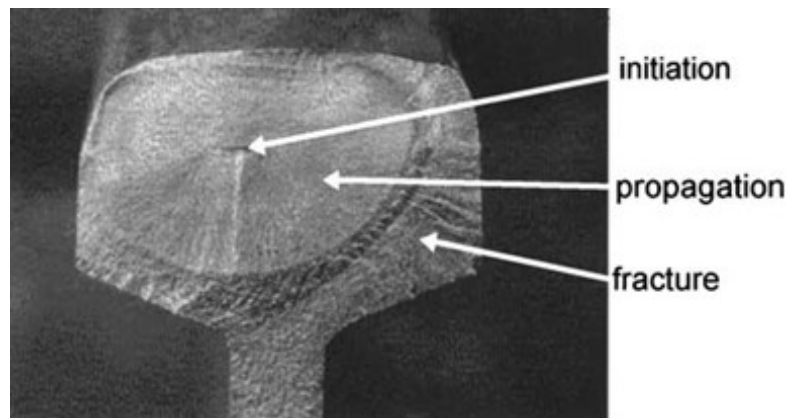


Figure 2.1 Tache ovale or 'kidney' rail failure [2].

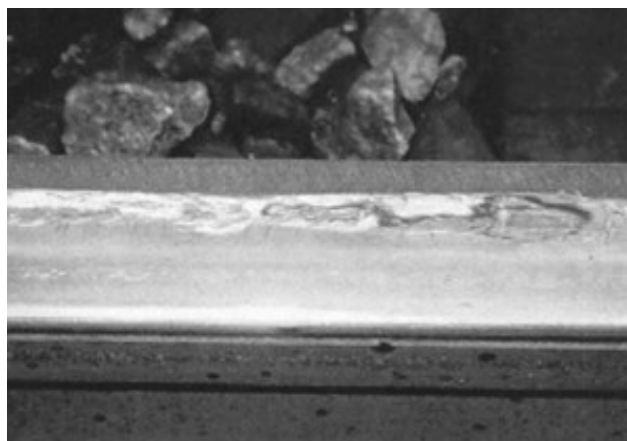


Figure 2.2 Surface spalling of the rail surface caused by wheelburn [2].

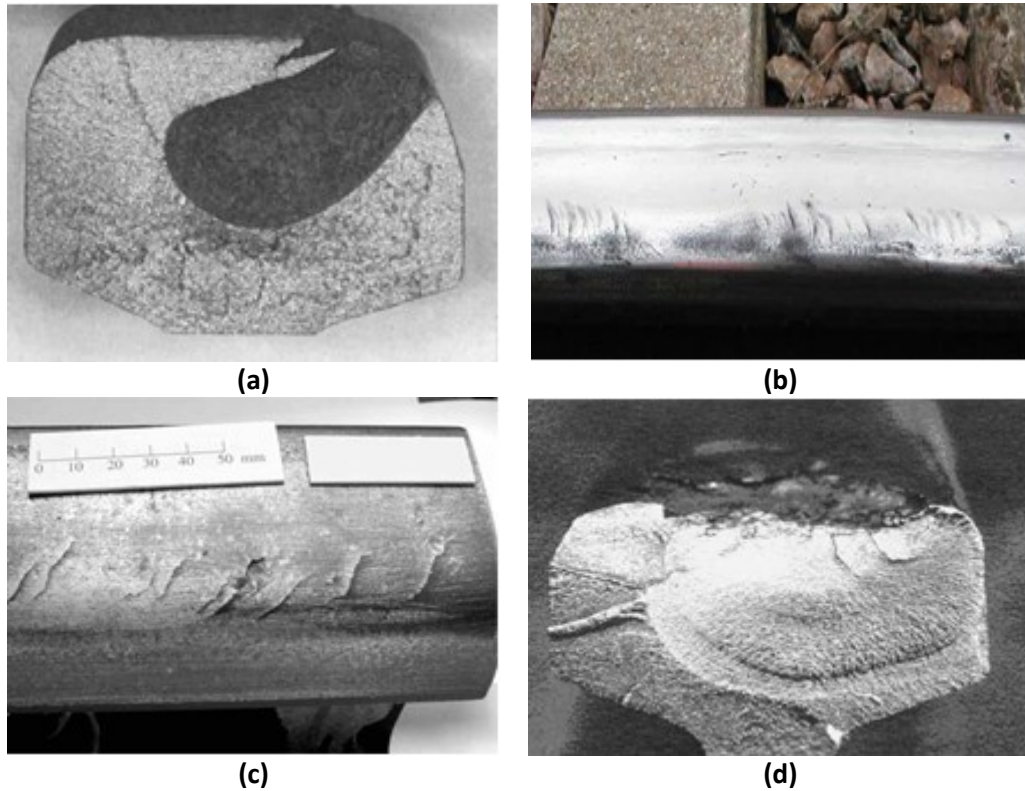


Figure 2.3 Examples of RCF cracks: (a), (b) & (c) head checking (gauge corner cracking) and (d) squats [2, 11].

The defects associated with the first and second category are currently being greatly reduced in the UK, and around the world by improvements in the steel and rail-making industry [2]. The third category, however, has been found to be much more common place, with RCF cracks being of significant concern [2, 4]. These defects can be effectively mitigated by improving the material properties of the rail, performing inspection maintenance and grinding on the track on a regular basis, and changing the conditions of operation (e.g. applying speed limits, managing the wheel and rail profiles) [2].

2.2.1. RCF Cracks

The catastrophic failure of rails in recent decades resulting from RCF cracks has meant that this type of defect is a major concern to the railway industry. For example in October 2000, the derailment of a passenger train at Hatfield, UK [2, 4], showed the severe consequences of RCF cracks. In this case, the existing RCF cracks grew and reached a critical depth, resulting in rail breakage, which caused the derailment of the train. The presence of RCF cracks continues to be a major concern of the railway industry due to increases in demands for higher speeds, higher axle loads and higher traffic density [2]. The current standard code for classification of RCF cracks (light, medium, heavy and severe) is based on a Network Rail, GB guidance chart which classifies the cracks according to their visible surface length [3, 9]. It can be also used to predict the maximum crack depth for a given surface length as shown in Figure 2.4.

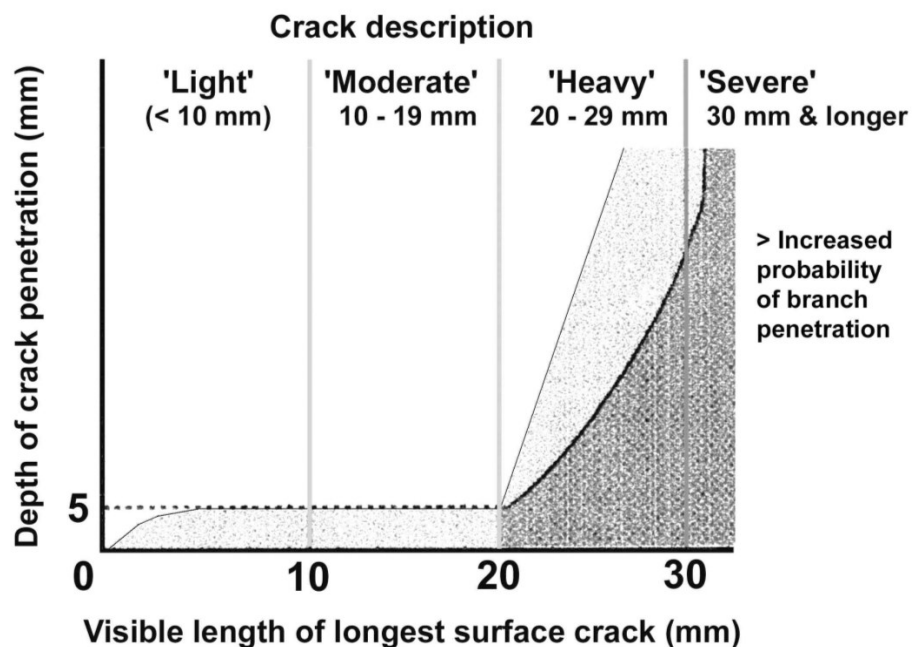


Figure 2.4 Railtrack (now Network Rail, GB) RCF crack visual length/depth guidance [12].

RCF cracks are caused by a combination of high normal and tangential stresses at the wheel-rail interface which causes shear strains in the surface layer of the rail resulting in deformation and eventual crack initiation [2]. Some of these high stresses are due to imperfect loading conditions at the wheel/rail interface (i.e. non-matching wheel-rail profile) due to wear which is termed as 'cant deficiency' within the rail industry. They can also arise from high dynamic loading as a result of slight corrugation [8]. These problems can be mitigated by preserving the wheel/rail profile through grinding on a regular basis [8].

Head checks, gauge-corner cracks and squats (a defect with an indentation shape having two lobes of similar size [13]) are instances of surface-initiated RCF cracks (Figure 2.3) which often form as closely spaced groups of cracks. Under repeated loading, the microscopic crack initially produced grows through the heavily deformed surface layers of the steel at a shallow angle to the rail running surface (usually between 10-30°) until it reaches a depth of a few millimetres [2]. At this point the direction of crack growth can turn upwards leading to spalling of material from the rail surface. However, for reasons still not clearly identified, isolated cracks can turn down into the rail [9], continue to grow, and, if not detected, cause the rail to break.

RCF initiation is not generally linked to any particular metallurgical, mechanical or thermal fault; it is a consequence of the steel's inability to tolerate the imposed operating conditions [2]. These types of surface-initiated RCF result in special inspection difficulties. For both head checks and squats the development of a downward-turning fatigue crack leads to rail failure. Undesirably, the earlier shallow-crack development phase can mask this from conventional ultrasonic examination [1, 2]; this occurrence is known as crack shielding. The use of harder rail grades gives rise to more closely spaced cracks, which even makes the UT inspection

more challenging than before. The use of EC and ACFM technology and better ultrasonic probe arrangements are being considered as potential solutions. The problem of RCF cracks can be contained by grinding the rail running surfaces to remove fatigue damaged material [2], provided the RCF cracks are detected when they are small enough to be removed by grinding. However, as this solution is both costly and time consuming, it is undesirable to grind the rail more than necessary.

2.3. NDT Methods in the Railway Industry

2.3.1. Visual Inspection

In conventional visual inspection (VI), trained rail inspectors walk along the rail track and search for defects by eye. Despite the high level of subjectivity, VI is still being used by some infrastructure managers. However, with the advancements in high speed electronics and visual cameras, the manual VI methods are generally being replaced by automated visual systems [14]. An example is shown in Figure 2.5. In automated VI, a high speed camera is used to capture video images of the rail while the train is moving. It may be used to find missing track components such as fastening bolts and fishplates and also surface damage such as RCF cracks and rail corrugation [1, 15-17]. Depending on the type of inspection and the required quality, different camera resolutions may be used. For example, in VI inspection of the rail surface, a higher resolution camera is employed to provide reliable data for detection of small defects [1]. Detection of missing objects or surface defects is achieved through image analysis of the recorded data offline.

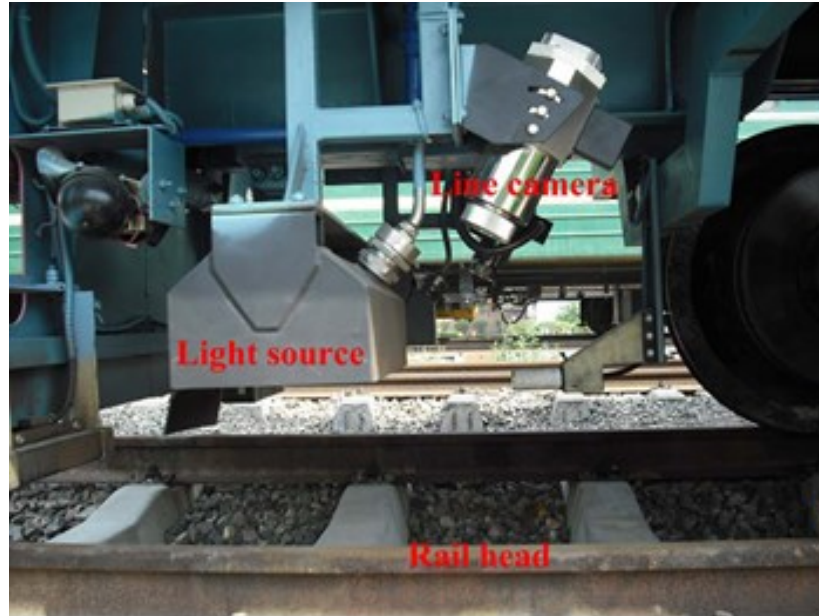


Figure 2.5 Experimental setup for automated VI used by Qingyong, et al. [18].

The performance of detection by VI is limited by the computational efficiency of the camera and also the hardware used for image processing. Thus, for the real-time VI, the inspection speed needs to be adjusted to keep pace with the data analysis [1].

Singh, et al. [19] developed an autonomous rail track inspection process using a vision based system. They used image processing and analysis methods for finding missing clips (used to secure the rail to the sleepers) and blue clips used in place of damaged clips. Finding clips is based on the density of edge pixels of the recorded frames. The frames experience a pre-processing short line removal stage and then are placed along the lines symbolizing the track. The frame containing the highest density of edge pixels represents the position of the clip. Blue clips were also detected by using a colour analysis method. Based on the experimental results, the authors claimed that automated image processing is a promising and effective approach for visual inspection of rail tracks.

Li, et al. [20] also presented a software solution for component-based track inspection using machine-vision technology. Their proposed system includes imaging setup for capturing multiple video streams, important rail component detection such as tie plates, spikes, anchor and joint bar bolts, defect identification such as raised spikes, defect severity analysis and temporal condition analysis, and long-term predictive assessment. Their initial performance study has revealed an average of 98.2% detection rate, 1.57% false positive rate and 1.78% false negative rate on the component detection.

2.3.2. Ultrasonic Transducers

The ultrasonic transducer (UT) is one of the most widely used NDT techniques in various fields of industry such as power generation, manufacturing and railways. In the ultrasonic inspection method, piezoelectric transducers are used to transmit ultrasonic energy in the form of sound waves into the specimen [21]. The waves can be generated in two modes: transverse (shear waves) and longitudinal (compression waves). In the transverse mode, the particles oscillate normal to the direction of wave propagation whereas in the longitudinal mode the particles oscillate parallel to the direction of wave propagation. In rail inspection using UT, liquid based (usually water) couplant is used in order to assist transfer of mechanical waves from the transducer to the rail surface. There are two common configurations of UT inspection: pulse-echo and pitch-catch. In the pulse-echo (Figure 2.6 right) method the transducer is used as both actuator (transmitter) and sensor (receiver) and is used to detect sub-surface cracks or discontinuities normal to the rail length. In the pitch-catch method (Figure 2.6 left), the transmitter and receiver are separate units which are placed at different locations of the specimen and are used for detection of cracks or

discontinuities parallel to the rail length (e.g. vertical split). For a normal angle of incidence, they are placed at opposite sides of the specimen and held collinear.

The integrity of the structure under inspection is evaluated based on the amplitude of the reflected waves along with when they occur in time [7]. In order to improve the chance of defect detection, the ultrasonic energy is transmitted at different incident angles, typically, 0° , 37° , 45° and 70° to maximise the probability of detecting unknown defects [1, 7]. The main benefit of this approach is the high depth of penetration leading to detection of internal defects such as web and sub-surface defects. The performance of ultrasonic test trains is generally high in detecting deep surface-breaking and internal defects, especially in the rail head and web [1]. In contrast, RCF defects less than 4 mm deep may be missed at high speeds. Besides, smaller surface cracks can shadow larger and more critical internal defects and therefore produce an invalid representation of the structural integrity of the rail [1].

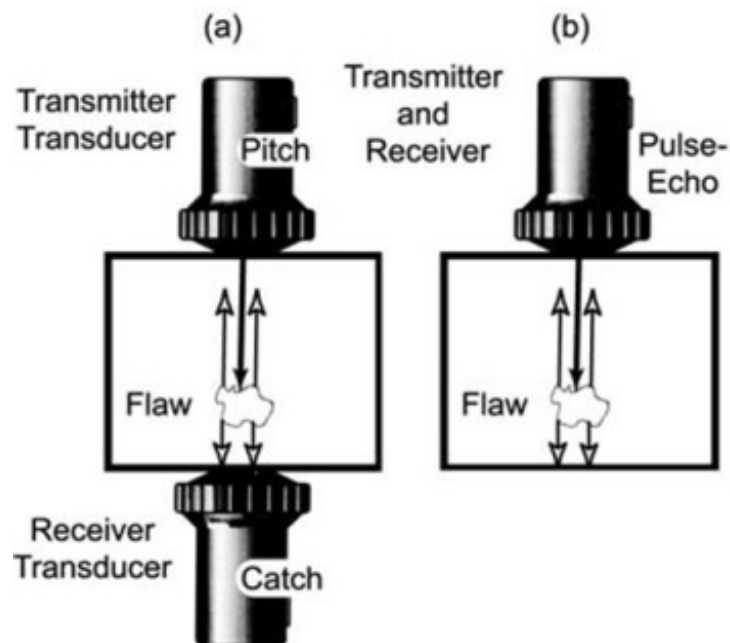


Figure 2.6 The two basic methods of transmitting and receiving ultrasound:(a) pitch-catch (separate transducers) and (b) pulse-echo (single transducer) [22].

Bray [23] conducted an experiment by using an UT sensor in order to detect internal defects in used track rails. Based on the reflected wave's data, he recognized that the material properties of used rail head are anisotropic; hence the UT sensors that were calibrated for isotropic rail failed to locate the transverse (tache ovale) defects in used rails. Moreover, in the case of conventional UT inspection methods, several difficulties have been reported in the literature with regards to the adjustment of acquisition time and signal threshold (amplitude) [1]. In the former case, the acquisition time window is normally expanded more than strictly required in order to take into account the sound velocity and material inhomogeneties [1]. Setting the time window too close to the origin (corresponding to the rail surface) may result in excessive noise while setting it too far may mean some sub-surface defects are missed [1]. In a similar way, in the latter case, the signal threshold value needs to be carefully set; a high threshold may result in missing some defects while a low value may generate several false indications of defects.

2.3.3. Laser Ultrasound

Unlike conventional UT methods, which use contact transducers, in the laser ultrasound (LUT) method, the ultrasound wave is generated by a modulated laser pulse from a remote location. When the laser pulse strikes the rail surface, ultrasonic waves are induced as a result of either rapid thermal expansion, which in turn produces thermo-elastic stress, or by ablating the medium [24]. The reflected waves are measured using optical probes or by air-coupled acoustic transducers [1]. Therefore the LUT method offers non-contact inspection of rail which comprises the following advantages [1, 24]:

- Inspection speed up to 15 km/h were reported;

- Couplant independent, therefore, the absolute wave displacement may be measured;
- Small footprint, therefore can be used to inspect most parts of rails with curved surfaces.

However, the LUT has also some drawbacks; the optical/air-coupled transducers have lower sensitivity than contact piezoelectric transducers [24], hence more signal processing effort is needed to distinguish the defects from the noise. Further, the high cost of the LUT method makes it worthwhile in limited circumstances.

Kenderian, et al. [25] investigated the application of laser-air hybrid ultrasonic (LAHUT) for detection of internal defects such as vertical split head and transverse defects in rail tracks. In LAHUT a remote laser source is used to transmit acoustic waves to the surface of rail while air-coupled UT transducers are used to record the reflected energy from the specimen (in the form of surface shear or bulk waves) in close proximity (few centimetres) of the rail surface. The results from field trials at walking speed (using a pushcart) suggested that the method was effective (high detection rate) for dynamic inspection of vertical split head and rail base cracks where the existing state-of-the-art techniques struggle to detect defects [25]. It may be also used for inspection of defects that are unfavourably positioned (e.g. transverse defects) for conventional NDT methods.

2.3.4. Electromagnetic Acoustic Transducers

Electromagnetic acoustic transducer (EMAT) is another non-contact ultrasound technique. Here the ultrasound wave is generated by inducing radio frequency eddy currents in the material under inspection in the presence of a strong static magnetic field [26]. According to Lorentz's law, a force is then generated, whose direction is normal to both the induced current and the magnetic field in the right hand sense. This results in an ultrasonic stress

wave. Different wave modes of ultrasound (e.g. compression, shear and plane) may be generated by changing the orientation of the magnetic field and geometry of the inducer coil. Similar to LUT, in the EMAT method, there is no need for acoustic matching; therefore it has the advantage of non-contact operation which makes it suitable for inspection of rail especially at high speeds.

The use of the EMAT method in the rail industry has been reported in several publications [1, 27-29]. Edwards, et al. [30] have investigated the use of non-contact ultrasonic pitch-catch EMAT sensors generating Rayleigh-like waves for detection of induced RCF defects in rail at high speeds (approximately 140 km/h). They suggested that EMATs may be used to detect RCF cracks at high speeds but also reported some shortcomings; in the case of multiple-RCF cracks, only the depth of the deepest defect may be detected. Besides, the method lacks spatial resolution therefore the exact position and number of RCF defects cannot be detected. Therefore high speed EMAT inspection was proposed to be used as a preliminary approach for finding areas of rail which require further examination. They also confirmed that at walking speed, the EMAT has been able to detect a range of artificial RCF defects including clusters of three closely spaced defects and isolated small defects (2-15 mm depth).

2.3.5. Long-range Ultrasound

In the long-range ultrasound (LRU) method, the ultrasonic transducers have been designed to produce bulk waves of different modes, such as Rayleigh, Lamb, and Plate waves, which are commonly referred to as 'guided waves' or 'surface waves'. These waves propagate along the surface of the rail and thus are capable of detecting transverse surface defects

such as RCF cracks or changes in cross-sectional area due to corrosion. Several researchers investigated the application of LRU method in the rail industry [31-34]. The major benefit of this technique is its long range of coverage and in ideal conditions it can cover up to 30 m of rail from the sensor but in some cases the practical covering range may be reduced to a few metres because of a considerable reduction of the ultrasound signal caused by various factors [1]. The wave mode and operational frequency play a crucial role in determining the effective coverage range. The LRU method is sensitive to changes in cross-sectional area of the material. Defects must produce at least 5% reduction in cross section in order to cause a distinguishable reflected signal. Bartoli, et al. [33] performed a simulation study of the interaction between ultrasonic guided waves and transverse defects on rails using the finite element method (FEM). They computed the reflection coefficient (ratio of the energy of the reflected wave to that of the transmitted wave) in the frequency range of 20-45 kHz for a number of oblique transverse defects. Their simulation results revealed a significant reflection from defects as small as 15% of the rail head. They found that in the case of oblique defects angled at 20° relative to the rail length, for frequencies above 30 kHz, the reflection decreases by increasing the defect's surface length owing to severe mode conversion for 20° cuts [33]. Moreover, they observed that the reflection from defects increased by increasing the angle. Their results indicate that, in order to inclusively detect surface defects in rails using the LRU method, different frequency ranges, rather than a single frequency, should be used.

McNamara, et al. [35] used experimental LRU measurements on transverse and oblique defects in rails to develop a supervised smart system using a support vector machine (SVM), which helped identify the defects automatically. They classified the defects based on the

values of their surface angle (angle made by the surface breaking crack length and the rail running direction) and their severity (large or small). They repeated their measurements by using different wave modes (vertical, transverse and longitudinal) over a frequency range of 10-40 kHz in order to find the best wave mode most suited (i.e. most sensitive) to a particular class of defect. They also confirmed that when a portion of the frequency range (rather than the whole range) is used, the number of misclassified defects increases and therefore for effective automatic classification the entire frequency range should be used when training the classifier.

2.3.6. Eddy Currents

This technique relies on the electromagnetic effects when an alternating current (AC) is passed through a primary coil; this leads to the induction of eddy currents (EC) in the surface layer of the metallic material (skin effect) under inspection (Figure 2.7). Any distortions caused to the eddy current (due to the presence of defects) will generate a secondary magnetic field, which will in turn affect the impedance of the secondary coil (Figure 2.7a). This change in the impedance can be monitored by a voltmeter and continuously displayed [36]. The key advantages of the EC method is that, unlike conventional ultrasonic testing, in EC testing the sensor is not required to be in contact with the material under inspection thus making it suitable for high speed inspection [36]. EC is sensitive to fine cracks and can be therefore used to detect RCF cracks such as gauge corner cracking at speeds up to 100 km/h [37]. However, despite its broad advantages, this method suffers from a number of shortcomings; the EC sensor not only responds to the disturbance to the induced eddy current (due to surface defects) but it also responds to undesired signal changes resulting

from variation of the material's properties, such as conductivity and permeability (due to the work hardening of the surface or due to the presence of wheel burns or welds). Further, special care needs to be given to avoid lift-off change as the EC method is very sensitive to lift-off; in practice, it is common to try and control the lift-off to 2 mm (maximum) [1].

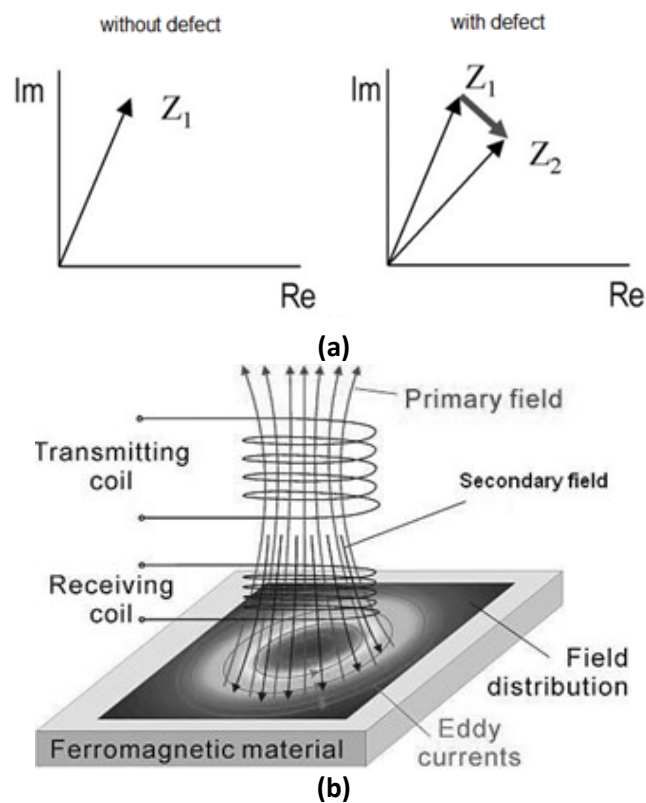


Figure 2.7 Illustration of the operation of the eddy current testing; (a) variation of the receiving coil's resultant impedance in the presence of a defect (horizontal and vertical axis display the coil resistance and impedance, respectively) (b) the distribution of EC on the surface of a specimen [37].

These undesired responses on the EC sensor are difficult to compensate for and would demand complex mathematical algorithms if present and high knowledge of the operator [36]. The other disadvantage of this method is that calibration is required in order for defect characterization. The common method of processing an EC signal would be to compare the

maximum amplitude of the signal to the reference signal; however this method is not robust and can lead to an underestimation of length and depth of the crack.

Bentoumi, et al. [38] presented a novel algorithm for real-time detection of surface defects from EC sensors based on differential measurements. They successfully separated the crack-like signals (resulting from bogie dynamics etc.) from true crack signals (fishplated joints, welded joints and shelling) using dual sensor measurements and proposed an automatic detection algorithm using a wavelet transform (WT) by means of a mother wavelet which resembles the signature of a typical crack signal. The detection of defects was then based on the magnitude of the highest modulus of transformation (thresholding). The results from their field trials suggest that the WT is capable of detecting surface defects automatically; however it struggles to distinguish shelling signals from welded joint signals.

Pulsed eddy current (PEC) is an improvement to the conventional EC method in which excitation of the inducer coil is achieved by a step rather than a single frequency sinusoidal voltage. The advantage is that a range of frequencies can be generated at once which means that a range of skin depths are obtained. Therefore critical information from a range of depths can be attained. For the response signal in the time domain, information about the features near the surface of the specimen (e.g. surface breaking defects) are observed first while more distant features (e.g. holes or discontinuities below the surface) are observed later in time. The PEC method has been recently used in the railway industry as a complementary means to UT inspection, which struggles to detect surface or near surface breaking defects especially at high speeds [37, 39-42]. The maximum inspection speed for the combined PEC and UT methods are reported as 75 km/h [1].

Smid, et al. [43] proposed a post processing algorithm based on a normalization technique for classification of defects, detected by the EC sensor. Artificially induced slots in an aluminium sample were used to mimic surface breaking defects typical of those found in aircraft structures. They employed complex discrete WT for feature extraction and classified defects using non-linear classifiers. They demonstrated that their method may be used to alleviate the problem of EC impedance change due to inevitable variations in scanning speed and probe position during manual scanning.

2.3.7. Magnetic Flux Leakage

Magnetic flux leakage (MFL) is a common method for non-destructive evaluation of ferromagnetic structural components and is widely used in the petrochemical, oil, energy and material industries [44-46]. In the MFL method, DC electromagnets or permanent magnets are used to magnetize the material under inspection to saturation, as depicted in Figure 2.8, and search coil probes are used to monitor, and quantify, the leakage in the magnetic field [44-46]. The MFL probes scan across the surface of the component under inspection looking for irregularities in the flux density which designates the location of a defect. It can be used to inspect complex geometries and features which are not visually accessible (e.g. inside surface of oil and gas pipe lines) [47].

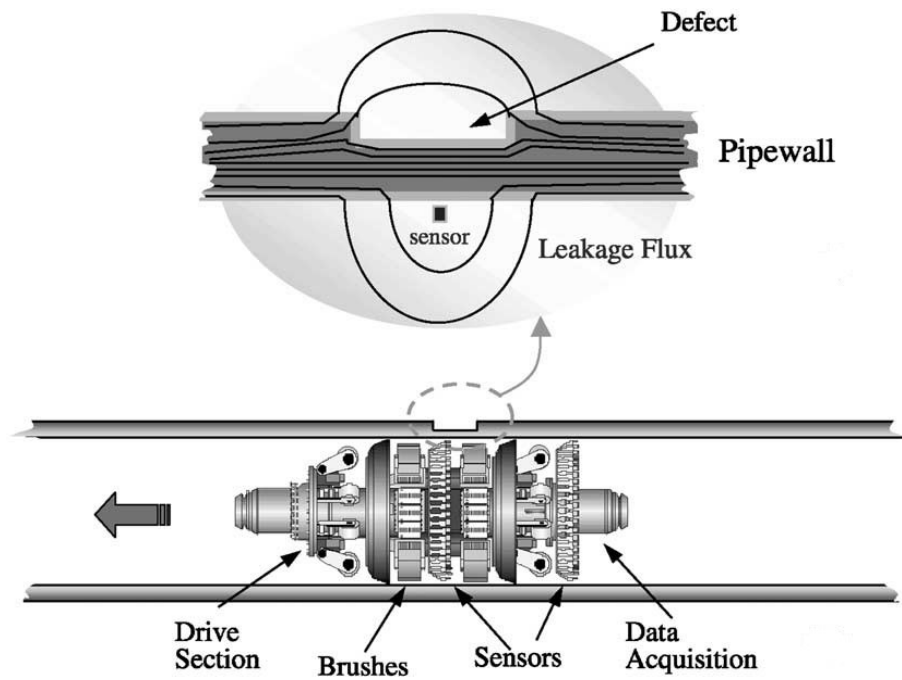


Figure 2.8 Principle of operation of MFL method used for pipeline inspection [48].

The MFL technique is more beneficial for applications where the defect location is already known or the defect location can be predicted with a realistic possibility of success [47]. A disadvantage of this method is that the intensity of the magnetic flux is significantly reduced by increasing inspection speeds and this reduces the sensitivity of the signal. The maximum operating speed for railway applications has been reported as 35 km/h [1]. A simulation study of an MFL sensor operating at high speed has been conducted by Li, et al. [49]; according to this work, the defect characterization is strongly affected by the speed (Figure 2.9), thus complex mathematical algorithms are required in order to take into account the effect of speed on the feedback signal. Therefore the MFL technique may be applied to collect detailed data for characterising known defects [50, 51].

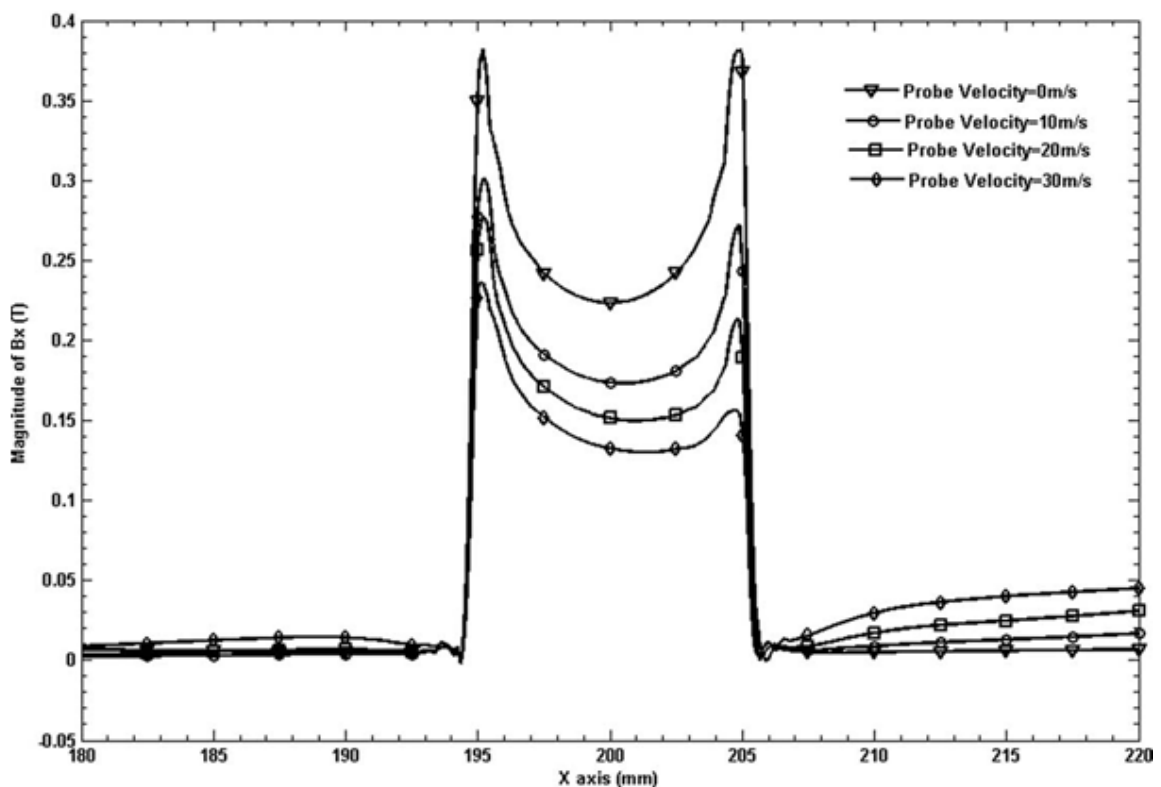


Figure 2.9 Simulation result of magnetic flux response to a rectangular slot at different probe speeds [49].

2.3.8. Alternating Current Field Measurement

The alternating current field measurement (ACFM) technique is a more recent NDT inspection method to be used in the rail industry and has drawn particular attention because of its combined advantages as listed below [1, 6, 52, 53]:

- High speed inspection capability, speed up to 121 km/h has been reported [11, 54-56];
- The capability to both detect and size defects;
- Reduced sensitivity to lift-off variation compared to the EC method;
- The ability to detect defects even with the presence of coatings and dirt (similar to the EC and MFL method);
- Non-contact.

Unlike the MFL method which uses large DC or permanent magnets to excite the specimen to saturation, the ACFM technique relies on the fact that an alternating current (AC) can be induced to flow in a thin skin near the surface of any conductor. When a remote uniform current is introduced into the area of the specimen under inspection, the induced current will remain undisturbed provided there is no defect present. Any defect present will force the current to flow around the ends and down the faces of the crack (Figure 2.10). The changes in the direction of the current will introduce non-uniformity to the magnetic flux which is constantly monitored using two sensors measuring the magnetic field in two directions. Near the crack ends the current lines become closer as they pass the defect. This gives rise to changes in the component of magnetic flux around the crack ends (B_x). A rotation of the current around the crack ends also occurs, which produces a non-zero component of the magnetic field normal to the surface of the specimen (B_z). Further, as the

current goes down the face of the crack it produces a trough in the B_x signal. The reduction in the B_x signal can be related to the crack's pocket length (i.e. length of crack along the direction of propagation below the surface) through inversion of the ACFM signal. The inversion process is not straightforward and involves a great deal of complex mathematical computations. The approximate crack surface length may be obtained from the distance between the characteristic peak and trough in the B_z signal provided that the ACFM sensor is oriented along the crack's opening. This is quite advantageous as it avoids the need to use a human/visual inspection (i.e. helps with automation). It has been shown that in practice this would give a reasonable measure of real crack surface length and the parameters such as sensor lift-off and crack aspect ratio (surface length to twice pocket length) are found to have a small effect on this value [52].

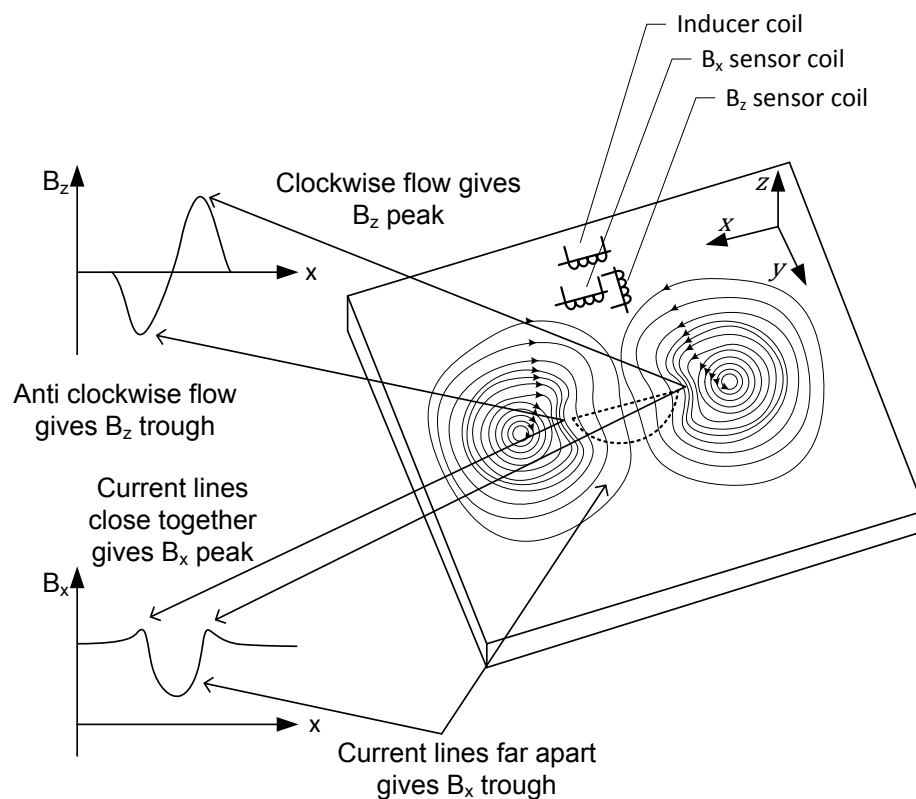


Figure 2.10 Illustration of the ACFM principle [53]. The eddy currents pass around the crack ends and down the faces of the crack opening. The graphs correspond to a 1D scan along the crack length.

2.3.8.1. Forward Problem

The interaction of magnetic and electric fields between air and a metal surface is governed by four pairs of partial differential equations known as the Maxwell equations, which must be solved simultaneously to give the electric and magnetic field distributions due to a defect with known geometry. This is hereafter referred to as the forward problem. Assuming the time dependency of the fields are harmonic (i.e. $e^{i\omega t}$), it can be shown that in the context of ACFM where the AC frequencies vary by up to 10 MHz, the displacement current (which is proportional to the frequency) is sufficiently small to be neglected. Therefore the equations describing the field variations are given as follows [57]:

$$\nabla \times E = -i\omega\mu H \quad (2.1)$$

$$\nabla \cdot E = 0 \quad (2.2)$$

$$\nabla \times H = \sigma E \quad (2.3)$$

$$\nabla \cdot H = 0 \quad (2.4)$$

within the conductor, and

$$\nabla \times E = -i\omega\mu_0 H \quad (2.5)$$

$$\nabla \cdot E = 0 \quad (2.6)$$

$$\nabla \times H = 0 \quad (2.7)$$

$$\nabla \cdot H = 0 \quad (2.8)$$

in the free space above the conductor. In the above equations E is the electric field, H is the magnetic field, σ is the conductivity of the specimen, ω is the AC frequency (rad/s), ∇ is the gradient operator and μ_0 and μ are the permeability of the free space and the conductor, respectively. The solution of the forward problem (i.e. the distribution of magnetic flux

above the surface when a single scan along the crack opening is performed), for a given crack geometry, involves combining equations (2.1) to (2.8) together with appropriate boundary conditions at the surface of the conductor and the faces of the crack. Lewis, et al. [57] demonstrated that the solution is dependent on a dimensionless number m (known as the Michael number) given as:

$$m = \frac{\mu_0 l}{\mu \delta}, \quad \delta = \frac{1}{\sqrt{\pi \mu \sigma f}} \quad (2.9)$$

where l is the crack length scale, δ is the skin depth (the depth at which current density reaches about approximately 37% of its surface value), f is the AC frequency (Hz). Small values of m correspond to ferromagnetic materials for which the $\frac{\delta}{l}$ ratio is also small. Conversely, for non-magnetic materials with a thin-skin effect, m is large. Lewis, et al. [57] then theoretically solved the forward problem for an artificial semi-elliptical crack and found good agreement with the experimental results for two limiting cases of very small and very large m . However, the complete solution for an arbitrary value of m was later given by Michael, et al. [58].

2.3.8.2. Inverse Problem

In the inverse problem, the ACFM response to an unknown crack is experimentally measured while the crack geometry is obtained by inverting the ACFM signal. The fact that the solution of the forward problem is highly nonlinear and may not be expressed analytically makes the inversion process very complicated. Because of this, an analytical solution yielding the crack geometry (pocket length) as a function of ACFM measurements may not be obtained. However, there are techniques that are being used at both research and industry

level to tackle this, such as optimisation, interpolation and neural network based approaches.

In the inversion of the ACFM signal using optimisation, the crack parameter to be predicted is given an initial value as the inverse solution and is updated iteratively until a reasonable tolerance of error is achieved. The update rule is based on the minimisation of a cost function which is generally the sum of the square of the predicted ACFM signal (using the forward model at the current solution) minus the measured ACFM signal, over the measurement points. This approach has been employed in a study by Amineh, et al. [59], [60] where they used a conjugate gradient method for the optimisation and used an existing forward model for a U-shaped inducer developed by Sadeghi, et al. [61].

They have used the same approach for prediction of the unknown sensor lift-off and found close agreement between the predicted and the true value of the crack pocket length for different lift-off values. However this method suffers from a shortcoming rendering it impractical at the industrial level; for non-linear cost functions with multiple minima, the optimisation may be stuck at a local minimum if the initial value is not carefully selected. Consequently, the optimisation terminates at the wrong solution value. Unless some procedures toward the initialisation of the desired parameter are implemented, the method would require an experienced user with superior knowledge about the technical aspects of the work. Further, the evaluation of the forward solution at each iteration step slows down the inversion process.

The interpolation technique is rather simple but more effective. It is a well-known method in industry and is preferred over other techniques where applicable due to its simple principle. It relies on a fairly large database containing the ACFM measurements for defects with a

given surface length and variety of geometrical aspect ratios. The database is constructed from simulation results of ACFM measurements over known crack geometry (usually a semi-ellipse is assumed) using a fast algorithm solving the forward problem [59, 60]. The alternative approach for constructing the database is to use FEM approaches to increase accuracy and reliability of the database. When the measurements are fairly close to each other, a linear interpolation is used to calculate the crack pocket length from the maximum ACFM signal drop ΔB_x as schematised in Figure 2.11.

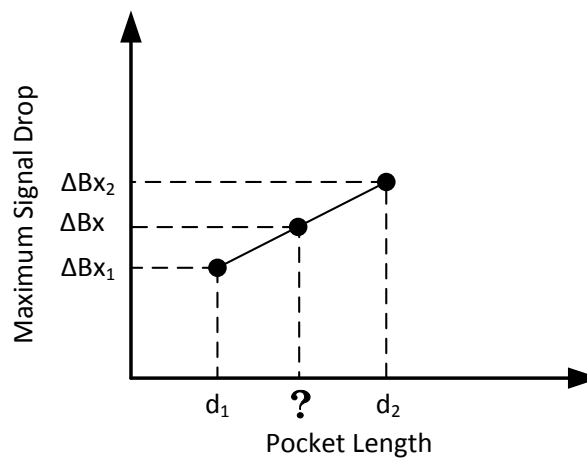


Figure 2.11 Illustration of ACFM signal inversion using table interpolation.

Therefore the unknown crack pocket length d is approximated as:

$$d = d_1 + \frac{(\Delta B_x - \Delta B_{x1}) * (d_2 - d_1)}{\Delta B_{x2} - \Delta B_{x1}} \quad (2.10)$$

where the subscripted letters denote the values stored in the database. Despite the fact that this approach offers acceptable accuracy in sizing defects (within 20% error), it suffers from uncertainty about the types of defects (i.e. unacceptable error in sizing complex RCF crack shapes as found in rails [3]) as it is impossible to create an inclusive database containing all the different types of defects that one could expect. In recent decades, the use of artificial

neural networks (ANN) for defect classification and characterisation has been one of the topics of research in the NDT community. Generally, ANN is the ideal choice for prediction problems where a limited number of measurements are available and the goal is to train an ANN so as to closely approximate the output (i.e. crack pocket length) for a given input (i.e. ACFM signal) which may fall outside the training database. Ravan, et al. [62] developed an ANN for inversion of the ACFM signal to crack pocket length profile from single ACFM measurements along the crack opening. They trained their ANN from the results of a fast simulator predicting the ACFM signal over a number of individual semi-elliptical multi hump cracks as shown in Figure 2.12.

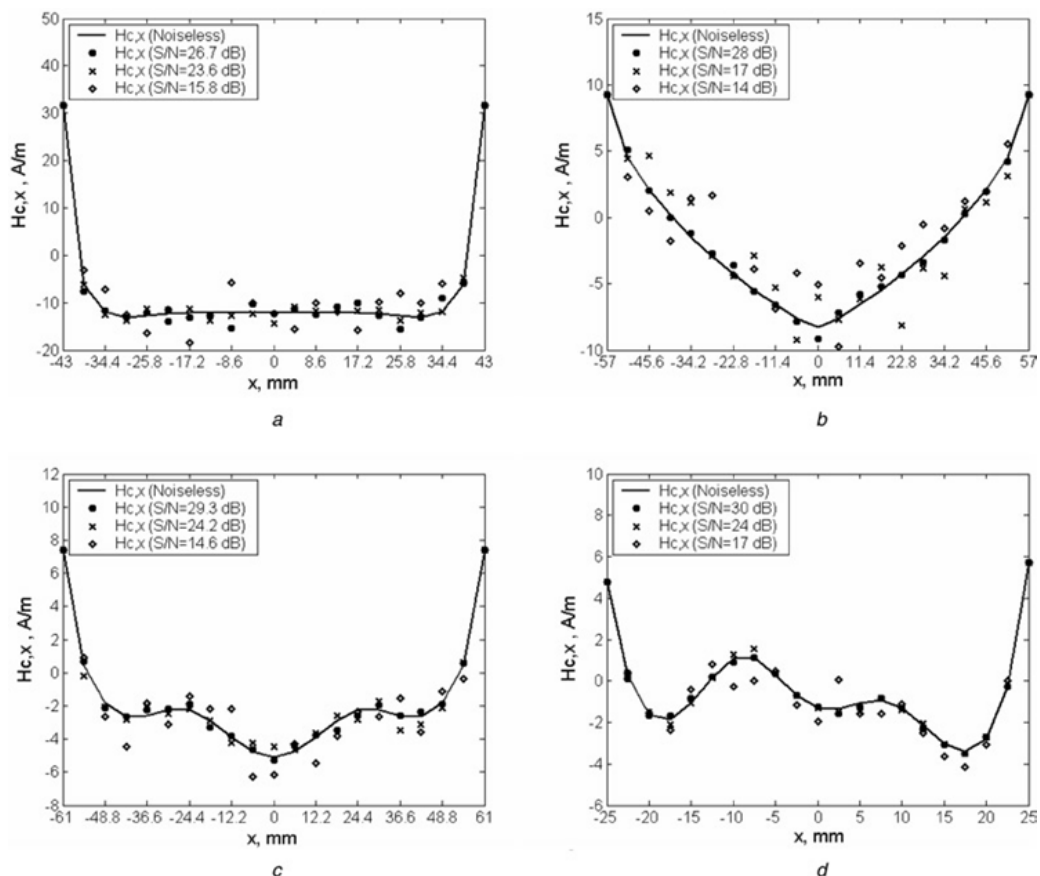


Figure 2.12 Variations of the real part of the crack signals, $H_{c,x}$ superposed by additive white Gaussian noise with various SNRs when scanning the cracks along $y_s = 0.5$ mm at lift-off distance $z_s = 0.1$ mm for (a) Rectangular depth profile (b) Triangular depth profile (c) Symmetrical triple-hump depth profile and (d) Asymmetrical triple-hump depth profile [62].

They demonstrated that their ANN can accurately predict the crack pocket length profile for several simulated and real measurements of ACFM over common or complex crack geometries that were not in the database. The performance of the ANN was also studied on several simulated measurements superposed by additive noise at a number of SNRs and it was found that the presence of noise would lessen the accuracy of inversion. While their approach works reasonably well at laboratory level for isolated multi-hump cracks, it may produce unacceptable error in sizing complex RCF crack shapes where the ACFM signal is not responsive to some part of crack geometry [3]. In addition this approach has not been used for clusters of RCF cracks, which are commonly seen in the rail industry.

Hasanzadeh, et al. [63] similarly used a fuzzy logic based approach for inversion of the ACFM signal to crack pocket length profile and achieved high accuracy from their inversion model (in the absence of noise) and proposed that their inversion algorithm may be used to compensate for the lack of a complete database. However, they also reported that while their method reduces the need for large database, it requires at least two cracks with the same length or depth to predict a piecewise linear equation. Besides, their results were based on laboratory rail samples which did not contain real RCF cracks.

Nicholson, et al. [3], [64] performed a FEM study on the ACFM response to light-moderate RCF cracks using COMSOL Multiphysics®. They modelled the RCF cracks as semi-ellipses of varying aspect ratios and found close agreement with the experimental ACFM measurements. Based on the simulation results, a sizing curve was then constructed which may be used for inversion of the ACFM signal to crack pocket length when the crack's surface length is known (Figure 2.13). The calculation of crack pocket length relies on the assumption of a semi-elliptical crack, which has been found to be valid for light and some

moderate RCF cracks in rail [9], i.e. surface lengths up to 20 mm [12]. Thus, for more complex geometries where this assumption does not hold, the pocket length may be over/under estimated by a greater margin of error. They also investigated the ACFM response to a crack when there is an angle offset between the ACFM probe and crack surface length - hereafter referred to as a non-matching case - at a range of angles (Figure 2.14) and found that for angle offsets beyond 10° , the reduction in the ACFM B_x signal drop due to the crack is significant enough to cause an unacceptable error in sizing the defects (i.e. error > 20%). The larger the angle offset, the larger the error in sizing the crack and thus it is crucial to know the crack orientation (within $\pm 10^\circ$). The knowledge of angle offset becomes very important when unmanned automation of ACFM for crack characterisation is desired.

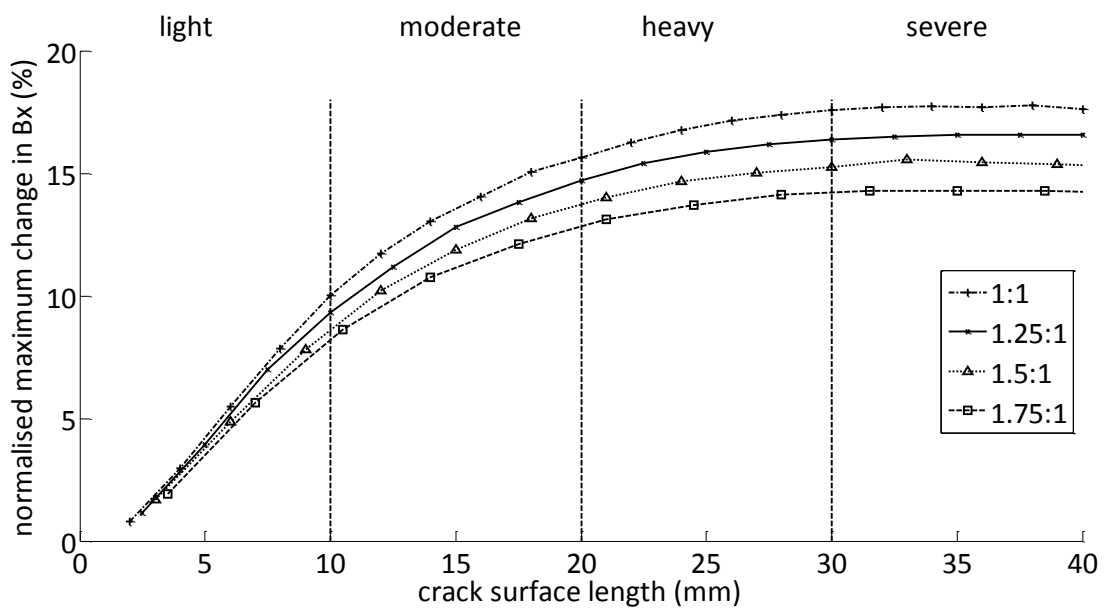


Figure 2.13 Normalized maximum change in B_x value against crack surface length at zero lift-off for semi-elliptical cracks of elliptical ratios 1:1, 1.25:1, 1.5:1 and 1.75:1 [3].

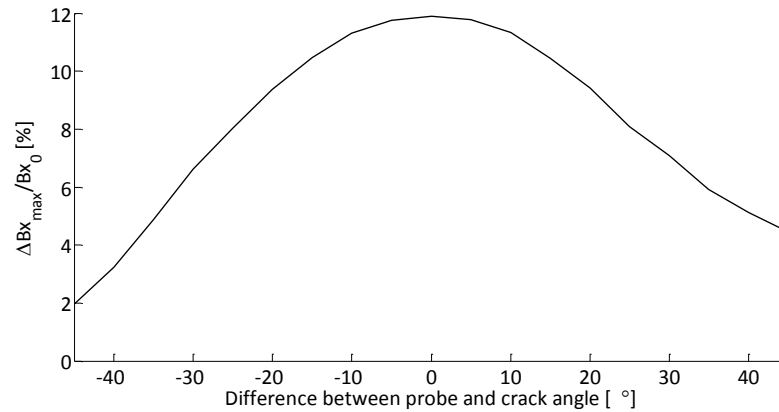


Figure 2.14 The sensitivity of the maximum change in B_x value at zero lift-off to changes in the orientation of the ACFM probe relative to surface crack angle for a 15 mm surface length, 5 mm pocket length semi ellipse [65].

2.3.8.3. Application of ACFM in the Railway Industry

The first commercial ACFM instrument for use in the rail industry was developed through a joint effort between Bombardier Transportation and TSC Inspection Systems [66]. They developed an ACFM walking stick device that could be used to manually detect and characterise surface breaking defects in rails (Figure 2.15). The device consists of a user interface unit (usually a dedicated laptop), an AMIGO ACFM instrument unit, an array ACFM probe and an odometer for measuring the distance travelled.

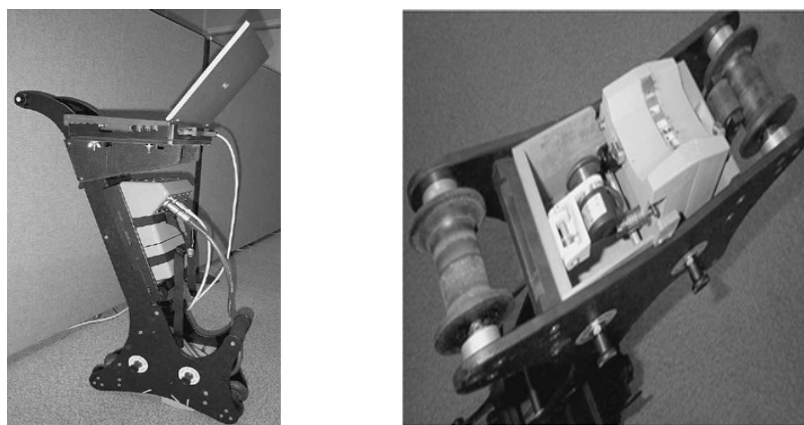


Figure 2.15 Image of the Bombardier and TSC ACFM walking stick [66].

Papaalias, et al. [54] have investigated the possibility of using ACFM sensors for inspection of surface breaking defects in rails at high speed. Their experiment was carried out on a spinning test piece containing several single spark eroded notches (Figure 2.16). The experiment used a high frequency 50 kHz single probe developed by TSC Inspection Systems along with dedicated high-speed data acquisition hardware. It was found that under constant lift-off conditions, the detectability of defects remained unaffected by the increase in the inspection speed and the defects were detected at speeds up to 121 km/h (Figure 2.17).

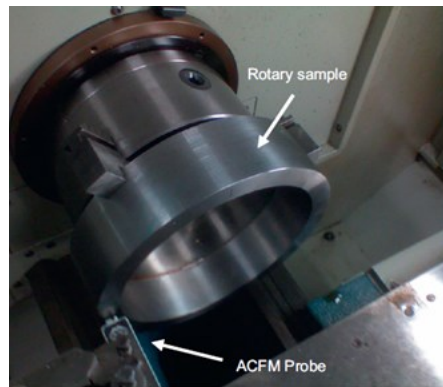


Figure 2.16 Experimental setup for the turning lathe tests using the rotary test piece [54].

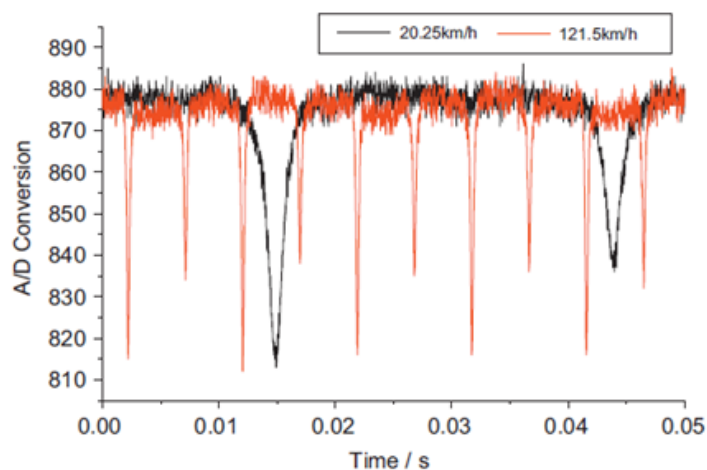


Figure 2.17 ACFM data plots showing the resulting signals at 20.25 and 121.5 km/h with 0.8 mm lift-off. The different signals (magnitude of A/D conversion signal change) are for machined defects of 4 mm and 2 mm depth [54].

A similar experiment was also conducted on a rotating rail rig containing clusters of artificial RCF defects (ranging from 2 to 15 mm in pocket length) at different spacings, to mimic the real scenario of rail inspection (Figure 2.18). A specially designed trolley was used to hold the ACFM probe in place; however during operation there was significant lift-off variation during the rotation of the rig. It was found that the defects were detected at moderate speed (30 km/h) even in the presence of the significant lift-off change (up to 5 mm), although some of the multiple defects could not be resolved from the ACFM signature and the amplitude of the signal was found to be dependent on the number of defects in a cluster (Figure 2.19). Further, as the sensor lift-off increased to about 8 mm (due to a further increase in the inspection speed), some defects went undetected [54]. Recent work has been carried out to include an ACFM sensor on a train for high speed inspection but no results have yet been published [67].

In conclusion, detection of surface breaking defects using ACFM at high speed is possible; provided that sensor lift-off variation is minimised, or at least known. During high speed inspection using the EC method, the EC probe is held in place by a rigid housing between the train's wheel sets where the lift-off variations due to bogie dynamics is a minimum, this approach would also be appropriate for ACFM inspection. When lift-off change occurs a variable background signal is observed, which means that simple methods to automatically detect cracks, such as the threshold method, become inappropriate, thus a more sophisticated signal processing technique must be considered.

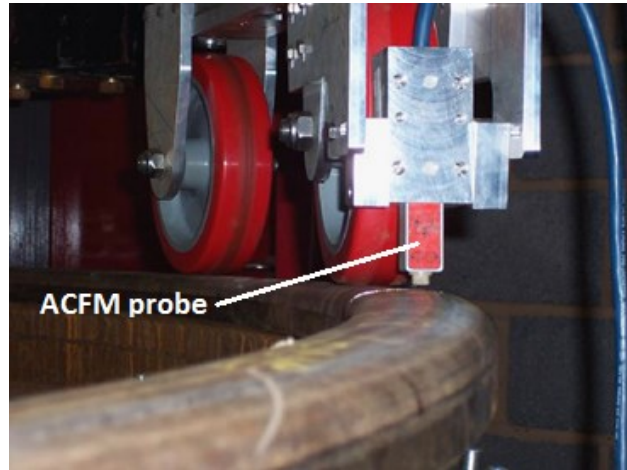


Figure 2.18 Experimental setup during the spinning rail rig tests [54].

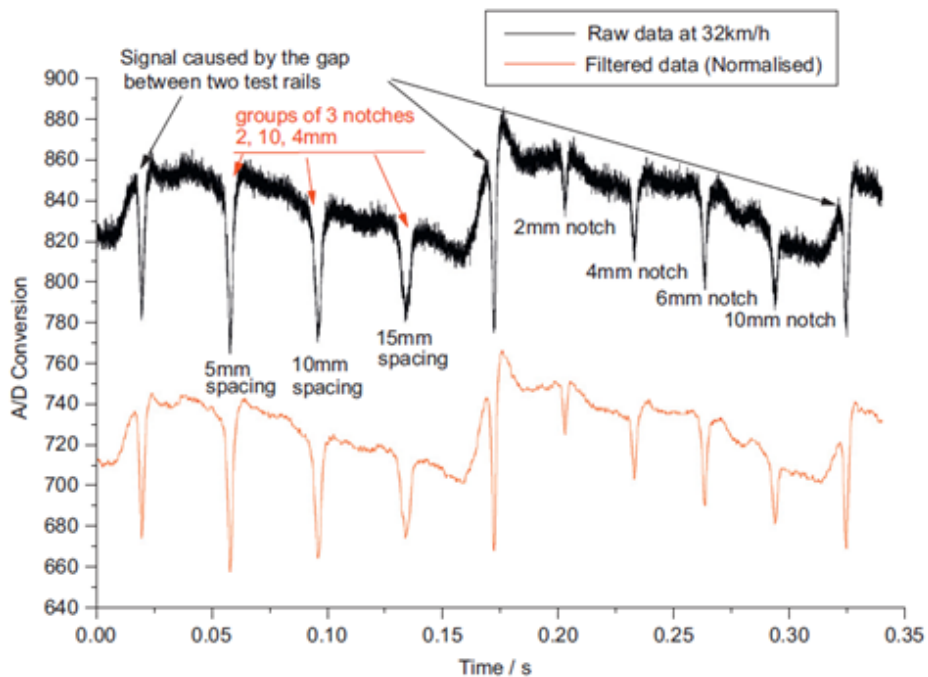


Figure 2.19 Raw and normalized filtered data plots for test rails where the 5, 10 and 15 mm spacing refers to the distance between each defect for clusters of three defects of varying depth (2, 4, 10 mm) [54]. The defects used in this experiment are later explained in Chapter 5 (Figure 5.11).

2.4. Robotic NDT

In recent decades, with the enhancement of sensor technology, robotics and artificial intelligence (AI), there has been a great desire from industry to use robots for inspection and

quality monitoring [68-82]. This is due to several shortcomings arising from manual inspection using human operators such as high level of subjectivity, tediousness of operation, high risk of operation in hazardous environments and high costs associated with training skilled operators. An example is the oil and petrochemical industry where the use of in-pipe inspection robots has been commonplace [83]. These robots may be used to either repair damaged welds in the interior surface of the pipe or inspect the surface of pipe for defects. Choi, et al. [84] developed a robotic system for inspection of underground urban gas pipelines utilizing UT sensors. The robot has excellent flexibility in order to steer in pipelines with different configurations such as in branches and elbows (Figure 2.20). It is being further developed to use different NDT sensors for inclusive assessment of pipelines.

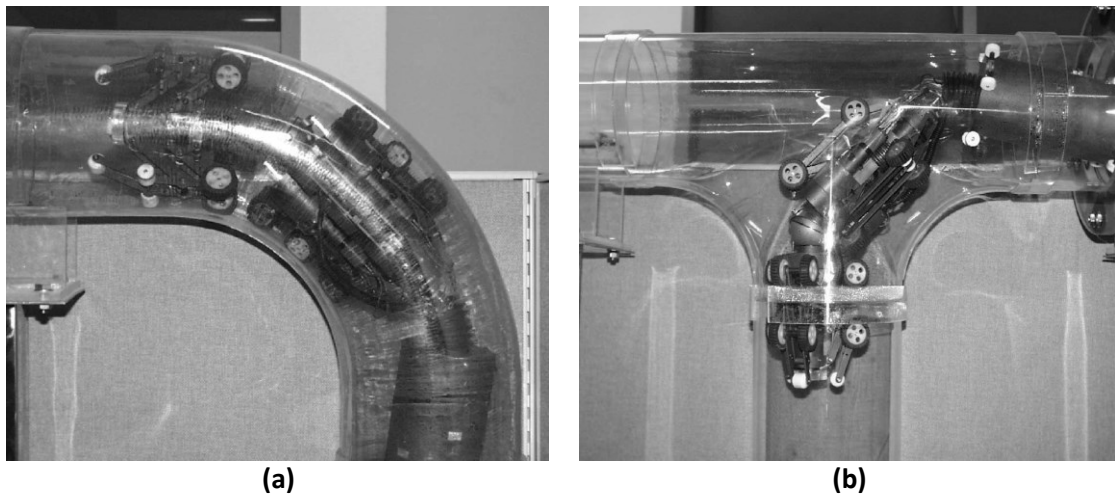


Figure 2.20 Pipeline inspection robot using a UT sensor adapting to different configurations: (a) elbow and (b) branch [84].

Miller, et al. [85] also developed a robotic system for automatic monitoring of weld quality on metal components using an EMAT sensor. The system consists of a laser ultrasound signal generator and EMAT reception system (Figure 2.21). The laser generates an ultrasound pulse on one side of the specimen and an EMAT receptor is placed on the other side of the

specimen to measure the time of flight (TOF) of the ultrasound signal in order to evaluate the weld quality. They proved that their system can be used to measure weld reinforcement distance and therefore monitor and control weld quality in real-time.

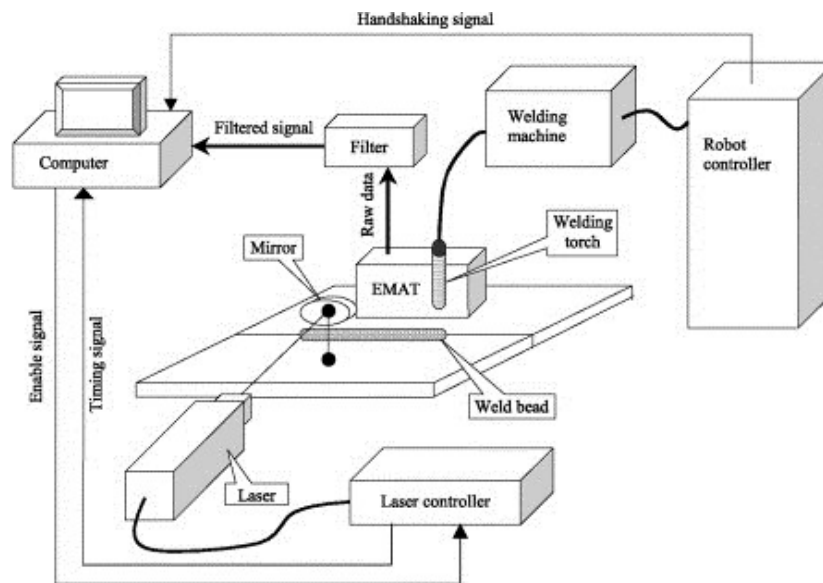


Figure 2.21 Automatic monitoring of weld quality using the EMAT technique [85].

Sattar, et al. [77] developed a robotic system for under-water inspection of oil tanks using an ACFM array probe for assessment of the weld surface (Figure 2.22). The robot is capable of maintaining its equilibrium and aligning its position over the weld surface by using four ultrasonic sensors. It is designed to operate both in air as well as under-water. The buoyancy tank on top of the robot maintains the robot's balance through adjusting the buoyancy near to equilibrium by controlling its mass. The depth at which the robot operates is regulated using a depth sensor. The propulsion system consists of a servo controller along with a position encoder which gives position and velocity feedback to the robot's main controller. Depth and horizontal position is controlled simultaneously to steer the robot to the inspection site on a wall or above a floor area.

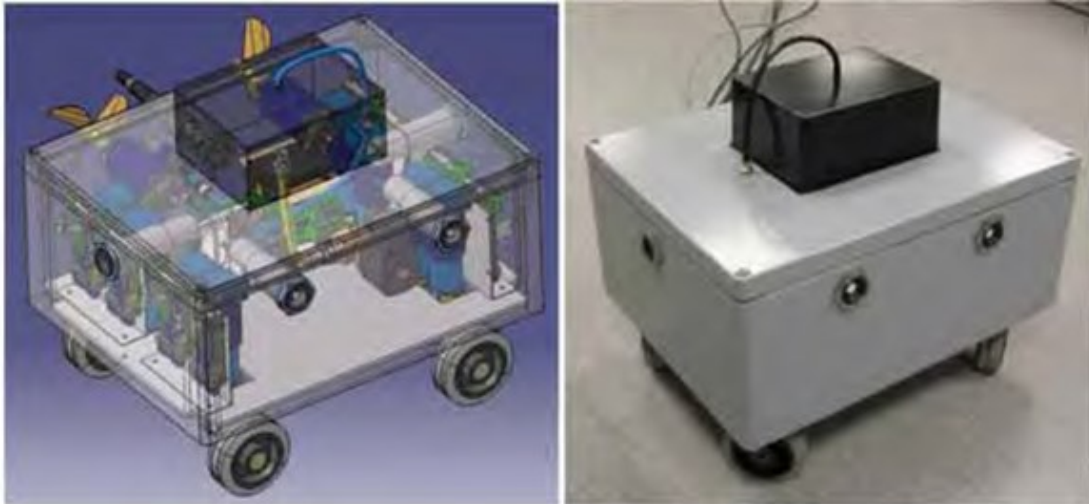


Figure 2.22 Underwater robotic system using an ACFM array probe developed by Sattar, et al. [77].

They also developed a ring climbing robot prototype for inspection of offshore wind turbine blades using X-ray tomography in order to detect and characterise internal defects. The robot was primarily designed to reduce the high inspection cost and risk for human operators [78]. It can move in three different ways (straight up-down, spiral and rotation at constant height) by using adhesion forces provided by springs which push it against the climbing surface (Figure 2.23a). This has the advantage of reduced cost and simplicity of operation over other existing solutions used for climbing robots (e.g. vacuum suction, air vortex or magnets) [78]. The robot can therefore orient itself around the wind turbine blade at a given height and perform a series of 2D X-ray measurements over the desired section of the blade. 3D X-ray measurements are made possible by taking advantage of the rotation of the turbine blade along its long axis (Figure 2.23b).

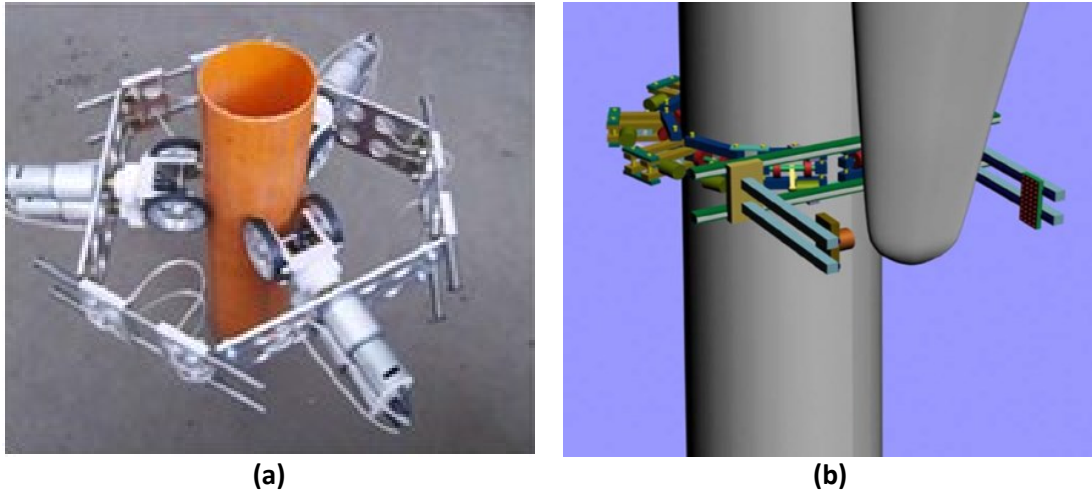


Figure 2.23 (a) Demonstration of the ring climbing robot prototype used for inspection of wind turbine blades (b) Conceptual design for full scale climbing robot that takes tomographic scans by using rotation capability of the turbine blade along its long axis [78].

The idea of robotic NDT can be extended to the rail industry. According to the literature, this is not yet a broad area of research, as most rail inspections are carried out by human operators or by train mounted inspection systems. Although automation of rail inspection for defect detection has been made possible using trains carrying non-contact NDT sensors (e.g. EC, UT, EMAT), the defects found would need to be re-inspected by a skilled operator (using a walking stick type systems) for the detailed data needed for crack sizing. Therefore there is a gap for an unmanned system, which could replace human operators and perform faster inspections, while the reliability of the inspection is not sacrificed. To date, automation of defect sizing has not yet been made possible because of several technical problems as follow:

- Interpretation of data collected from NDT sensors is complex. For example, in the case of the EC method, the sensor may also respond to changes in the rail's metallurgical properties and therefore the location of the defect found needs to be confirmed visually;

- Uncertainties about unknown defects makes automatic sizing very challenging. For example, in the case of EC, MFL and ACFM the direction of induced current /flux would have to be normal to the crack length in order to produce optimal data for sizing;
- Fundamentally, developing robots for automation of defect sizing requires multi-disciplinary knowledge and access to different resources which must be gathered together in order to achieve such a system. Designing a system which keeps user interaction to a minimum in a semi-constrained environment as in the railway industry, demands expert's knowledge which must be implemented on machines. This makes it very challenging to achieve at the industry level.

Recent research has proved that ACFM is a good candidate for automation of rail inspection (for both detection and sizing) for RCF cracks, as discussed in section 2.3.8. However, in order for an unmanned system to collect reliable and accurate data for an unknown crack on a rail which may be subject to an unpredicted level of wear, the following requirements have to be met:

- The ACFM scan must be performed at a constant lift-off;
- The ACFM scan must be performed along the crack opening;
- The ACFM probe must be oriented normal to the rail surface.

These requirements have been graphically explained in Figure 2.24.

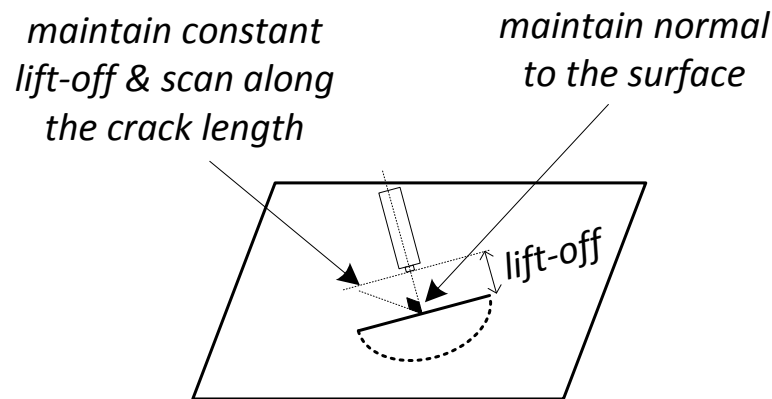


Figure 2.24 Graphical illustration of automatic ACFM scan for crack sizing.

2.5. Summary

In this chapter the current state of rail inspection using the NDT techniques along with their associated signal processing has been reviewed, a summary is presented in Table 2.1. Each technique has its own strength making it suitable to target a specific type of defect for either detection or characterisation or both depending on the nature of the technique used. For an inclusive assessment of the rail, however, different NDT techniques may be combined together (known as NDT data fusion [26, 86]).

RCF cracks are a major concern to the rail industry and should be taken more seriously than before as the demand for higher speed and axle load trains is increasing.

Amongst other NDT techniques (e.g. MFL, EC and PEC), ACFM has shown to be most feasible for both detection and characterisation of RCF cracks due to its combined advantages as discussed earlier in this chapter.

At present, expert rail inspectors are used in order to manually verify the defects detected at speed. This must take place before any decision on track maintenance is made in order to minimise track down-times and also unnecessary repairs due to non-critical defects. The

combined advantages of the ACFM technique enables its automation and hence, robotics and AI can be combined together to enhance the speed, reliability and accuracy of the automated ACFM inspection.

Table 2.1 Summary of the NDT methods and their associated signal processing.

Method	Signal processing	Applications
VI	<i>Image processing + machine vision technology [19], Image processing + local normalisation [18]</i>	<i>Rail component detection and defect identification, discrete surface detection</i>
UT guided waves	<i>WT + ANN [34, 87], WT + SVM [35]</i>	<i>Automatic detection and classification of transverse and oblique defects</i>
EC, PEC	<i>FT + WT + ANN + SVM [43, 88], WT + time heuristic + inverse filtering [38]</i>	<i>Automatic detection and classification of surface and near surface defects</i>
MFL	<i>WT [89, 90]</i>	<i>Automatic detection of vertical split head type defects in rails</i>
ACFM	<i>Fuzzy logic [63], Non-linear optimisation [59, 60], ANN [62, 91]</i>	<i>sizing of surface breaking cracks, estimation of crack depth profile</i>

Chapter 3. Development of a Robotic System for Inspection of RCF Cracks in Rails

3.1. Introduction

The primary aim of this research is to develop an unmanned system to enable automation of RCF crack inspection using the ACFM technique. Specifically, a robotic trolley is desired which should be capable of performing both detection and characterisation where the former is used to locate RCF cracks in rail while the latter is needed to collect more detailed data on the unknown cracks for accurate sizing. These functionalities may be performed by machines provided they are given the required knowledge.

For detection scanning, the necessary knowledge are the initial ACFM sensor lift-off, initial orientation of the ACFM sensor with respect to the rail length, the inspection distance and speed which are all fixed throughout the detection process. For characterisation scan, the ACFM sensor trajectory, orientation of the ACFM sensor relative to the defect and scanning speed are the required knowledge. These are (except the last one) not initially known due to uncertainties in rail profile and defect's orientation which may cause significant sizing inaccuracy, if not accounted for.

Therefore, the main objective of this research is the design of a platform for implementing the necessary AI and its integration with a machine which is capable of performing inspection tasks and also minimising its reliance on expert operators, especially when the knowledge is not present. This need has been accomplished by developing a robotic trolley utilising a number of commercially available and developed hardware components, sensors,

sophisticated signal processing/algorithms and a software interface developed for unmanned control of the robotic trolley.

3.2. Rule-Based Expert System

In a rule-based expert system (RBES), human knowledge is given to machines as a rule that is *“defined in an IF-THEN structure that relates given information or facts in the IF part to some action in the THEN part”* [92]. In these rules, the IF parts are called the antecedent (premise or condition) while the THEN part is called the consequent (conclusion or action) [92]. A rule can generally be constructed by combining many antecedents joined by the logical AND (conjunction), OR (disjunction) or both. It should be noted that the action may represent relations, recommendations, directives, strategies and heuristics [92].

In RBES, an inference engine (i.e. computer software) is used to derive the actions from the knowledge base (i.e. IF-THEN rules) which in turn acts on the facts that are provided either by prior knowledge or by sensor measurements. The explanation facility informs the user of the rules that are being fired and also it keeps track of how the system arrived at a certain conclusion. It also helps with troubleshooting and debugging the system upon its failure. This is facilitated by, for example, displaying a specific message on the user interface or by an event logging mechanism. Figure 3.1 shows the block diagram representation of a RBES.

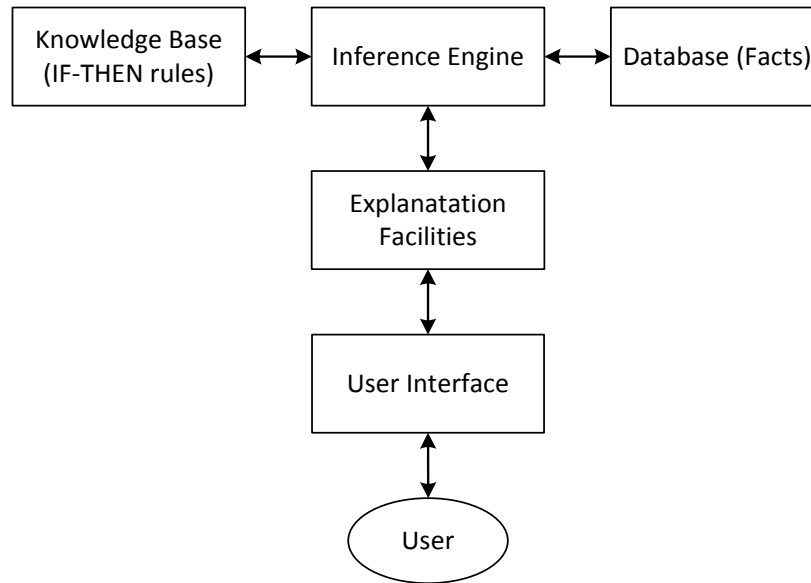


Figure 3.1 Structure of a rule-based expert system [92].

Researchers have applied RBES to a wide range of applications including: production planning [93], automobile process planning [94], system development [95], knowledge representation [96], communication system fault diagnosis [93], probabilistic fault diagnosis [97] and robotics [98], just to name a few. RBES is an ideal choice for domain specific problems where knowledge is directly tied to the inference engine (i.e. no separation between knowledge and problem solving) and is therefore very feasible for implementation [92]. Its disadvantages, however, are (a) it fails once the application domain is expanded (b) updating the knowledge base requires re-programming.

3.3. Software/Hardware Developments and Methods

To serve the purpose of this research, using C++, intelligent user interface (IUI) software has been developed (Figure 3.2). The software has been based on the conventional RBES as the aim is to develop a system specifically for rail inspection with predetermined functionalities.

The IUI is used to autonomously control the inspection trolley as shown in Figure 3.3 and serves as an inference engine where all the real-time data logging, analysis, optimisation, decision making and supervision occur. It exploits the multi-threading capability of the C++ language (best performed on a multi-core CPU computer) so as to communicate with the sensor and actuator agents concurrently. Figure 3.4 shows the block diagram of the IUI.

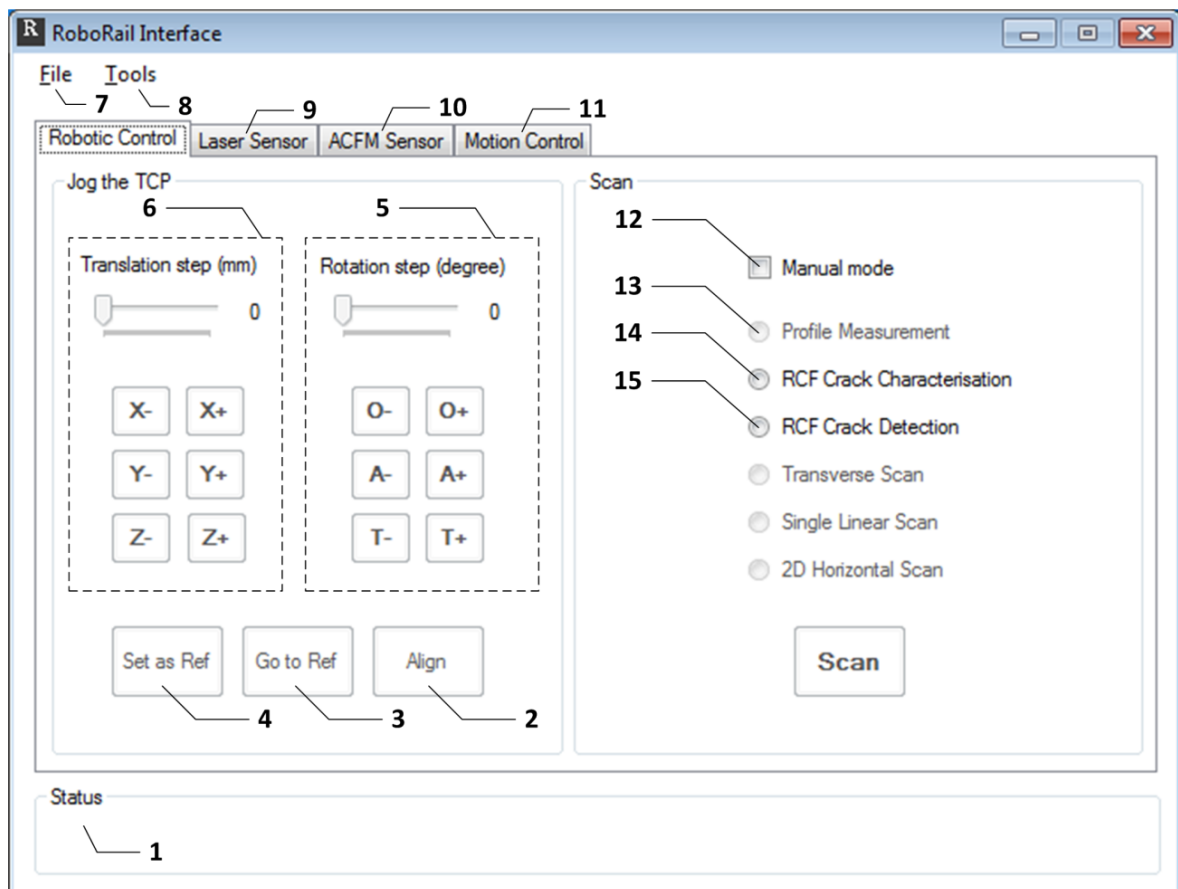


Figure 3.2 Screenshot of the developed IUI software. Labels: 1→ explanation facility, 2→ function for aligning the robot’s tool centre point with the global coordinate system (manual mode), 3→ function for moving the tool centre point to a predetermined reference point (manual mode), 4→ function for setting the current location as a reference point (manual mode), 5→ functions for changing the alignment of the robot’s tool centre point relative to its current pose defined by three rotational components (manual mode), 6→ function for translating the tool centre point relative to its current location defined by three linear components (manual mode), 7-11→ see Appendix, 12→ function for switching between manual and automatic mode, 13→ function for measuring the rail head profile (manual & automatic), 14→ function for performing a 3D ACFM grid scan following the rail head profile at a constant lift-off (manual & automatic), 15→ function for performing an ACFM detection scan along a rail at a constant speed using the motorised trolley (automatic mode).

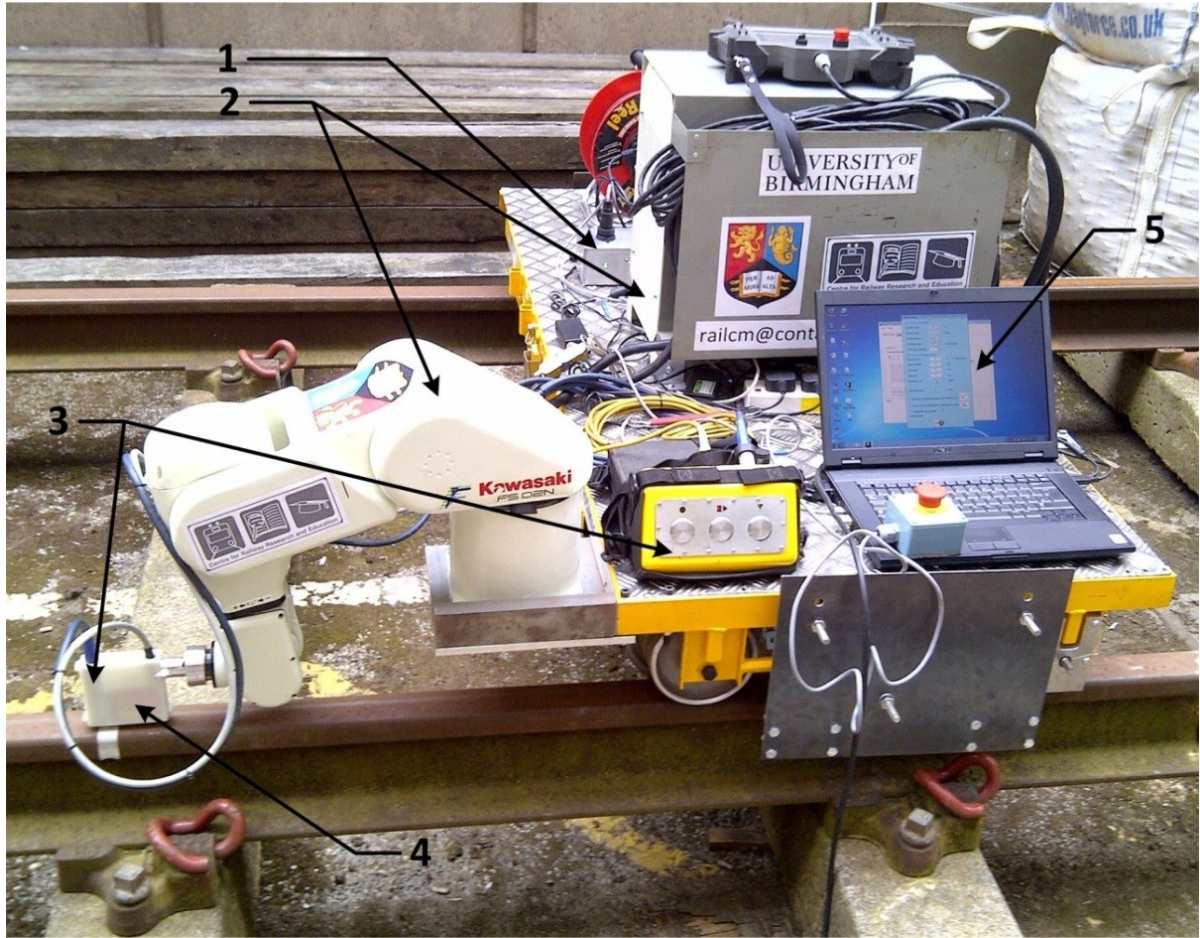


Figure 3.3 Image of the developed robotic trolley at the University of Birmingham. Labels: 1→ Motion Controller Agent, 2→ Robot Arm Agent, 3→ ACFM Sensor Agent, 4→Laser Sensor Agent, 5→ IUI Software.

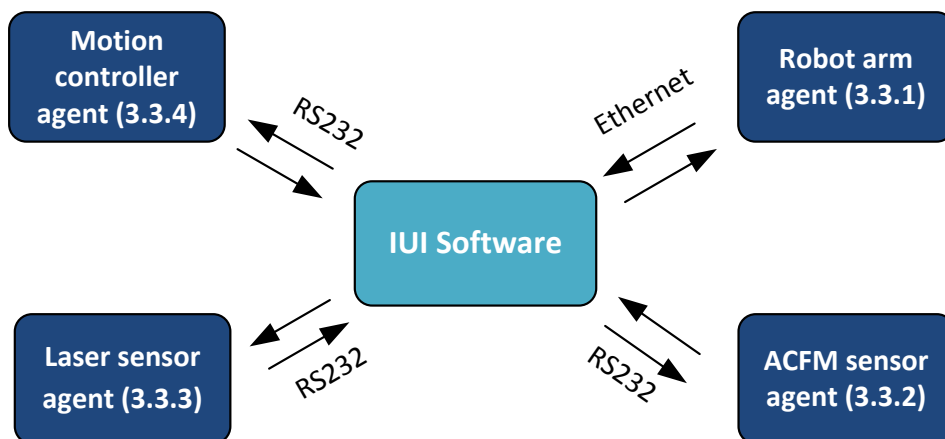


Figure 3.4 The block diagram representation of the IUI software communicating with the sensor and actuator agents. RS232 is the standard protocol used for serial communication with a PC.

The laser sensor, ACFM sensor and robot arm are commercially available, whereas the motion controller agent has been developed by the author. The IUI operates in either manual or automatic mode. The manual mode has been extensively used to acquire ACFM measurements in the laboratory (static test) and also to demonstrate the following functions:

- Robot arm alignment and calibration with respect to the rail;
- Rail profile measurement and conditioning;
- 1D/3D ACFM scan using the robot arm over defects following the measured rail profile at the user specified lift-off value;
- Crack surface angle calculation from 3D ACFM grid scan data.

The automatic mode is designed for dynamic inspection of a rail and includes both detection and characterisation scans. In this mode the IUI acts in a supervision mode where it automatically controls the flow and order of the mentioned functionalities.

The sensor and actuator agents used in the robotic rail inspection system are controlled by software agents which are essentially routines. These are the main routines that run on separate threads dedicated to them and are created upon request from the main supervisory thread. This allows the agents to be controlled simultaneously, resulting in improvement of the software's real-time performance and reduction of latency. However, there are cases where some routines would have to wait for others to finish processing. The number of required routines is dependent on the nature of the task requested by the user. These are illustrated in Table 3.1. The main routines may also call other sub-routines which are hidden from the user.

Table 3.1 Explanation of the software agents (routines) used to communicate with the hardware (sensor and actuator) agents. Parallel blocks represent the multi-threading characteristics.

Tasks	Name of routine	The order in which hardware agents are accessed	Prerequisite
Robot arm calibration	"Calibrate"	Laser sensor Robot arm	-
Rail profile measurement	"MeasureProfile"	Laser sensor Robot arm	Call to routine "Calibrate"
3D ACFM scan over rail	"RScan"	ACFM sensor Robot arm	Call to routine "MeasureProfile"
Automatic detection scan	"LScanDetect"	ACFM sensor Motion controller	The user must input the corresponding data
Automatic characterization scan	"AutoScan"	Motion controller Laser sensor Robot arm ACFM sensor Robot arm	The user must input the corresponding data

3.3.1. Robot Arm Agent

The ACFM sensor, from the point of view of automatic RCF crack characterisation, needs to be given enough flexibility so as to adapt itself with different conditions arising from either changing rail track geometry (due to wear) or unknown RCF crack (e.g. varying crack surface angle) which may not be predicted. Specifically, a robot with at least five DOF is required in order to meet the requirements set out earlier in Chapter 2 (section 2.4). The required DOFs are explained in Table 3.2 with regards to a fixed Cartesian coordinate reference frame *XYZ* where the *X* axis is aligned with the rail length.

Table 3.2 Explanations of the DOFs required by the ACFM sensor for automatic RCF crack characterisation.

DOF No.	Purpose
1	<i>Moving the ACFM sensor along X axis</i>
2	<i>Moving the ACFM sensor along Y axis</i>
3	<i>Moving the ACFM sensor along Z axis</i>
4	<i>Aligning the ACFM sensor parallel to the crack length</i>
5	<i>Aligning the ACFM sensor normal to the rail surface</i>

These necessities have been facilitated by using an existing six DOFs Kawasaki FS02N robot arm which is equipped with a controller. It is worth mentioning that, desirably, a customised robot fit for purpose could have been developed. However, this has not been considered in this research due to time limit.

The robot may be controlled by calling a series of instructions written in the AS language. These instructions are transmitted to the robot through the TCP/IP internet protocol. Multiple instructions may be also executed by calling a dedicated program saved in the robot's memory which stores all the desired instructions. This approach is beneficial where the number of instructions is relatively high and it therefore offers faster execution because of reduced data transfer time. The instructions may be a movement or sending feedback on a desired parameter such as the tool centre point's position or orientation. There are two modes of movements defined for the robot; they are *LMOVE* and *JMOVE*. The former initiates a linear interpolated motion and the robot tool centre point moves along a straight line path whereas the latter initiates a joint interpolated (point-to-point) motion. The robot moves in a path that interpolates respective joint angles between the current position and

the destination position. However, in this study, the *LMOVE* mode is used since the linear motion between consecutive data points on the rail head is desired; moreover, the target position and orientation of the robot's tool centre is known (through *a priori* rail profile measurement and calibration of alignment).

3.3.1.1. Robot's Coordinate System

The position of the robot's tool centre point can be represented either by six joint angles or by defining its 3D position along with orientation, altitude and tool (*OAT*) angles all measured with respect to the fixed *XYZ* reference frame at the robot base as illustrated in Figure 3.5. The positions can either be defined with respect to the fixed reference frame *XYZ* or they can be defined with respect to the robot's tool reference frame *xyz* which is referred to as a compound transformation. When the latter is used, all the data points are measured with respect to a reference point (Figure 3.6). This is quite advantageous in dynamic environments where objects change their position with respect to the robot. Using the compound transformation, the data points on the desired object can be easily accessed by updating only the position of the reference point.

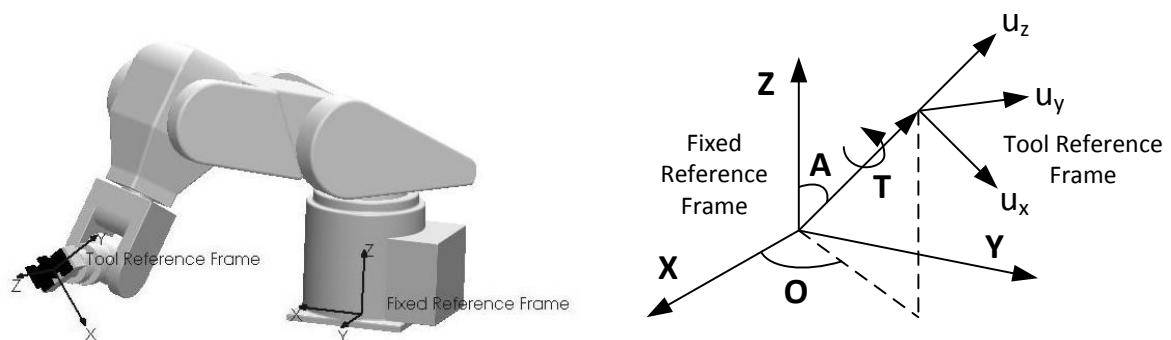


Figure 3.5 Illustration of the Kawasaki FS02N robot arm and its coordinate system.

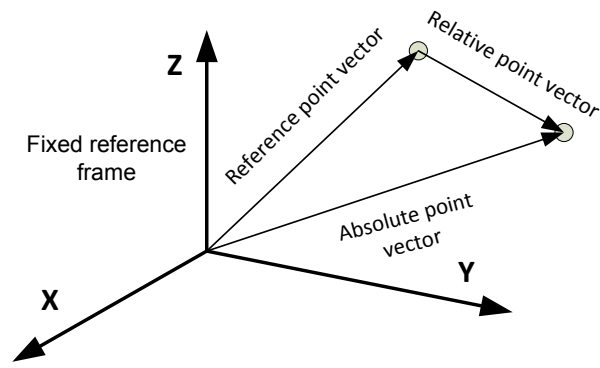


Figure 3.6 Illustration of compound transformation.

3.3.1.2. Data Transformation

The profiles of rails to be inspected will be measured by the laser sensor agent in terms of discrete data points in a 2D Cartesian coordinate system with respect to the robot's fixed reference frame XYZ (explained later in section 3.4.2). The OAT angles are then calculated in the software in such a way as to satisfy the following conditions:

- The ACFM probe needs to be normal to the rail head profile;
- The ACFM probe's orientation needs to match the crack surface angle.

These conditions are illustrated in Figure 3.7.

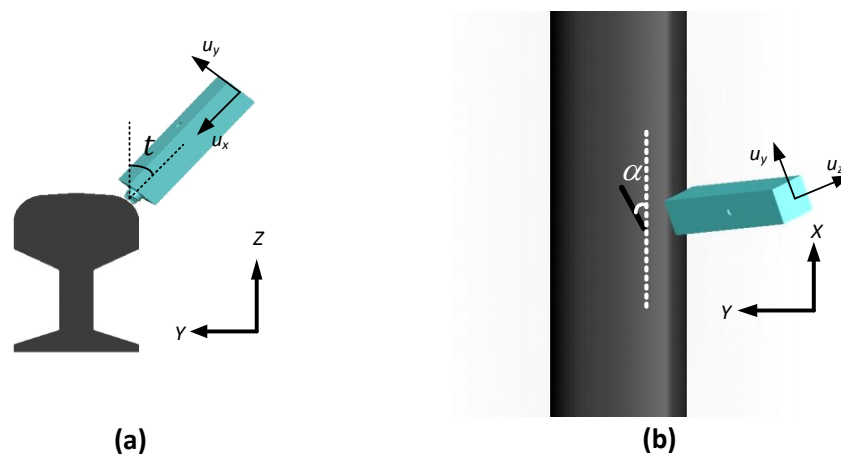


Figure 3.7 Graphical representation of the ACFM probe's conditions being: (a) normal to rail surface and (b) parallel to the crack opening.

The above conditions are mathematically expressed as:

$$\vec{u}_z = \begin{bmatrix} \sin(\alpha) \\ -\cos(\alpha)\cos(t) \\ -\cos(\alpha)\sin(t) \end{bmatrix}_{3 \times 1} \quad (3.1)$$

where \vec{u}_z is the tool reference frame's z direction measured with respect to the robot's fixed reference frame XYZ , α is the crack surface angle with respect to the rail length and t is the angle of tangent line to the rail head profile with respect to Y axis, at the desired point.

Using the OAT notations, it follows that:

$$\vec{u}_z = \begin{bmatrix} \sin(A)\cos(O) \\ \sin(A)\sin(O) \\ \cos(A) \end{bmatrix}_{3 \times 1} \quad (3.2)$$

Equations (3.1) and (3.2) may be solved simultaneously to give the angles O and A . As anticipated, it can be observed that the tool angle T has no effect on the \vec{u}_z direction. However, it appears in the tool reference frame's x direction \vec{u}_x with respect to the fixed XYZ frame given as:

$$\vec{u}_x = \begin{bmatrix} \cos(A)\cos(O)\cos(T) - \sin(O)\sin(T) \\ \cos(O)\sin(T) + \cos(A)\cos(T)\sin(O) \\ -\sin(A)\cos(T) \end{bmatrix}_{3 \times 1} \quad (3.3)$$

The tool angle T may then be obtained by setting the x component of \vec{u}_x direction to zero in order to orient the ACFM probe normal to the rail surface. Therefore, the OAT angles are calculated in the software in the closed form as:

$$\begin{cases} O = \tan^{-1}(-\cot(\alpha)\cos(t)) \\ A = \cos^{-1}(-\cos(\alpha)\sin(t)) \\ T = \tan^{-1}(\cos(A)\cot(O)) \end{cases} \quad (3.4)$$

In Equation (3.4), α is fixed while t varies across the rail head and needs to be updated for every single point on the rail head profile. Using the compound transformation, the points on the rail profile may be given as:

$$\begin{bmatrix} P_x \\ P_y \\ P_z \end{bmatrix} = R_Y \left(\frac{\pi}{2} \right) * \begin{bmatrix} 0 \\ P_Y \\ P_Z \end{bmatrix} \quad (3.5)$$

where R_Y is the 3D rotation matrix about the Y axis and P_Y and P_Z are the Y and Z coordinates of the rail profile at a certain point measured with respect to the fixed frame. Therefore the points are given to the robot as:

$$P_i = (P_x, P_y, P_z, O, A, T); i = 1 \dots n \quad (3.6)$$

where n is the number of the points on the measured rail head profile. The robot arm controller then computes the corresponding individual joint angles through its built-in inverse kinematic model.

3.3.2. ACFM Sensor Agent

The 5 kHz single probe ACFM sensor (Figure 3.8a) along with the AMIGO instrument (Figure 3.8b) supplied by TSC Inspection Systems have been used in this research. The sensor features two coils measuring the component of magnetic flux in two directions B_x and B_z . It interfaces to a PC via a standard RS232 serial port at 19200 bps and can be set to either sample the data (16 bits resolution) once or continuously at a controlled interval (minimum 10 ms). The latter has been used as it best suits the application. The sensor can be also set to output the moving average data over an adjustable number of data points (the default is 20). This helps to improve the resolution of the data when the speed of the probe's movement is relatively low (20 mm/s with the robot arm). However, for the detection scan

where the robot arm is fixed and the trolley moves at much higher speeds (e.g. 5 km/h) this value has been set to its minimum. The maximum inspection speed v_{max} (km/h) is dependent on operating frequency of the ACFM probe and can be approximated by the following equation:

$$v_{max} = \frac{f * d}{3.6} \quad (3.7)$$

where f is the sampling frequency (kHz) and d is the ACFM signal wavelength (mm) due to a crack. For a 50 kHz probe and a wavelength of 10 mm, the maximum inspection speed is approximately 139 km/h provided that the sampling frequency is the same as the operating frequency. In practice, however, the actual limit is lower than the predicted value as the sampling frequency is reduced to improve the signal quality (e.g. down-sampling and averaging). The sensor transmits the data in packets of seven bytes, Table 3.3. The IUI dedicates a separate thread for ACFM data sampling which is initialised before the ACFM scan is started.

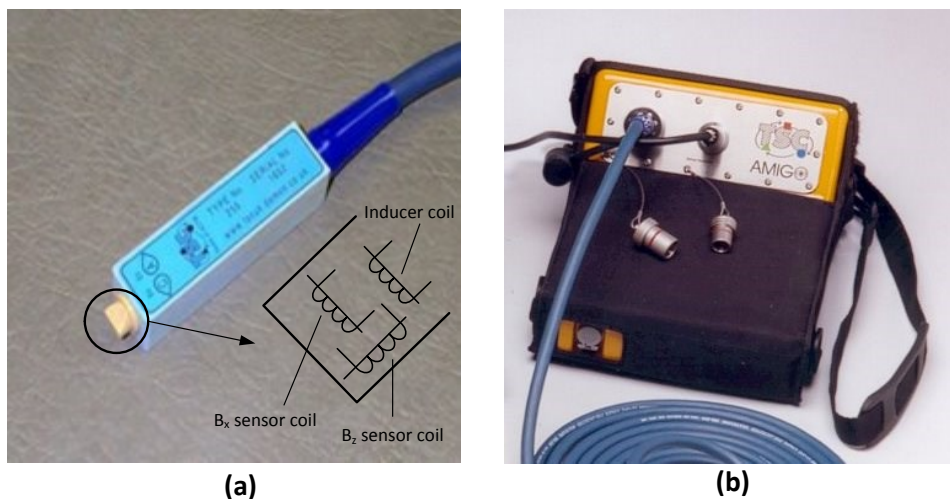


Figure 3.8 (a) The ACFM 5 kHz micro pencil probe and (b) the ACFM AMIGO instrument [99].

Table 3.3 The representation of ACFM sensor data format.

Data	Number of bytes
> Character	1
Checksum	1
B_x	2
B_z	2
Carriage return character	1

3.3.3. Laser Sensor Agent

Laser sensors have been widely employed in unknown environments for various purposes such as object recognition, obstacle detection and localisation, pose estimation and surface pattern extraction [100-105]. In this research, the *ILD 1302-20* laser triangulation displacement sensor supplied by Micro-Epsilon® has been used. It helps to accurately measure the rail head profile (Figure 3.9). It also assists the robot arm to calibrate its orientation with respect to the rail; this eliminates any uncertainties about the correct alignment of the robot (and hence the ACFM probe) when a characterisation scan is to be performed. Further, it ensures the desired ACFM probe lift-off and orientation are achieved, which plays a crucial factor in the reliability of the ACFM data in the absence of an expert human operator.

The laser sensor is interfaced to a PC via a serial port (a library file is provided) and transmits the moving averaged data (10 µm resolutions) at 115200 bps sampled at 750 Hz. In order to correctly measure a distance, objects (in this case the surface of rail) must be placed in the range of 30-50 mm from the measuring lens otherwise the sensor outputs a negative value. The distance is measured by issuing a polling instruction to the sensor which stores the measurement in a double precision floating point number in the range 0-20 mm which must be added to 30 to provide the actual distance from the object. It should be noted that the

resultant accuracy of the profile measurement is decreased to 0.1 mm (accuracy of the robot) when the laser sensor is integrated with the robot arm's end effector. A dedicated thread is used in the UI for reading the data from the laser sensor.



Figure 3.9 Image of the Micro-Epsilon ILD 1302-20 laser triangulation displacement sensor [106].

3.3.4. Motion Controller Agent

Using a PIC18F4431, a programmable interface controller (PIC) based closed loop control sequence has been developed to control the trolley's speed and position (Figure 3.10). The developed firmware and hardware regulates the speed of the variable frequency drive (VFD) through an analogue input to propel the motorised trolley. It also provides the IUI with information on instantaneous position and speed of the trolley. Figure 3.11 shows the block diagram representation of the motion controller agent.



Figure 3.10 Illustration of the motion controller agent and its components. Labels: 1→ Developed position/speed controller, 2→ position feedback signal from odometer, 3→ RS232 serial I/O port, 4→ Analogue output, 5→ emergency stop signal, 6→ ABB VFD inverter, 7→ three-phase AC motor used to propel the trolley.

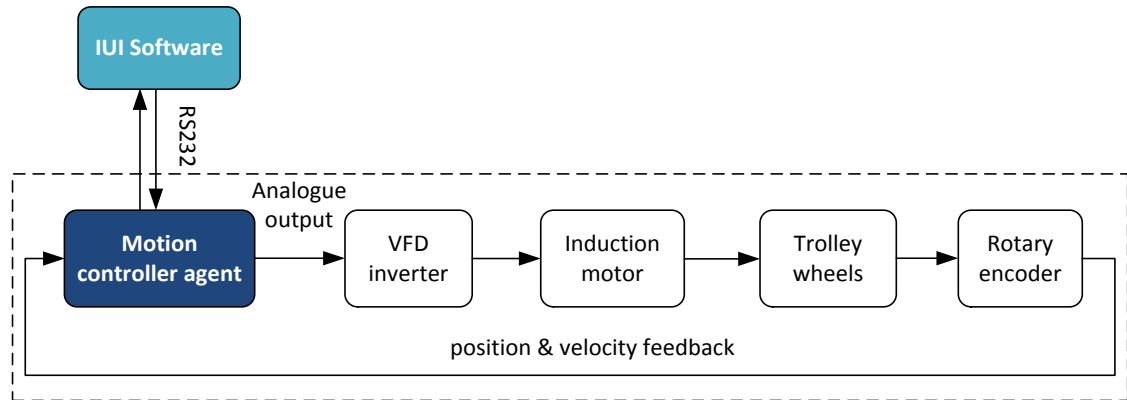


Figure 3.11 Block diagram of the closed loop motion controller agent.

3.3.4.1. Motion Feedback

Rotary encoders have been widely employed at both research and industry level to provide cheap and accurate position/velocity measurement at millimetre-level accuracy [100-103, 107]. However, the likely wheel-slip (due to a reduced adhesion force at the measuring wheel contact surface) may result in significant position/velocity error which reduces their reliability. A number of solutions have been proposed in the literature to tackle this problem. In this research, the problem of wheel-slip has been avoided by attaching the sensor to a separate measurement wheel spring loaded to avoid wheel slippage. The amount of spring pre-load has been calculated based on a maximum expected acceleration/ deceleration and a worst case scenario where adhesion force (static friction coefficient) at the wheel-rail contact are reduced to its minimum.

A *Miniature Type 2400* encoder supplied by Kubler Group has been used which generates 12 bits resolution pulses representing the incremental rotation of the measuring wheel. The encoder produces three logical signals in the form of quadrature that are QA, QB and INDEX. The incremental position of the rotating shaft connected to the measuring wheel may be

obtained by counting the number of pulses generated by QA or QB. The absolute position may also be obtained by counting the INDEX pulses representing the number of revolutions. Further, there is a 90° phase offset between the QA and QB signals. This information is exploited to give the direction of rotation; if the former lead the latter then the direction of travel is forward otherwise is backwards (Figure 3.12).

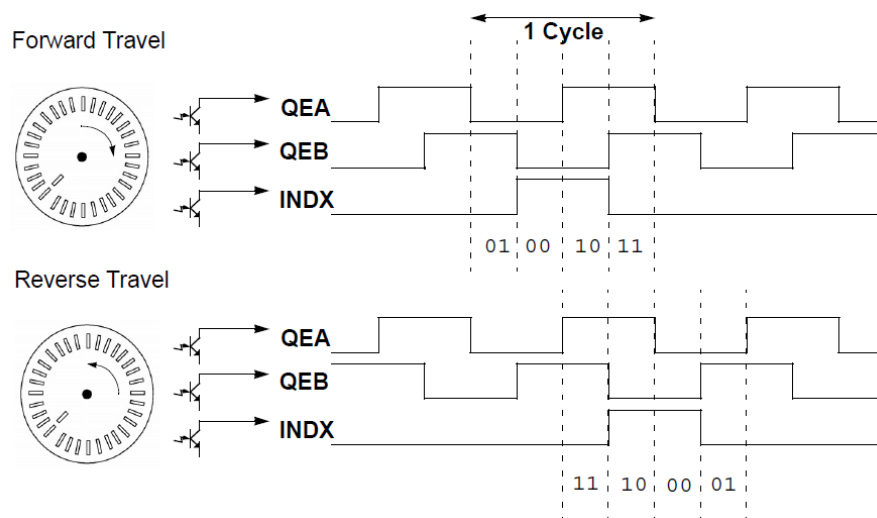


Figure 3.12 Quadrature encoder interface signals [108].

The microcontroller used supports a quadrature encoder interface (QEI) hardware module which has been used to decode these three signals to provide real-time information on position and velocity of the trolley. The QEI module enjoys a 16 bits time-base register which can be configured to be incremented on every rising edge of the QA signal. The counter is reset when its value reaches the maximum number of pulses per revolution specified by the user (1024 in this case) and is stored in another 16 bits register. The QEI module also features a number of hardware interrupt-driven registers which are used in the firmware to provide information about the absolute position of the rotating shaft. The QEI registers are described in Table 3.4. This information has been put together in the firmware to calculate the instantaneous position and speed of the trolley and transmit it to the IUI.

Table 3.4 Summary of the hardware registers used in the QEI module for PIC18F4431.

Register name	Size (bits)	Function
MAXCNT	16	Storing the maximum number of pulses per revolution specified by the user upon initialization of the IUI
POSCNT	16	Storing the accumulated pulses generated by QA. It resets to zero once the maximum number of pulses is reached
QEICON (UP/ $\overline{\text{DOWN}}$)	1	A bi-state register indicating the direction of rotation, 1 for forward and 0 for reverse
PIR3 (IC2QEIF)	1	The register flag is set at every INDEX pulse and must be cleared in the firmware

3.3.4.2. Position Controller

A proportional (P) controller has been found to be appropriate for this application due to its relatively rapid response time, simplicity and easy implementation. The controller output is linearly proportional to position error (e) which is defined as difference between target position (x_t) and the current position (x_c) measured using the rotary encoder as given by Equation (3.8). The P controller has been tuned online using the Ziegler-Nichols method [109]. For a specific location on the rail track where a characterisation scan is required, the IUI moves the trolley to the desired location. In the process, the set point signal (target position) is transmitted to the controller which continues regulating the speed of the trolley until the steady state position error (SSPE) < 30 mm. Meanwhile, the IUI goes into an idle state until it is informed that the position convergence criterion has been met. The SSPE may then be compensated for by the robot arm (a SSPE beyond 50 mm will not be tolerated by the system as some scan points may fall outside the work space of the robot). Figure 3.13 shows the control strategies implemented in the microcontroller.

$$\begin{cases} e = x_t - x_c \\ V = K_p e \end{cases} \quad (3.8)$$

where K_p is the proportional constant (experimentally tuned) and V is the corresponding control voltage output from the controller.

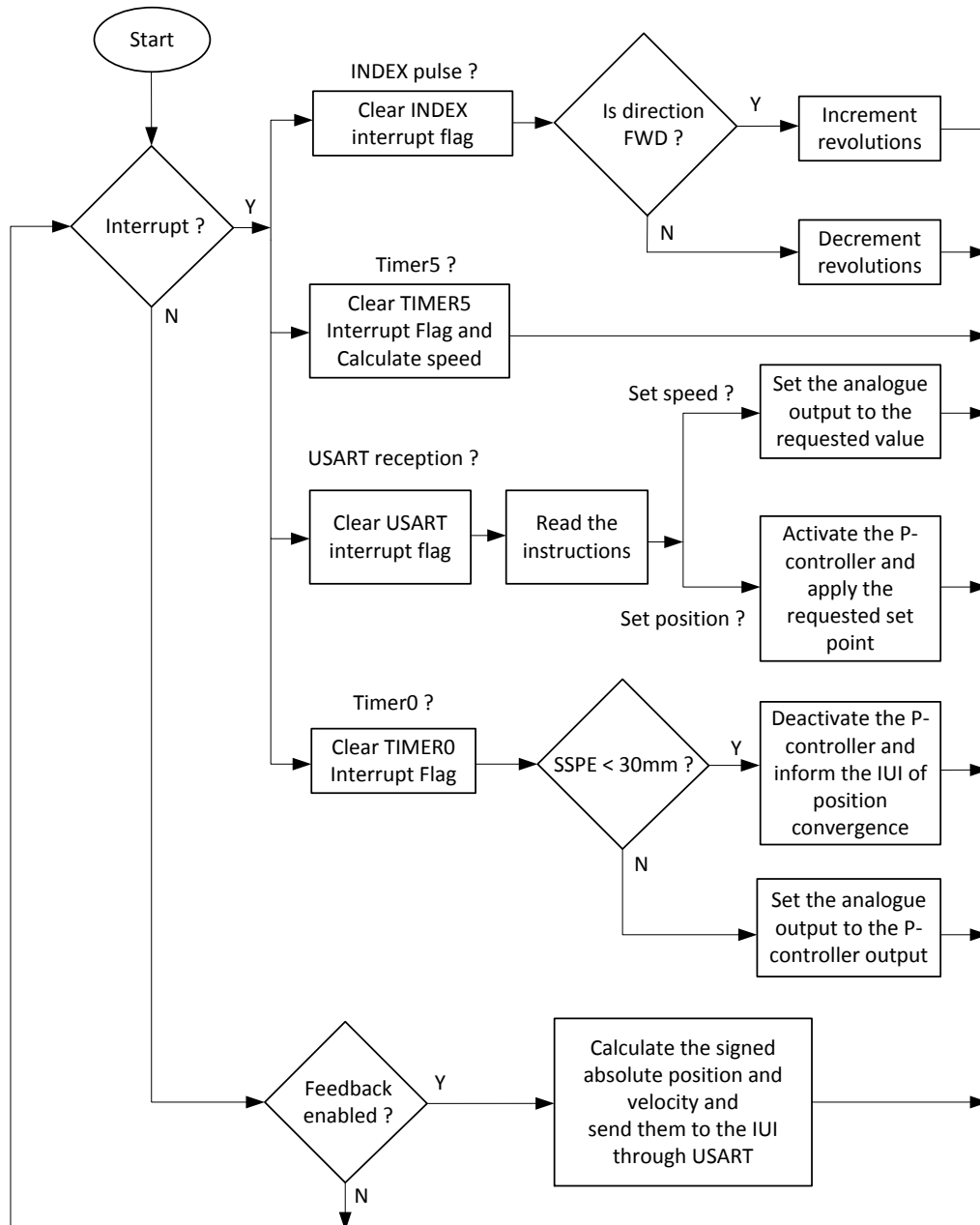


Figure 3.13 Flow chart demonstration of the control sequences implemented on the microcontroller running at 20 MHz (using external clock).

3.4. Functionalities of the Developed Robotic System

The functionalities of the software agents used in the IUI are discussed here. These include robot arm calibration, rail profile measurement, 3D ACFM scan, crack surface angle detection and 1D ACFM scan for sizing the defect. These functions are used in both manual and automatic modes. In the manual mode, for a 3D ACFM scan, they should be called in sequence; firstly the robot arm is calibrated to avoid any misalignment (the users may skip this step if not needed but is always performed in automatic mode), then the rail profile is measured with the robot arm and lastly the 3D ACFM scan over the measured profile may be initiated.

3.4.1. Calibration

The robot arm should be calibrated to alleviate the adverse effect of the robotic system's lateral movement introduced during travel of the trolley to the defect location. This helps increase the reliability of the rail profile measurement and also the automatic ACFM scans in the process of automatic defect characterisation. The calibration is required for both the O and A angles which are initially set at 0° and 90° , respectively.

3.4.1.1. Orientation Angle

Initially, the robot arm is instructed to move from its current location point P_1 , to point P_2 as shown in Figure 3.14. Then, using the laser sensor and robot arm, a two-point based calibration is carried out. These two points (P_2 and P_3) are apart by distance d along the tool direction (\vec{u}_z). In the first measurement the laser sensor records the current height h_0 at the

point P_2 . The second measurement (h_1) is then taken after the robot arm has moved to the point P_3 . The orientation angle offset ΔO may be calculated as:

$$\Delta O = \tan^{-1}\left(\frac{h_0 - h_1}{d}\right) \quad (3.9)$$

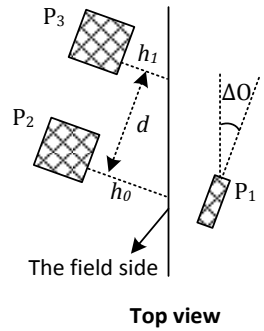


Figure 3.14 Two-point based calibration approach for the orientation angle. The robot’s tool angle for points P_2 and P_3 has been set to -90° to make the laser sensor face the field side of the rail.

3.4.1.2. Attitude Angle

Subsequently, the robot arm moves to its initial location (P_1) at the corrected orientation angle (ΔO) defined by Equation (3.9). Then the A angle is calibrated similarly using the previous approach; the current height is first measured as h_2 at the point P_1 , then the robot arm moves to the point P_4 followed by the new measurement of height h_3 at this point (Figure 3.15). The attitude angle offset is therefore calculated as:

$$\Delta A = \tan^{-1}\left(\frac{h_3 - h_2}{d}\right) \quad (3.10)$$

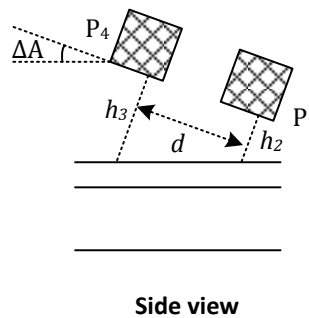


Figure 3.15 Two-point based calibration approach for the attitude angle.

A specific program has been developed to facilitate the robot’s movement to the points at which the laser measurement is taken. The program is stored in the robot’s memory and contains a number of instructions written in AS language. It may be called through the IUI software by sending an appropriate command. The robot first moves to the desired location and informs the IUI of its arrival by sending a specific message and goes into an idle state until notified to proceed to the next point. At the same time, the IUI takes a laser measurement of the current height, once the message is received. It then informs the robot to move on to the next point. The process is repeated until all the necessary measurements are taken. The algorithm is described in Figure 3.16.

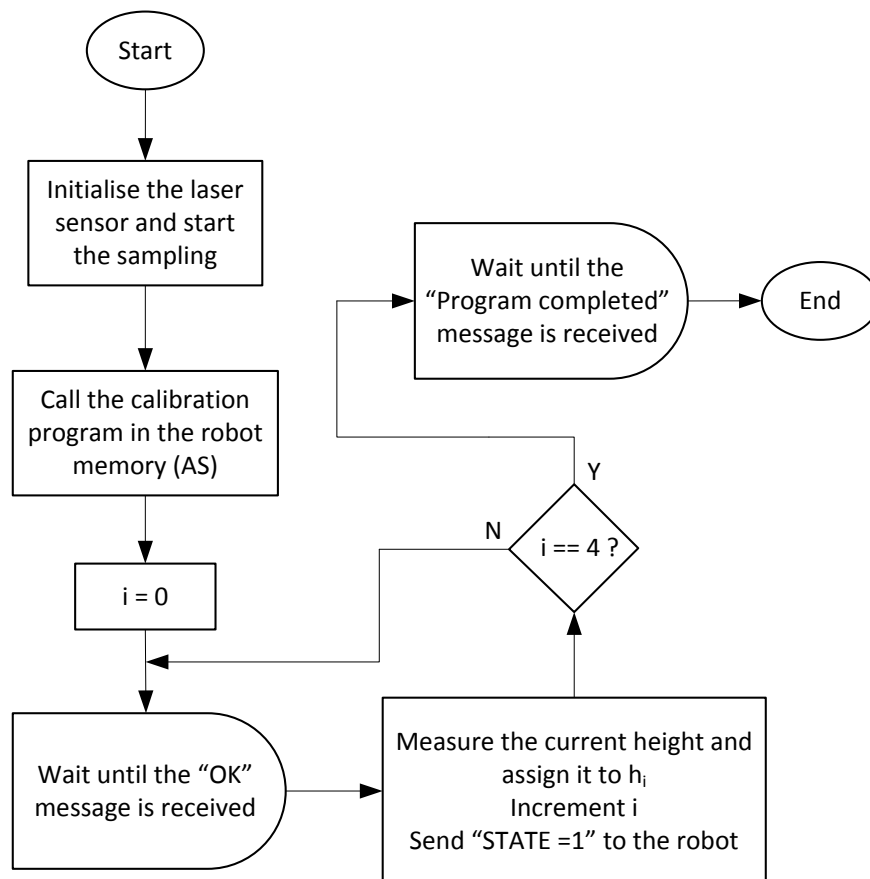


Figure 3.16 Process flow chart representation of the “Calibrate” function in the IUI.

3.4.2. Profile Measurement

It is known that in order to accurately characterise the detected defects the ACFM probe lift-off should remain constant and also that the ACFM probe should be normal to the surface of the specimen under inspection. The fact that RCF cracks often appear on the gauge corner of the rail, where the curvature changes significantly, makes it essential to measure the rail head profile to take into account the lift-off variation caused by any geometry change. A local measurement of the profile is required, rather than using a standard 'new' rail profile, as the repeated wheel-rail contact in service results in wear and changes to the rail profile (Figure 3.17).

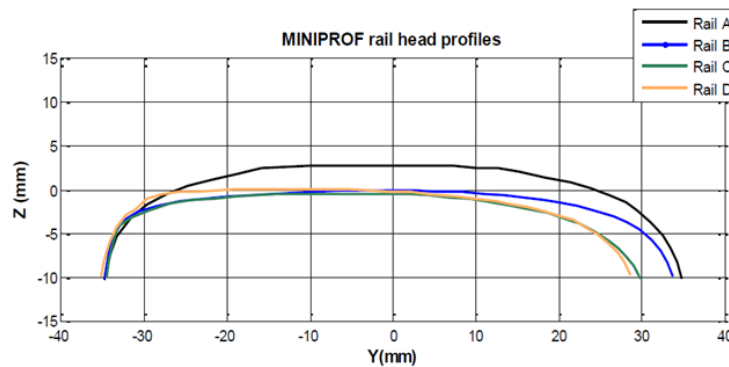


Figure 3.17 Rail head profile of in-service rails (BS113A) subject to different amount of wear. Rail A represents a new rail.

The “MeasureProfile” function has been developed to receive and process the real-time data from both the robot and laser sensor. The function calls an AS program in the robot controller which when executed, moves the laser sensor from left to right in the Y direction and sends the instantaneous horizontal coordinates (Y) back to the IUI software. Meanwhile, the IUI waits for incoming data from the robot and measures the distance from the rail surface once the data has arrived. The data from the robot and laser sensor are then combined to form a 2D rail head profile. These steps are outlined in Figure 3.18.

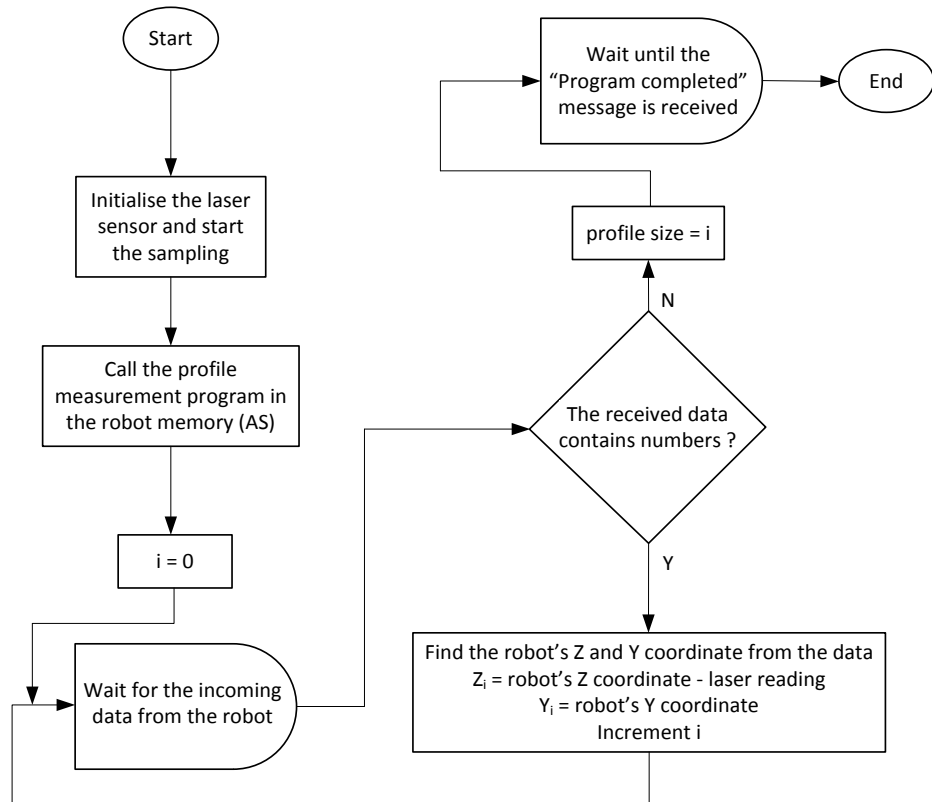


Figure 3.18 Process flow chart representation of the “MeasureProfile” function in the IUI.

It has been demonstrated that the accuracy of the laser profile measurement with the robot arm is comparable to that obtained using MiniProf, the commercial equipment for this purpose (Figure 3.19).

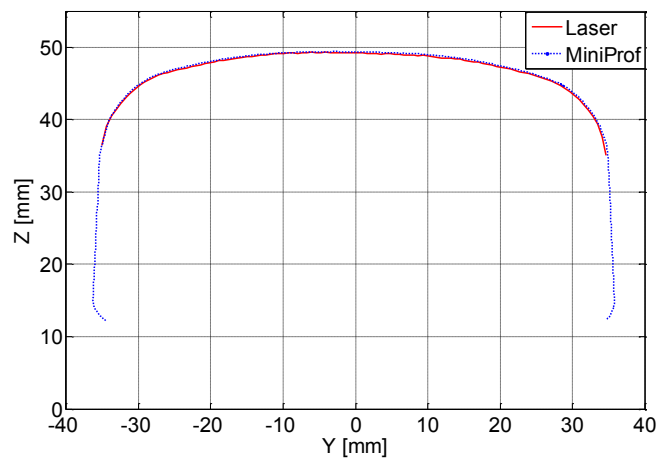


Figure 3.19 Comparison between the robot and MiniProf measurement on UIC54 rail.

3.4.2.1. High Order Polynomial Fitting

The rail profile is smoothed by fitting a high order polynomial defined by Equation (3.11) to the measured profile (Figure 3.20) which reduces the inaccuracies introduced due to surface noise (owing to surface roughness) and quantisation error, which have the potential to affect the alignment of the ACFM probe. The unknown coefficients of the fitted polynomial p_j ($j = 0 \dots k$) are optimised using the Levenberg-Marquardt approach (a library file was provided) on the basis of minimising the quadratic cost function J expressed in Equation (3.12):

$$z^*_i = \sum_{j=0}^k p_j y_i^j \quad (3.11)$$

$$J = \sum_{i=1}^n (z_i - z^*_i)^2 \quad (3.12)$$

where k is the order of the polynomial to be fitted, n is the number of points on the rail profile and z_i and z^*_i are the measured value and the fitted value, respectively. There is no fixed rule for finding the optimum value of k , however, it may be experimentally found by plotting a standard deviation (SD) of residuals against polynomial order. An example is shown in Figure 3.21. It can be observed that the reduction in the SD of residuals for polynomial of orders beyond 16 is insignificant, thus a 16th order polynomial has been found to be appropriate in this study. The tangent angle (i.e. the angle made between normal to the rail surface at a given point and the Z axis, as shown in Figure 3.7a) denoted by t_i ($i = 1 \dots n$) is given by:

$$t_i = \tan^{-1} \left(\frac{dz^*_i}{dy} \right) = \tan^{-1} \left(\sum_{j=1}^k j p_j y_i^{j-1} \right) \quad (3.13)$$

In Equation (3.13) the derivative term is determined based on the fitted curve using an analytical approach rather than the numerical differentiation. This technique has the advantage of suppressing the measurement error and results in a smoother trajectory for the ACFM probe (Figure 3.22).

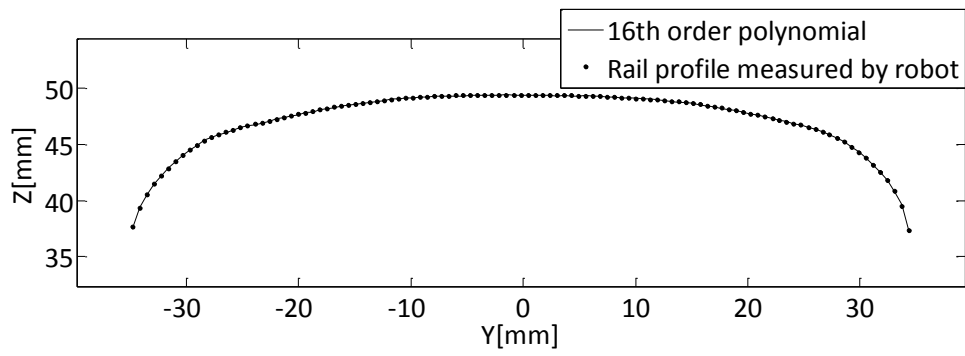


Figure 3.20 Demonstration of a 16th degree polynomial fitted to the measured rail profile.

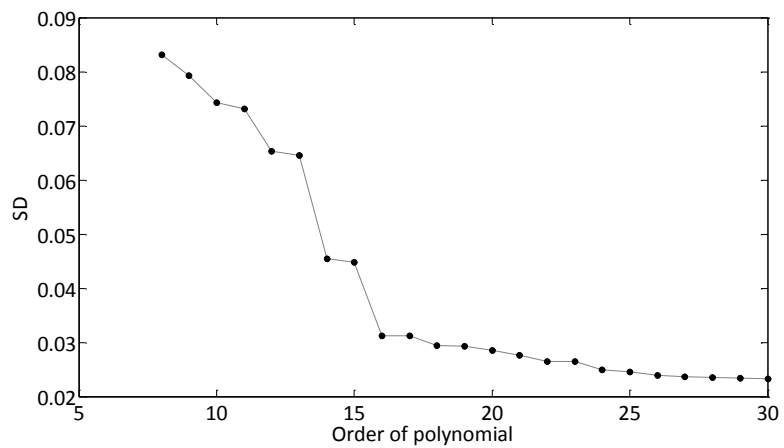


Figure 3.21 Plot of standard deviation of residuals against order of polynomial.

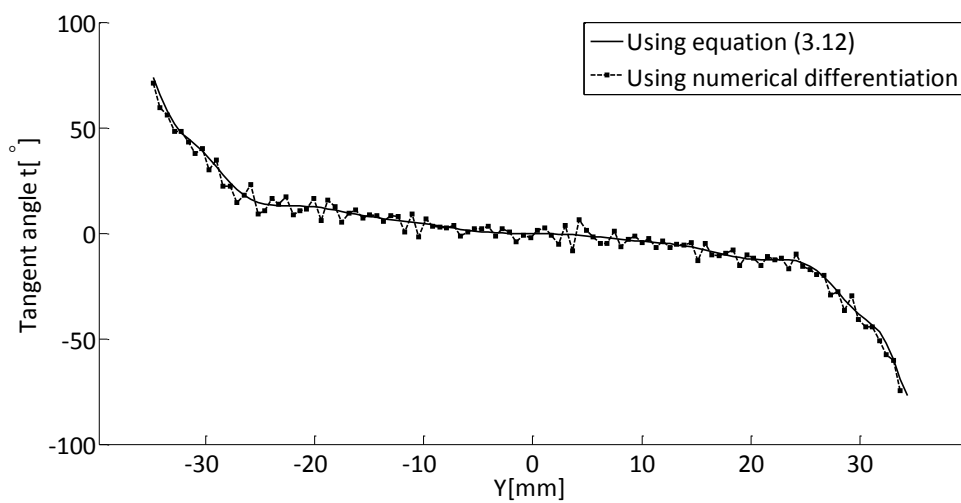


Figure 3.22 Comparison between the numerical and analytical approach for calculating the ACFM probe's tangent angle t .

3.4.3. RCF Crack Characterisation

3.4.3.1. 3D ACFM Grid Scan

Following the calibration of the robot arm and rail profile measurement, a 3D scan may be initiated. The scan is performed at constant ACFM probe lift-off and speed (defined by the user) while the ACFM probe follows the rail head profile. This condition is crucial in determining the orientation of an unknown crack and hence the accuracy and reliability of the crack sizing process. A scan region with uniform spacing in the Y direction (Figure 3.23) is specified by the user through lower and upper limits on the rail head profile, although in automatic mode a default range is used. To accomplish this, the IUI first transforms the smoothed rail profile data using Equations (3.4) to (3.6) and then successively transfers them to the robot's memory (using the TCP/IP protocol). Subsequently, the IUI calls an AS program (stored in the robot's controller memory) developed for the ACFM 3D scan and records the ACFM signal at regular intervals (every 15 ms) once an appropriate signal is received from the robot. The process starts at the beginning of each longitudinal path on the measurement grid and terminates once the path has been swept (Figure 3.23). Consequently the ACFM probe advances to the next point on the rail profile and the procedure is repeated until the region is completely scanned. These sequences are depicted in Figure 3.24.

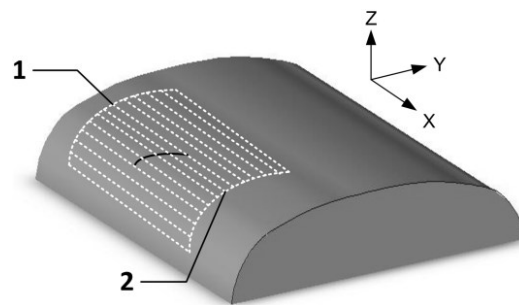
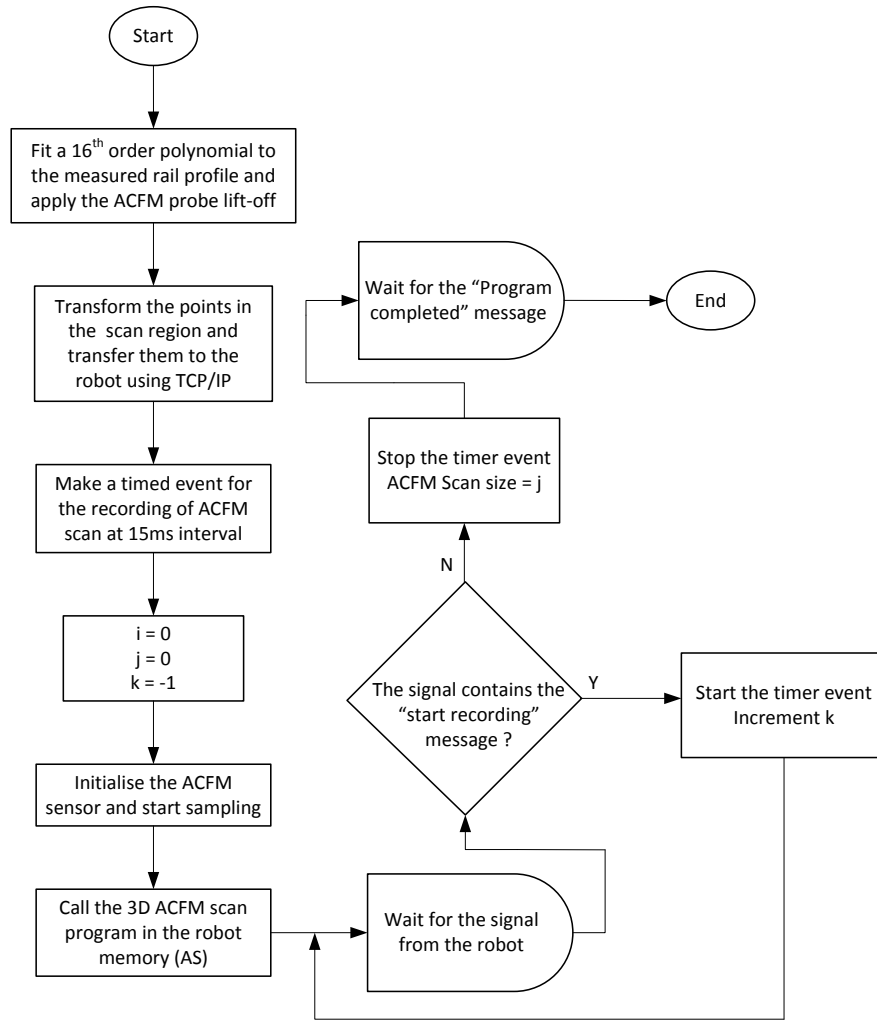


Figure 3.23 Illustration of the scan region on the rail profile. Labels: 1→ start of recording, 2→ end of recording.



Timer event (fired on a separate thread)

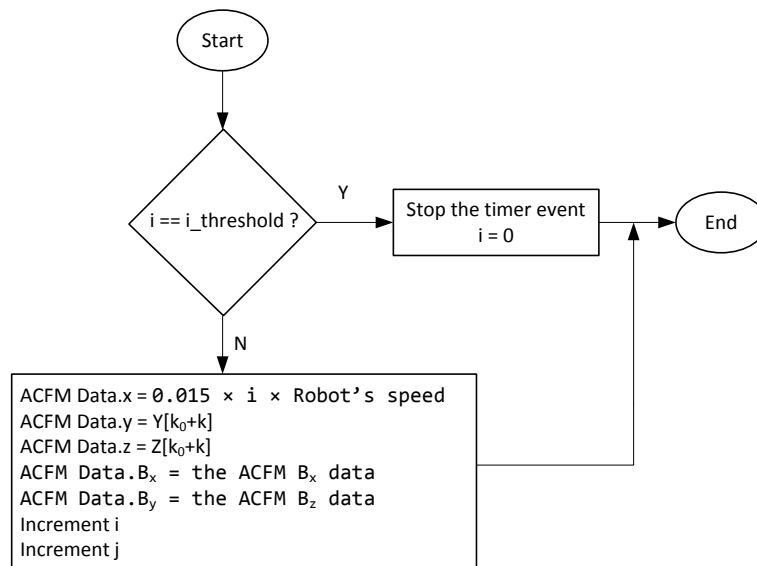


Figure 3.24 The process flow diagram of the "RScan" function in the IUI.

3.4.3.2. Crack Surface Angle Detection

An angle offset between the ACFM sensor and crack results in an underestimation of the RCF crack's pocket length since the change of probe angle causes a reduction in the ACFM maximum signal reduction (ΔB_x) which is inverted to give the pocket length. This has been confirmed by a finite element method simulation study of the ACFM signal over a semi-elliptical crack by Nicholson, et al. [65] as demonstrated in Figure 3.25. The characteristic peaks in the B_x signal near the crack ends (due to an increase in the eddy current density) may be exploited to locate the crack ends and hence the crack surface angle by performing a 3D scan (2D for flat surfaces) over the region encompassing the crack. It will be shown in the next chapter that in practice, the crack surface angle may be detected within an error of 5° where the variation of the B_x signal to the angle offset between the probe and the crack is a minimum.

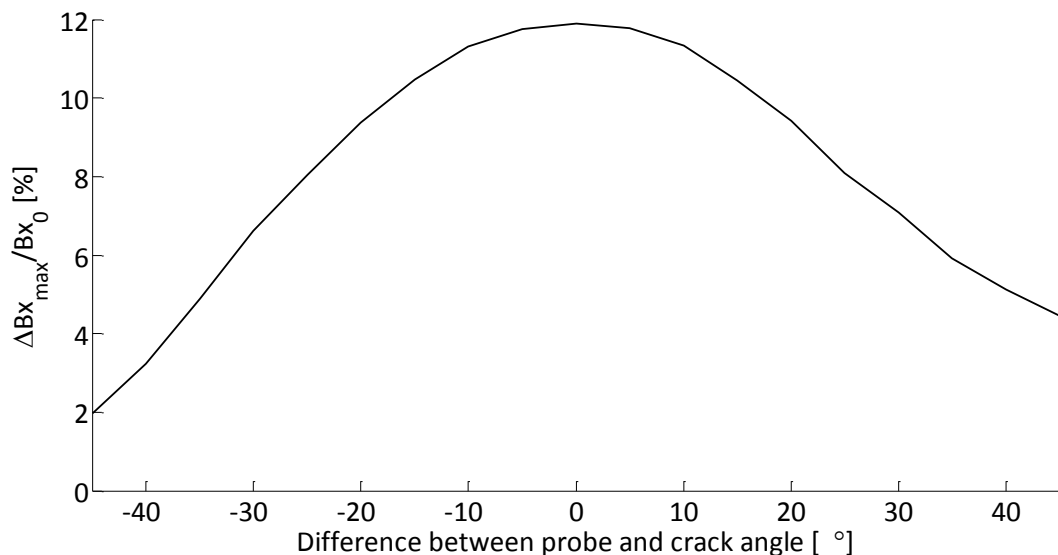


Figure 3.25 The sensitivity of the maximum change in B_x value at zero lift-off to changes in the orientation of the ACFM probe relative to surface crack angle for a 15 mm surface length, 5 mm pocket length semi ellipse [65].

3.4.3.3. Searching Algorithm

A fast searching algorithm has been developed that takes the 3D ACFM scans as an input and returns the crack surface angle as its output. The algorithm first finds the location of the minimum B_x signal within the scan region corresponding to the maximum depth of the crack and then the scan region is narrowed down by two searching windows based on a maximum possible crack length (25 mm in this case). These are the north-west and south-east regions (from the middle of the crack) where the crack ends are surrounded as shown in Figure 3.26. Then, the crack ends are found by searching the location of the maximum B_x signal within these windows. This method is beneficial as it eliminates the need for searching the entire scan region once the location of the maximum defect depth is identified. Alternatively, the crack ends may be found by searching the location of highest peak and lowest trough in the B_z signal where the rotation of eddy current takes place, nonetheless, it has been experimentally observed that this approach works reasonably well only for small angle offset and results in unacceptable error as the angle offset is increased. The accuracy of both approaches is discussed in detail in chapter 4 (4.3.2).

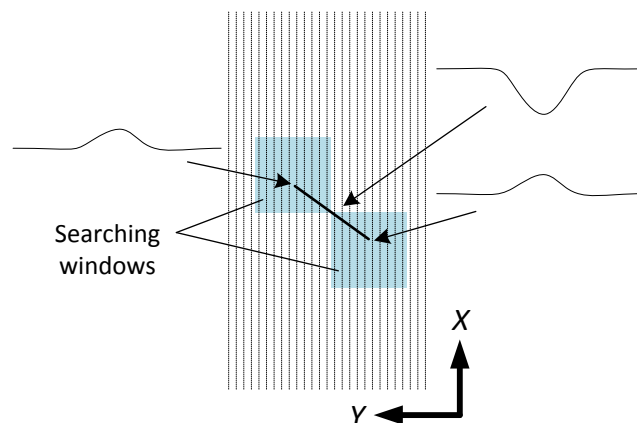


Figure 3.26 Demonstration of the searching algorithm and the B_x waveforms developed in the middle and near the ends of the crack. The location of maximum B_x signal indicates the crack ends in each of the searching windows.

3.4.3.4. 1D ACFM Scan

The knowledge of a crack's surface length is vital in the determination of the crack's pocket length from the B_x signal. The surface length can be closely approximated by the distance between the characteristic peak and trough in the B_z signal [52] provided the measurements are taken along the crack opening at the correct probe angle.

After the crack surface angle is detected through the searching algorithm discussed earlier, the IUI instructs the robot arm to move the ACFM probe in the corrected direction (Figure 3.27) while the ACFM probe is maintained normal to the rail surface at the constant probe lift-off. In the meantime the ACFM measurements (B_x and B_z) and the distance data are recorded in the IUI for accurate crack sizing.

In the process, the ACFM probe's path (discretized points) is constructed in the IUI software and transmitted to the robot's memory. Then an AS program developed for moving the ACFM probe along the crack opening and sending back the probe's current position is called. The ACFM measurements are recorded when an appropriate signal is acknowledged from the robot. Figure 3.28 schematises the ACFM sizing process in the IUI.

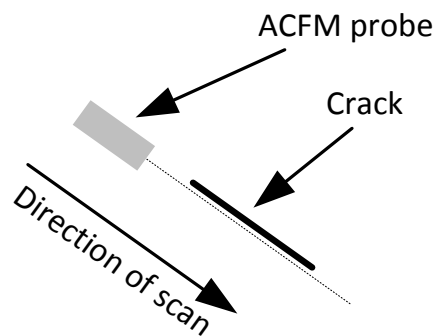


Figure 3.27 Illustration of 1D ACFM scan for crack sizing.

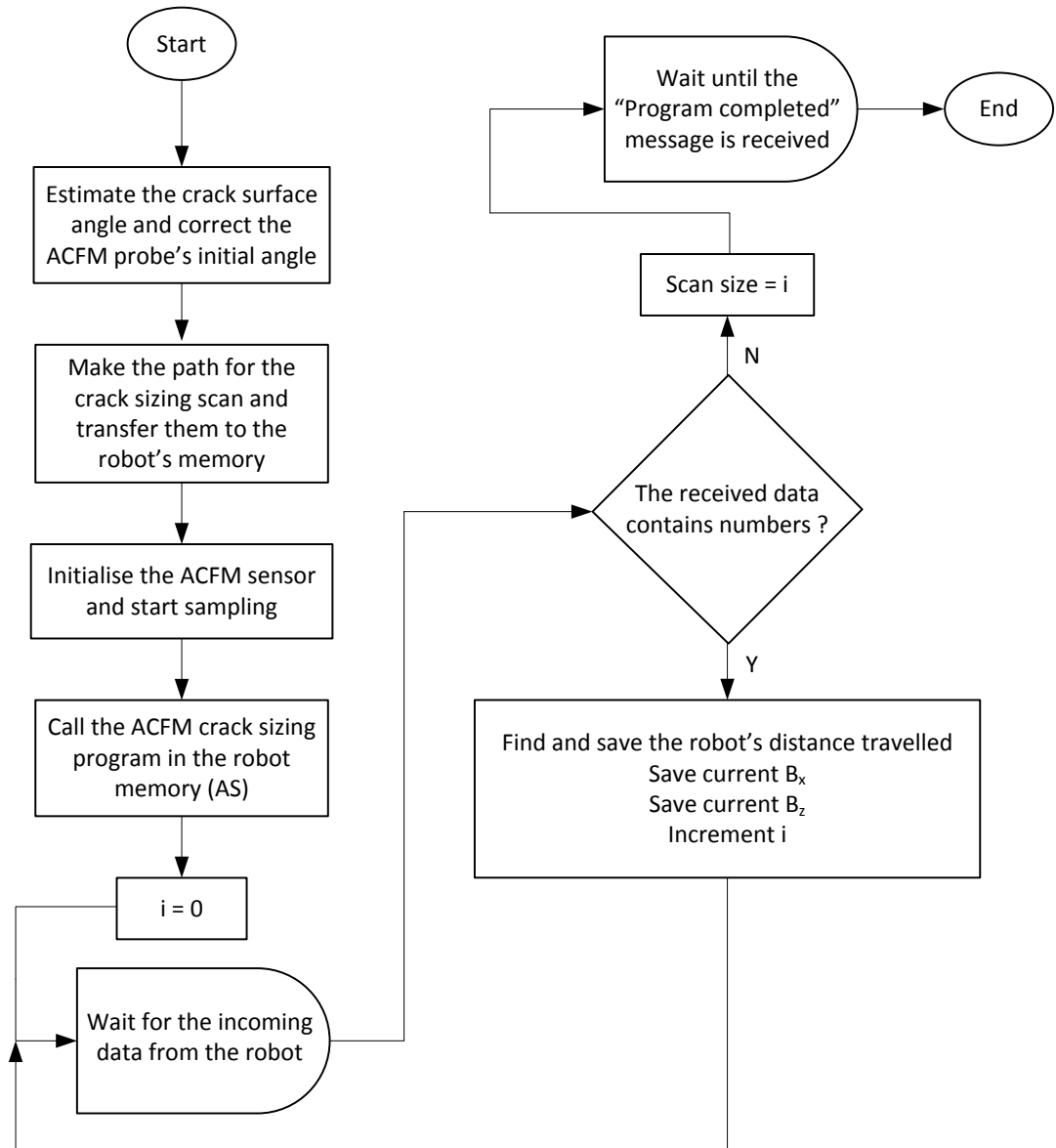


Figure 3.28 The process flow representation for the 1D ACFM scan for crack sizing.

3.4.4. RCF Crack Detection

When operating in the detection mode, the robotic system travels at a moderate speed (4-20 km/h, set by the operator) whilst the robot arm holds the ACFM sensor in a fixed position at a pre-determined angle with respect to the running direction of the rail (e.g. this is typically set at an average angle of 52° based on reported range of RCF crack

orientation [3, 8-10]) in order to maximise the likelihood of detecting RCF defects present in the rail.

Any difference in the ACFM probe sensor angle and the crack's surface breaking component with respect to the rail running direction will result in a reduction in the magnitude of the ACFM signal change (i.e. deviation from the background signal). However, the resultant crack signal should still be detected for probe offset angles of $\pm 20^\circ$ since the change in signal (with respect to the background) is predicted to be approximately 2.5% for a 5 mm pocket length crack at $\pm 20^\circ$ offset [3], as discussed in Chapter 3 (section 3.4.3.2). The majority of RCF type cracks are reported to have an angle between 30° and 75° to the rail running direction [3, 8-10].

After the settings for the crack detection operation have been applied by the user (e.g. trolley speed, inspection distance and ACFM probe orientation), the IUI instructs the motion controller module to move the trolley over the inspection distance at a controlled speed whilst the ACFM sensor signal along with the position signal are sampled and stored in the software memory. Using 2GB of RAM, the software can store the inspection data for up to 31 km of track running at an average speed of 5 km/h. A flow diagram for the detection scan is given in Figure 3.29.

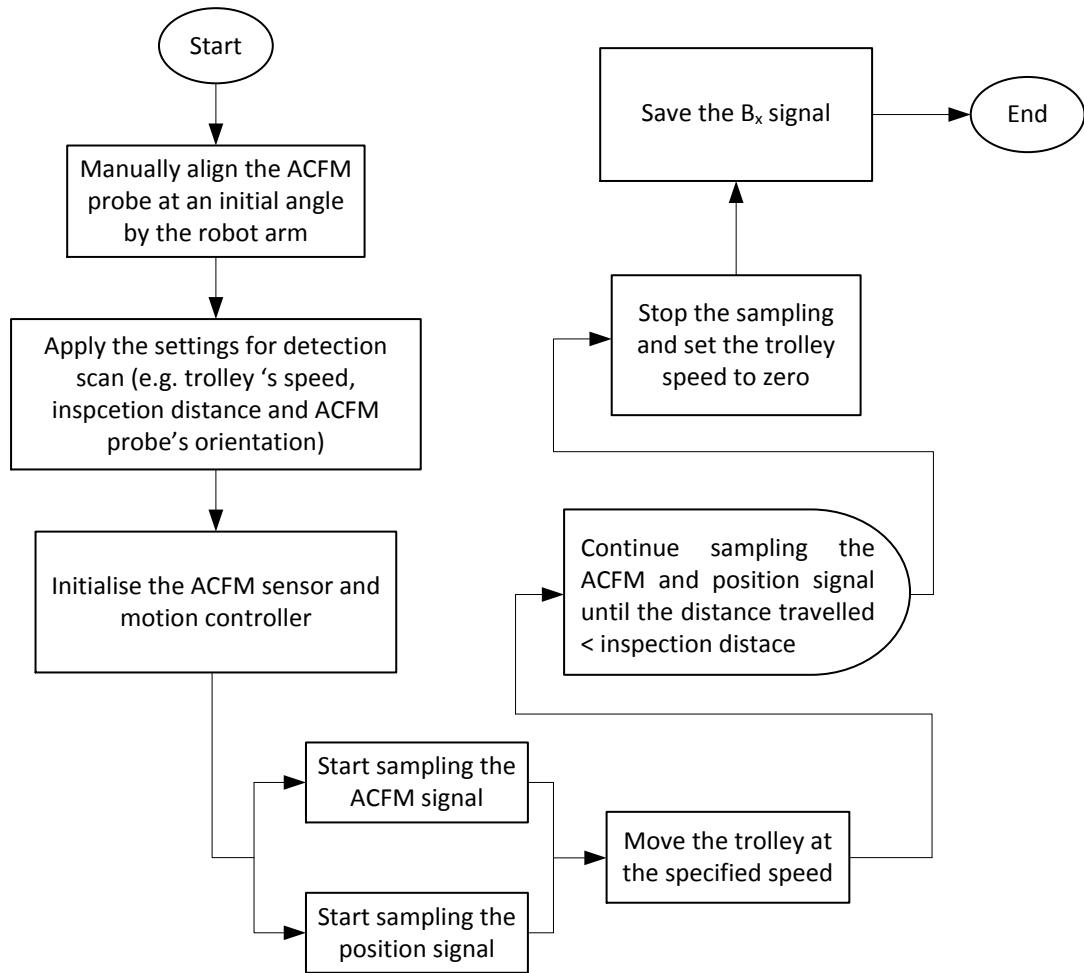


Figure 3.29 The process flow representation for an automatic detection scan.

3.5. Summary

In this chapter, the process of design and development of a robotic trolley for automatic detection and characterisation of RCF cracks in rails using the ACFM technique has been systematically presented. The robotic trolley is autonomously controlled by the developed IUI software using AI based on a conventional RBES architecture. It can automatically deploy the robot arm to perform constant lift-off 3D ACFM grid scans conforming to the rail profile at a speed of 1-20 mm/s over unknown RCF cracks to obtain critical data needed for accurate sizing (e.g. crack surface angle, length). Using even grid spacing of 0.5 mm, a 3D

ACFM scan over a single defect takes approximately 240 s. This is followed by an automatic non-contact rail profile measurement at a repeatability error of 0.1 mm prior to the ACFM scan. These are demonstrated in Chapter 4.

The robotic system can also inspect the rail track at a constant speed of 4-20 km/h to locate the RCF defects (automatic detection scans). Besides, it can automatically travel to the location of the detected defects with a position error of 30 mm and automatically use the robot arm to collect reliable and detailed data to characterise them (automatic characterisation scans). These are demonstrated in Chapter 5.

Chapter 4. Case Study: Static Results

4.1. Introduction






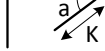


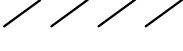
This chapter discusses the first of the three case studies designed to demonstrate the results of several static experiments that have been carried out on rail samples containing artificial RCF cracks. The experiments mimic the real scenario of automatic crack characterisation where the position of the crack along the rails is identified using an initial detection scan run, as discussed in Chapter 3 (section 3.4.4) and later in Chapter 5 (section 5.4.1) while the inspection trolley is deployed to automatically survey the defective area to collect more detailed information, enabling accurate sizing of the cracks found. For each test, the robot first measures the rail profile near the defect and then performs a constant lift-off 3D ACFM scan over a user-specified region of the rail containing the crack. Several important factors, such as ACFM sensor lift-off, SNR, ACFM probe orientation and grid spacing have been investigated. Further, the performance of the searching algorithm for determination of an unknown RCF crack angle (i.e. the angle the surface breaking part of the crack makes with the rail direction) has been studied and compared with the simulation results.

4.2. Experimental Setup

A UIC54 rail containing eight artificially-induced semi-elliptical cracks typical of light RCF cracks in rails [64] has been used as a calibration block for assessment of the accuracy of the crack sizing procedure (see Table 4.1). For each defect, the robot first measures the rail head profile using the laser sensor, as described in section 3.4.2, and then performs a 3D ACFM

scan over the rail profile in the 3D grid region specified by the user. Investigation on samples taken from in-service rail show that the RCF cracks form just above the gauge corner of the rail [110]. Therefore, in automatic mode, a default range of 30% of the rail profile width is used to ensure the scan region aligns with the RCF crack region. Also, the accuracy of the searching algorithm has been assessed based on B_x and B_z signals for cases of both matching and non-matching probe angle. Further, the experimental measurements (B_x and B_z) have been compared against predicted values based on COMSOL simulations of the ACFM signals for the same cracks used in the calibration block with the assumption of a flat rail surface [111].

Table 4.1 Schematic diagram and details of the calibration block.

Top view								
(1)	(2)	(3)	(4)	(5-8)				
								
Side view								
								
Crack Number	1	2	3	4	5	6	7	8
Surface angle (b) [°]	48	45	37	34	32	32	32	32
Surface length (L) [mm]	5	7	5	9	10	10	10	10
Pocket length (K) [mm]	2	2	2	3	4	4	4	4
Vertical angle (a) [°]	90	30	20	25	25	25	25	25

4.3. Results

4.3.1. Matching Probe Angle

It is known that the ACFM probe's initial angle α (Figure 3.7b), and hence angle made between the probe and the crack surface breaking length, affects the sensitivity of the signal to crack pocket length [64] and hence SNR in the case of experimental data given that the noise level remains constant. In this part of the study the probe angle was set to match the crack surface angle in order to obtain maximum field perturbations leading to optimisation of the SNR.

Furthermore, the probe was held normal to the surface of the rail to ensure a constant lift-off. The probe's lift-off was held at 2 mm while moving along the length of the rail at 10 mm/s. To acquire a reasonable level of background signal (B_x), unaffected by the crack, the scan lines were chosen to be 70 mm long (defect centrally positioned within the scan lines which were spaced apart by 0.5 mm). Figure 4.1 shows the contour plots of the ACFM scans over cracks 1-4. For each case, the magnetic flux distributions B_x and B_z have been normalised based on Equations (4.1) and (4.2) and plotted over the scan region, where x and z directions are clarified in Figure 4.2.

$$B_{x_n} = \frac{B_x}{B_{x_0}} \times 100 \quad (4.1)$$

$$B_{z_n} = \frac{B_z - B_{z_0}}{B_{z_{max}} - B_{z_0}} \times 100 \quad (4.2)$$

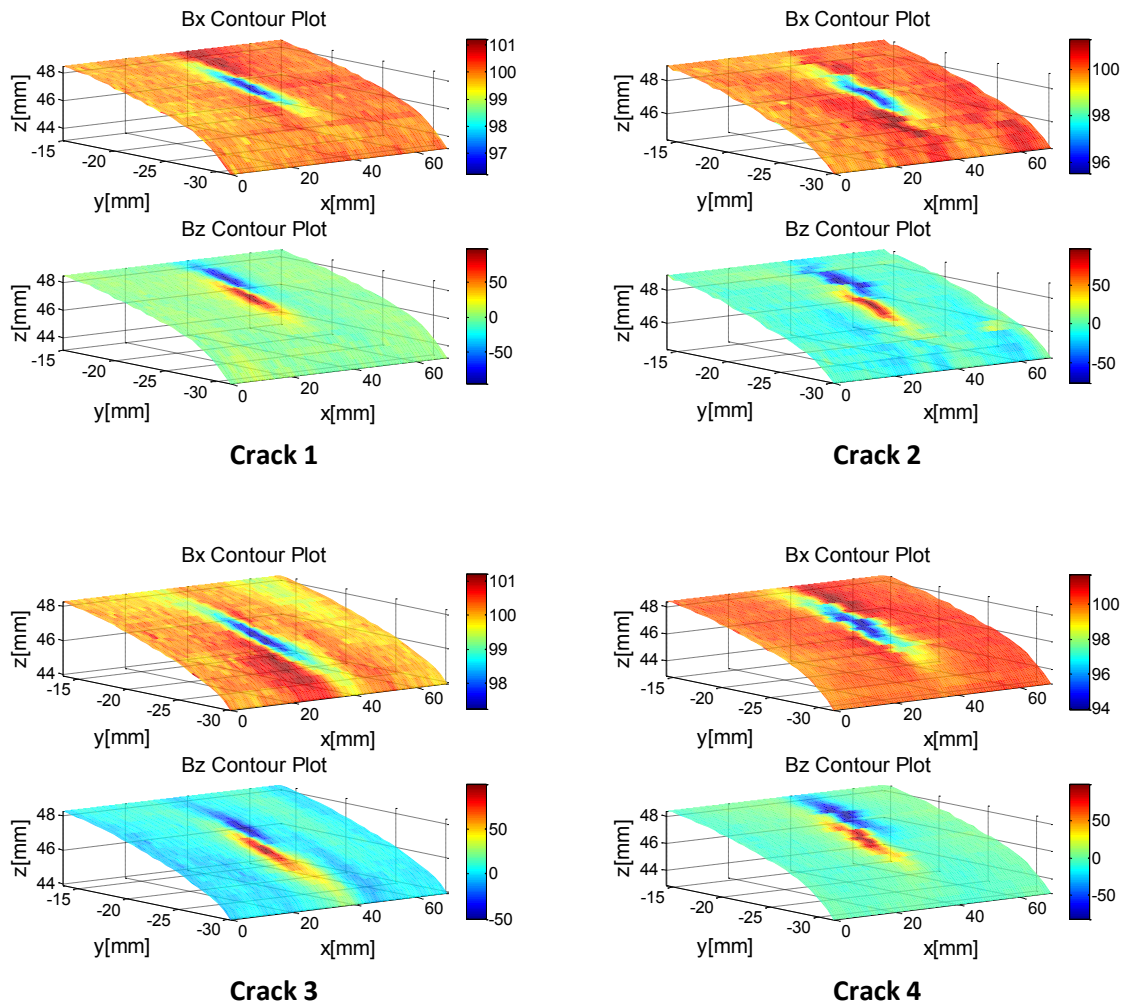


Figure 4.1 3D representations of the robotic ACFM scans over UIC54 calibration rail at 2 mm lift-off, matching probe angle, 0.5 mm spacing between scan lines and scan speed of 10 mm/s.

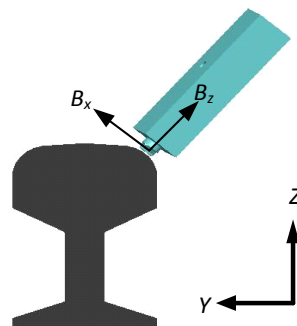


Figure 4.2 Direction of the magnetic flux components as measured by the ACFM sensor.

The B_x and B_z contour plots shown in Figure 4.1 for each crack have similar general characteristics due to the distribution of the magnetic field in the x and z directions, as described in section 2.3.8. For the B_x signal, the magnitude deviates from its background value (i.e. signal in the absence of a defect) as the current passes the defect and reaches its minimum (the lowest value on each contour map) at the deepest point of the crack. For the B_z plot, the highest and lowest values on each contour map correspond to the defect ends, where the induced current rotates to pass the crack.

It is known that the locations of the maximum and minimum B_z signals are associated with the crack ends (i.e. the crack surface length) [52] and this can be used to determine the angle of the defect to the rail length. The crack surface length may be roughly estimated simply by measuring the distance between the maximum and minimum B_z signal on the contour map (in practice, however, this calculation is based on a 1D ACFM measurement along the crack opening at a matching probe angle rather than grid scans). The crack ends are automatically found by the searching algorithm as described in section 3.4.3.3. It should be noted that the accuracy of the results are affected by noise as the searching algorithm works on the basis of maximum/minimum values. To reduce the adverse effect of noise, a simple first order low-pass filter defined by Equation (4.3) has been designed and applied to both B_x and B_z data.

$$G = \frac{Output}{Input} = \frac{1}{1 + (\pi f_s f_c)^{-1} jw} \quad (4.3)$$

$$f_c = \frac{2T_s * v}{d} \quad (4.4)$$

where G is the filter gain (also known as filter transfer function), f_s is the sampling frequency, f_c is the normalized cut-off frequency given by Equation (4.4), w is the frequency components of the signal to be filtered, j is a complex number defined as $\sqrt{-1}$, v is the speed of probe

movement along the scan lines (mm/s), T_s is the sampling time (s) and d is the signal drop region due to crack (mm). A first order low-pass filter attenuates magnitude of signals whose frequencies are above the cut-off frequency f_c in a linear fashion (slope of -20 dB in logarithmic scale) as shown in Figure 4.3.

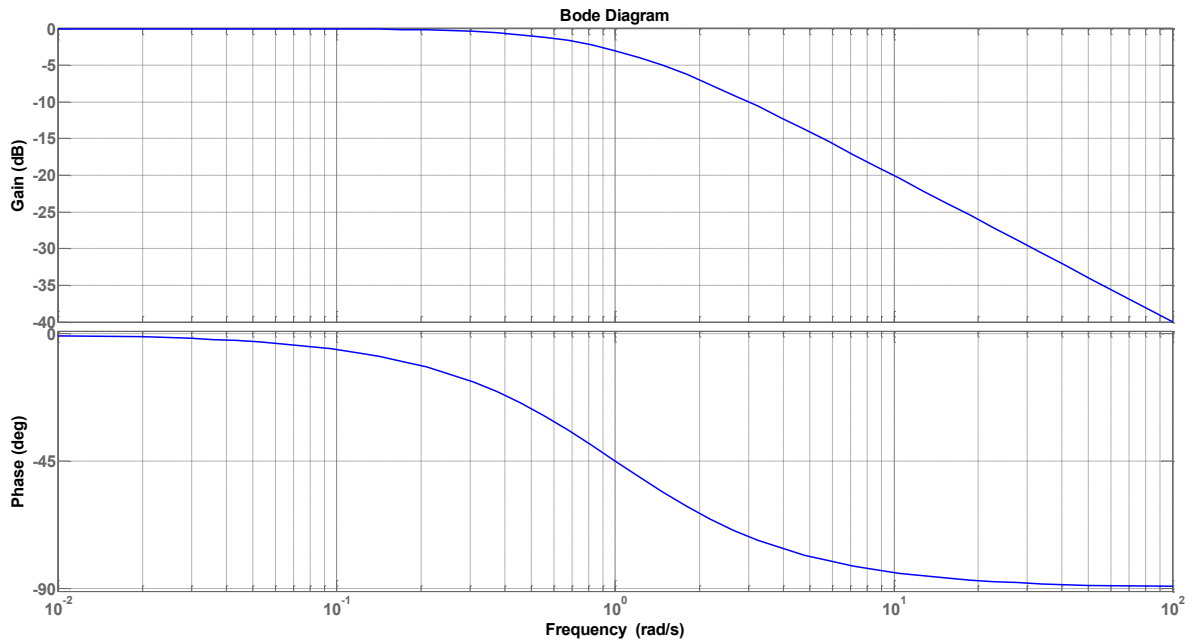


Figure 4.3 Response of a first order low-pass filter using a cut-off frequency of 1 rad/s corresponding to $v = 10$ mm/s and $d = 10$ mm.

While the calculation of approximate crack surface length is straightforward, there is not a single expression to relate the B_x signal to the crack pocket length, using the crack length, as the relationship depends on the crack shape. The existing methods either are based on a lookup table [112] containing different crack geometries that relate the B_x signal to the depth profile for a given crack surface length that were calculated theoretically, and for only a limited range of geometries, or are based on complex signal inversion algorithms; for example using neural network approaches [62, 63, 91]. In this experiment, the crack surface length and angle have been approximated based on the location of the maximum and minimum B_z on the contour map (Table 4.2), while the crack pocket length has been

estimated by curve-interpolation using first order (linear) approximation based on COMSOL simulations that have been carried out for semi-elliptical cracks (i.e. geometrically similar to those in the calibration rail) of different aspect ratios¹ (Figure 4.4). The inaccuracy on crack pocket length can be further improved given they are aspect ratios reported for rail RCF cracks.

Table 4.2 Comparison between the estimated and real crack parameters.

Crack	L (mm)		b (°)			K (mm)		L relative error %	b relative error %		K relative error %
	Est.	Real	Est.		Real	Est.	Real		Based on B_z	Based on B_x	
			Based on B_z	Based on B_x							
1	5.7	5	42.8	49.3	48	1.6-2.4	2	14	10.8	2.7	0-20
2	6.9	7	46.8	48.1	45	1.6-2.4	2	1.4	4	6.9	0-20
3	5.9	5	41.5	33.5	37	1.3-2.0	2	18	12.2	9.5	0-35
4	7.8	9	36.3	34.7	34	2.2-3.2	3	13.3	6.8	2.1	7-27

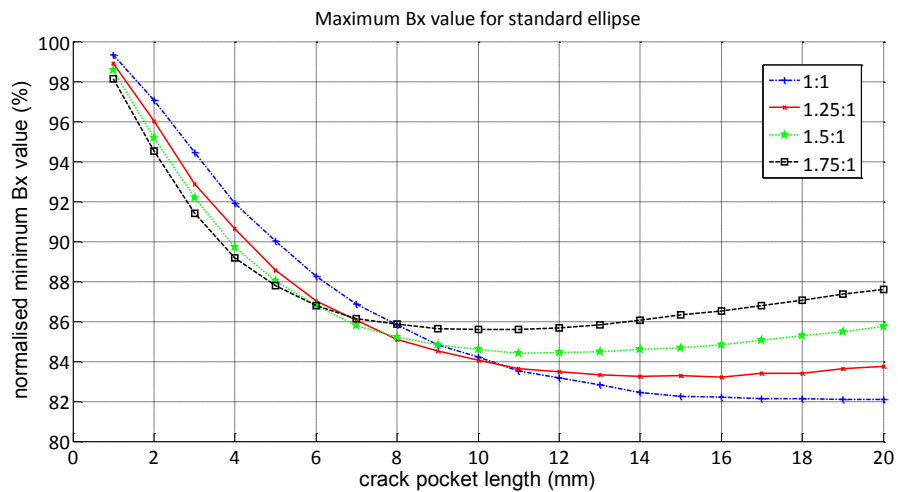


Figure 4.4 Relationship between the normalised B_x signal and crack pocket length obtained from COMSOL simulations of the ACFM signal for semi-elliptical cracks of different aspect ratios and dimensions [65].

¹ The aspect ratio is defined to be the surface length divided by twice the pocket length.

For cracks 1-4, the estimated surface length and angle to the rail length agrees well (within 20% error) with that of the actual crack surface length and angle. It should be noted that the accuracy of the results is influenced by the spacing between the successive ACFM scan lines. In this case a spacing of 0.5 mm has been used in order to achieve a good compromise between accuracy and scan time (a 3D scan over a single defect takes approximately 240 s).

Despite good agreement (i.e. maximum error of 7% for pocket length using a known aspect ratio) being found for the estimation of crack surface length and angle to the rail axis, it is not feasible to estimate the crack propagation angle into the rail (α) as the results do not show significant change for varying crack propagation angle (Figure 4.1 Crack 1 vs. Crack 2). This is however due to a fundamental limitation of the ACFM technique in predicting the crack propagation angle from the B_x signal, and has been reported in the literature [3].

For the scans over the multiple cracks 5-8 with a nominal 4 mm spacing between each crack, the results do not show any clear indication (e.g. individual peaks and troughs as for isolated cracks) of multiple cracks (Figure 4.5a). Identification of separate defects in a cluster depends on spacing between individual defects and also lift-off during inspection [113].

As there is no differentiation of the separate cracks, using the B_z signals to determine a crack surface length and angle (based on the location of maximum and minimum values in the contour map) gives significant error (estimated surface length of 18.4 mm compared to each individual crack of 10 mm, and estimated angle of 10° compared to actual of 32°). It can be seen from Figure 4.5a that the B_x signal shows a much broader signal, compared to the signal for cracks 1-4, indicating the presence of a wide defect. The magnitude of the B_x signal suggests a crack pocket length of 3.4 mm using a known aspect ratio of 1.25:1 on the

calibration curve, or of 2.8-4.0 mm based on the calibration curve and unknown aspect ratio, which compares to the true individual crack pocket length of 4 mm.

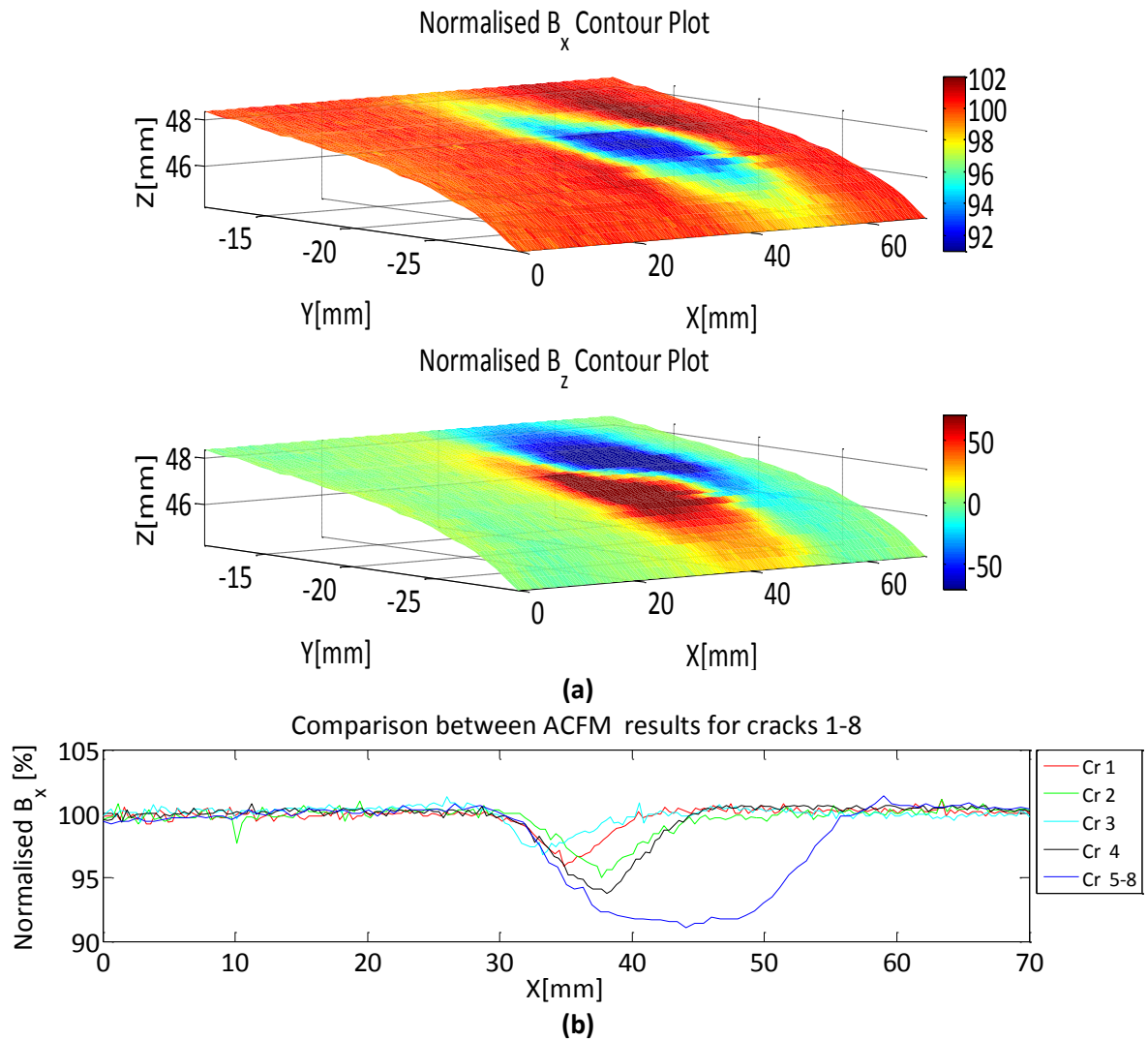


Figure 4.5 (a) Contour plots for the ACFM scan over multiple cracks 5-8 and (b) comparison between single scan line data showing the maximum change in B_x signal for the multiple cracks and single cracks (1-4).

4.3.2. Non-matching Probe Angle

To investigate the real scenario of automatic characterisation of an RCF crack at an unknown surface angle, a number of ACFM grid scans at different ACFM probe angle offsets have been carried out on cracks 1-4. The aim of the experiment was to assess the accuracy of the searching algorithm described in Chapter 3 (section 3.4.3.3) for prediction of an unknown crack surface angle and use this value for correction of the ACFM probe's initial angle. The offset angles used were chosen in such a way as to include a typical deviation of 22.5° from a mid-range angle of 52° with respect to the rail length, as reported for the RCF cracks [3, 8-10]. The values used in this experiment include -30 , -25 , -22 , 10 , 15 and 25° relative to the crack where the negative sign indicates an anti-clockwise direction. In each case, the ACFM probe was held at a constant lift-off and normal to the rail surface while the ACFM probe's movement conformed to the rail head profile. The results were then compared against COMSOL simulations [111] using similar crack geometries and angle offsets used for the experiment except that an assumption of a flat surface was used in the model (Figure 4.6 - Figure 4.9).

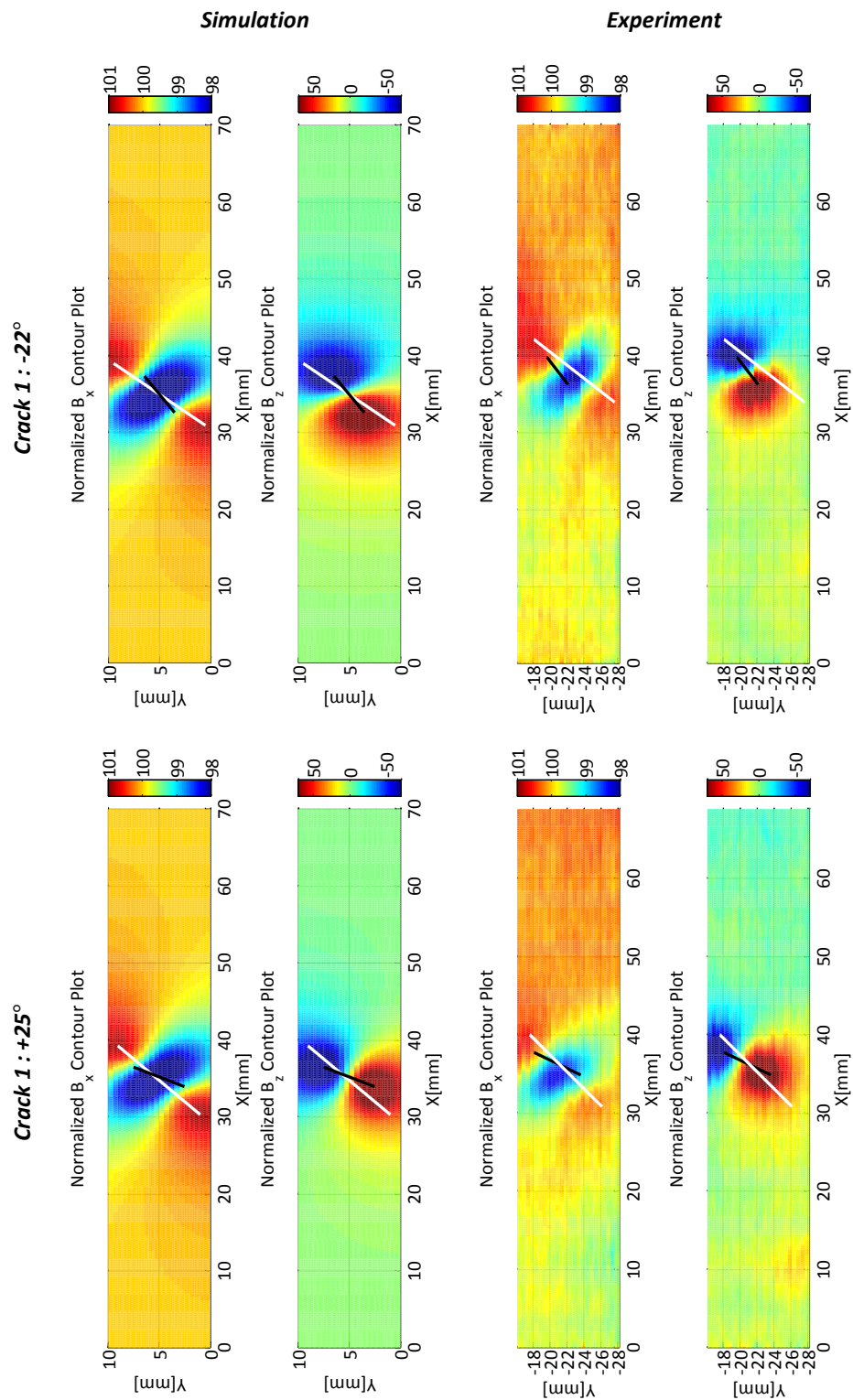


Figure 4.6 Comparison between experiment and simulation of 2D ACFM scans at two probe angle offsets for crack 1. The offset angles are measured relative to the crack. The white and black lines show the direction of crack length based on B_x and B_z signals, respectively.

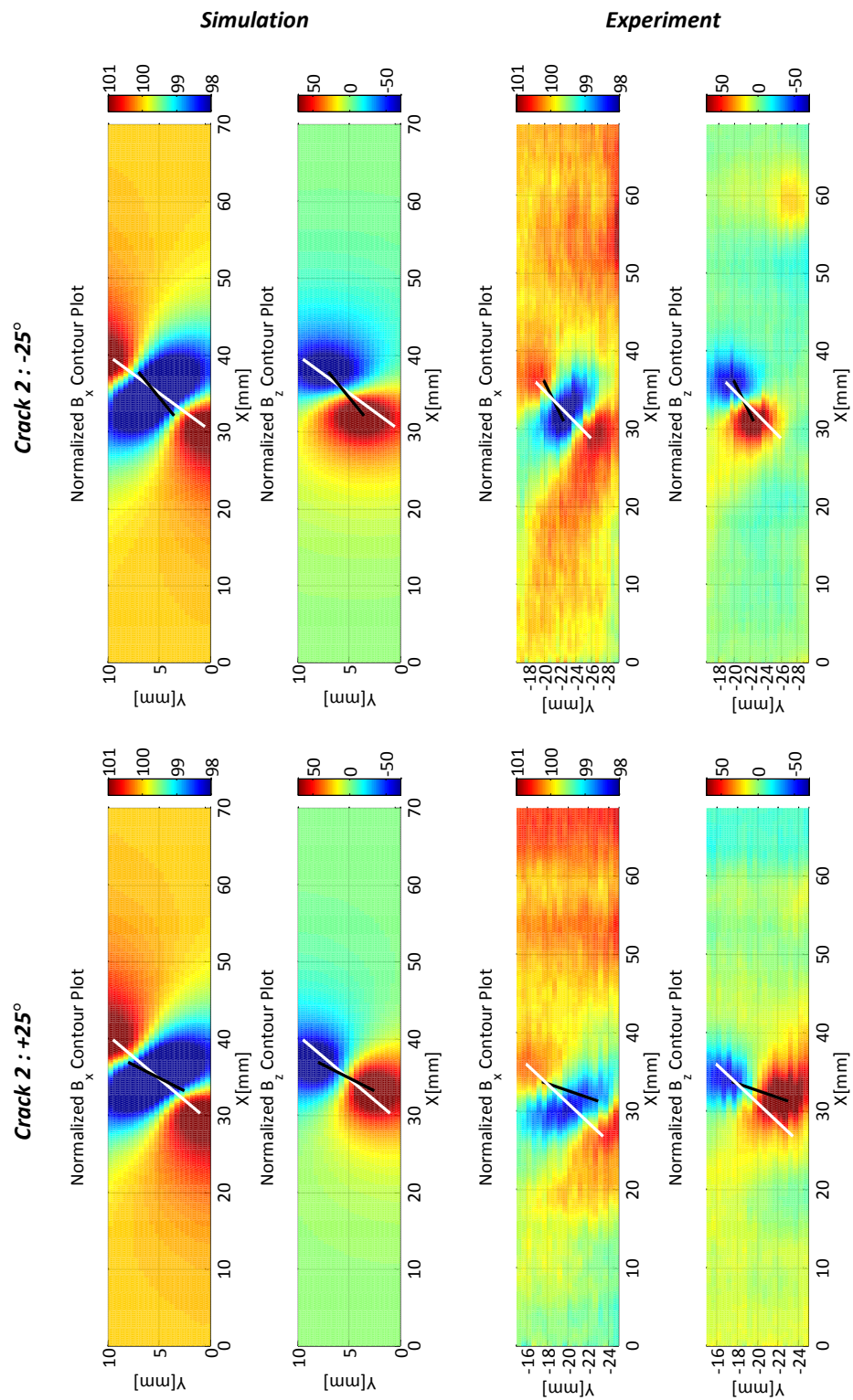


Figure 4.7 Comparison between experiment and simulation of 2D ACFM scans at two probe angle offsets for crack 2. The offset angles are measured relative to the crack.

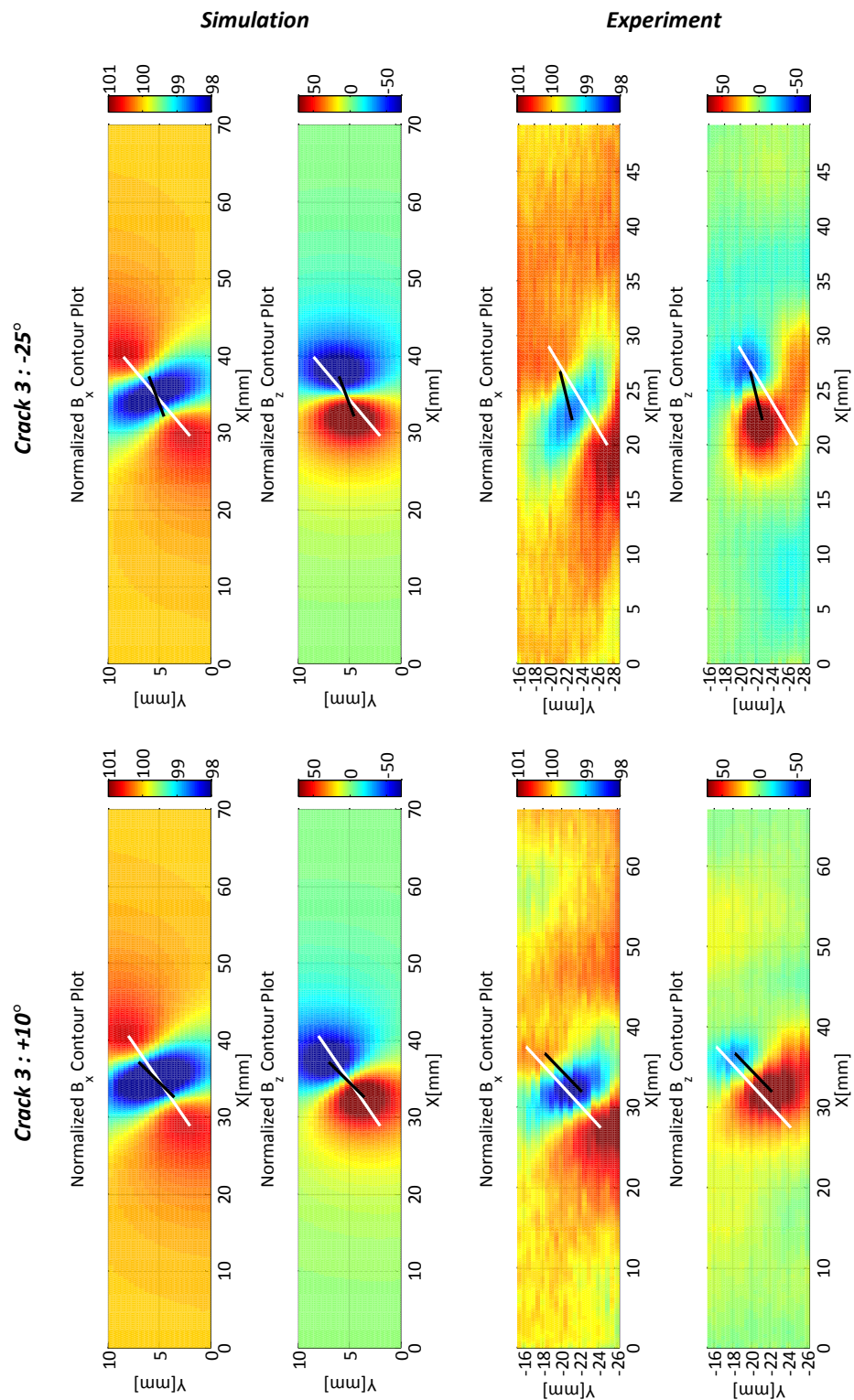


Figure 4.8 Comparison between experiment and simulation of 2D ACFM scans at two probe angle offsets for crack 3. The offset angles are measured relative to the crack.

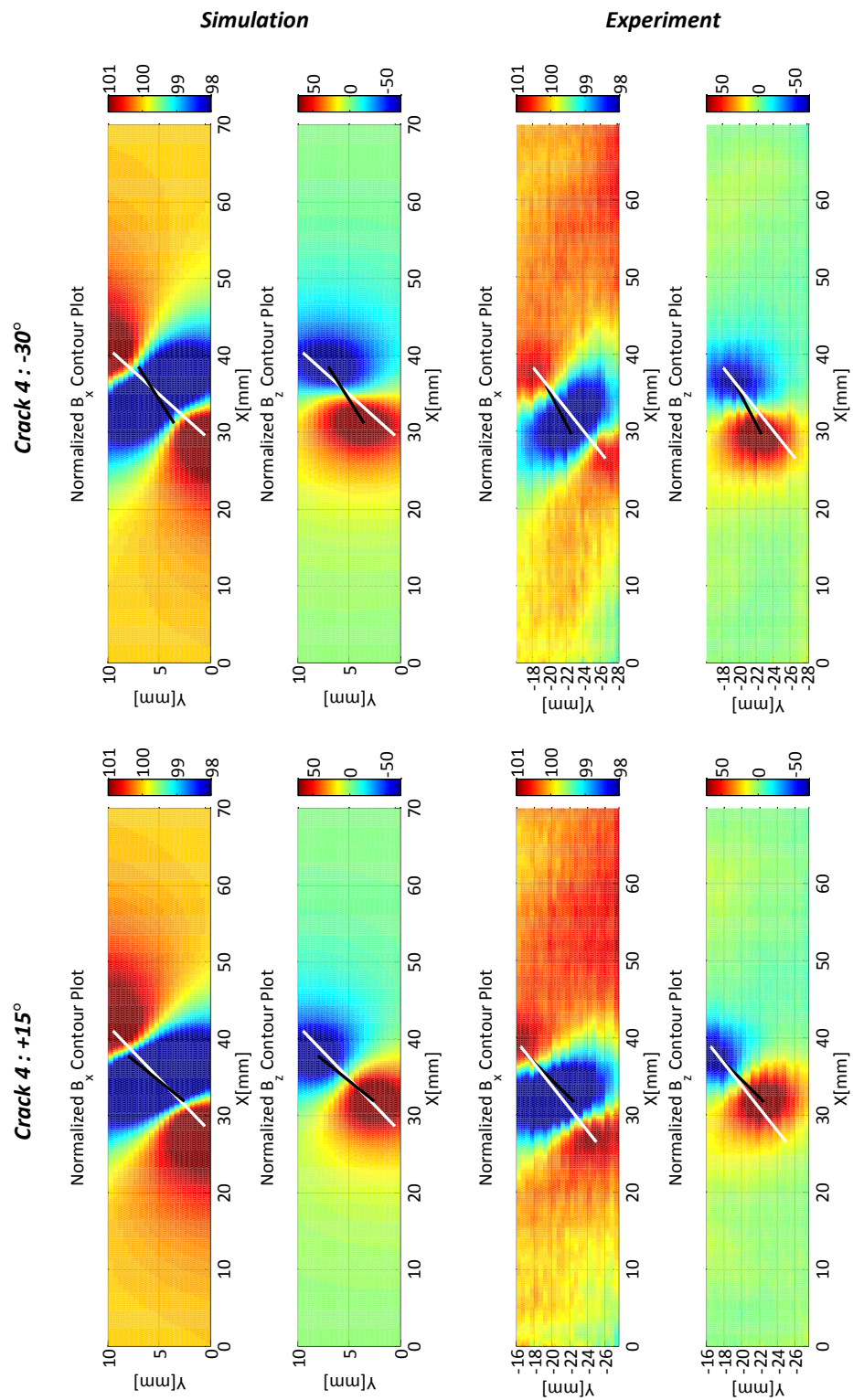


Figure 4.9 Comparison between experiment and simulation of 2D ACFM scans at two probe angle offsets for crack 4. The offset angles are measured relative to the crack.

It has been shown in section 4.3.1 that in the case of matching probe angle, the crack surface length and angle may be obtained within an error of 20% and 13%, respectively. In contrast, in the case of non-matching probe angle, as the B_z contour maps suggest, the presence of an angle offset influences the location of maximum and minimum B_z in the contour map (the black line on the contour maps indicates the direction of the crack as calculated on the basis of maximum and minimum B_z points) owing to the fact that the rotation of eddy current occurs at locations other than the crack ends. This effect can be observed for both positive and negative offset angles and is more prominent for larger angle offsets ($> 20^\circ$). Hence, it would result in an unacceptable error ($> 10^\circ$) for calculation of crack surface angle using the B_z signal (Table 4.3).

On the other hand, when using the B_x signal for the angle approximation, the error has been observed to be bounded within an acceptable range ($\leq 10^\circ$) even for larger angle offsets ($> 20^\circ$) owing to the fact that the location of maximum intensity of the induced current density is still near the crack ends (approximately along the crack length) regardless of the decreased angle of attack to the crack length.

Consequently, using the B_x signal for crack horizontal angle calculation suggests that the angle offset may be closely compensated for (within 10°) and therefore the 1D ACFM scan for sizing may be performed at close to the optimum angle. This hypothesis has been also supported by the numerical results of the searching algorithm based on the COMSOL simulations [111] (Table 4.4).

Table 4.3 The numerical results of crack surface angle calculation based on the experimental measurements for cracks 1-4 using uniform grid spacing of 0.5 mm.

Crack number	Angle offset (°)	Real angle (°)	Angle est. abs. error (%)		Angle est. abs. error (°)	
			Based on B_x	Based on B_z	Based on B_x	Based on B_z
1	-22	48	5.4	26.4	3.0	13.0
1	+25	48	9.5	30.1	5.0	14.0
2	-25	45	0.1	41.6	0.0	19.0
2	+25	45	11.8	47.3	5.0	21.0
3	-25	37	10.8	48.9	4.0	18.0
3	+10	37	5.2	10.4	2.0	4.0
4	-30	34	8.9	23.5	3.0	8.0
4	+15	34	3.2	22.4	1.0	8.0

Table 4.4 The numerical results of crack surface angle calculation based on the COMSOL simulation for cracks 1-4 using a uniform grid spacing of 0.5 mm.

Crack number	Angle offset (°)	Real angle (°)	Angle est. abs. error (%)		Angle est. abs. error (°)	
			Based on B_x	Based on B_z	Based on B_x	Based on B_z
1	-22	45	7.2	29.1	3.0	13.0
1	+25	45	7.1	40.5	3.0	18.0
2	-25	45	2.0	30.3	1.0	14.0
2	+25	45	8.0	25.0	4.0	11.0
3	-25	28	15.0	43.3	4.0	12.0
3	+10	28	3.1	33.3	1.0	9.0
4	-30	37	7.7	31.1	3.0	12.0
4	+15	37	2.7	15.3	1.0	6.0

4.3.3. Effect of Grid Spacing

The performance of the searching algorithm for different grid spacings and probe angle offsets is presented in Figure 4.10. In each case, the original data at 0.5 mm spacing has been re-sampled at wider spacings that are multiples of 0.5 mm. It should be noted that the scan region was chosen in such a way as to contain the crack while the starting position was selected randomly in order to mimic the uncertainty due to an unknown RCF crack. The results suggest that the grid spacing may be increased to 1.5 mm where the reduction of accuracy in crack surface angle is insignificant. Therefore the characterisation process may be performed three times faster than when using initial grid spacing of 0.5 mm. However, it

should be noted that the optimum grid spacing will vary with the crack surface length. It can be also seen from Figure 4.10 that for crack 4 (surface length of 9 mm) the grid spacing may be increased up to 4 mm where the error is bounded within 10°. For smaller surface lengths, closer grid spacings should be used to ensure the critical data corresponding to the middle of the crack and crack ends are sampled. In this study the minimum crack surface length of 5 mm allows the use of wider (1.5 mm) grid spacing. However, in a real experimental scenario where the crack’s surface length is unknown to the robotic system, a closer spacing (e.g. 0.5 mm) should be used. It is also evident that the performance of the searching algorithm becomes unreliable for a grid spacing of greater than 2 mm. In fact, the accuracy of the algorithm is associated with the chance of performing a scan at the distance from the rail’s gauge corner that produces the maximum change in B_x signal. Increasing the grid spacing leads to a reduction of the probability at which a scan line containing the maximum B_x signal is achieved.

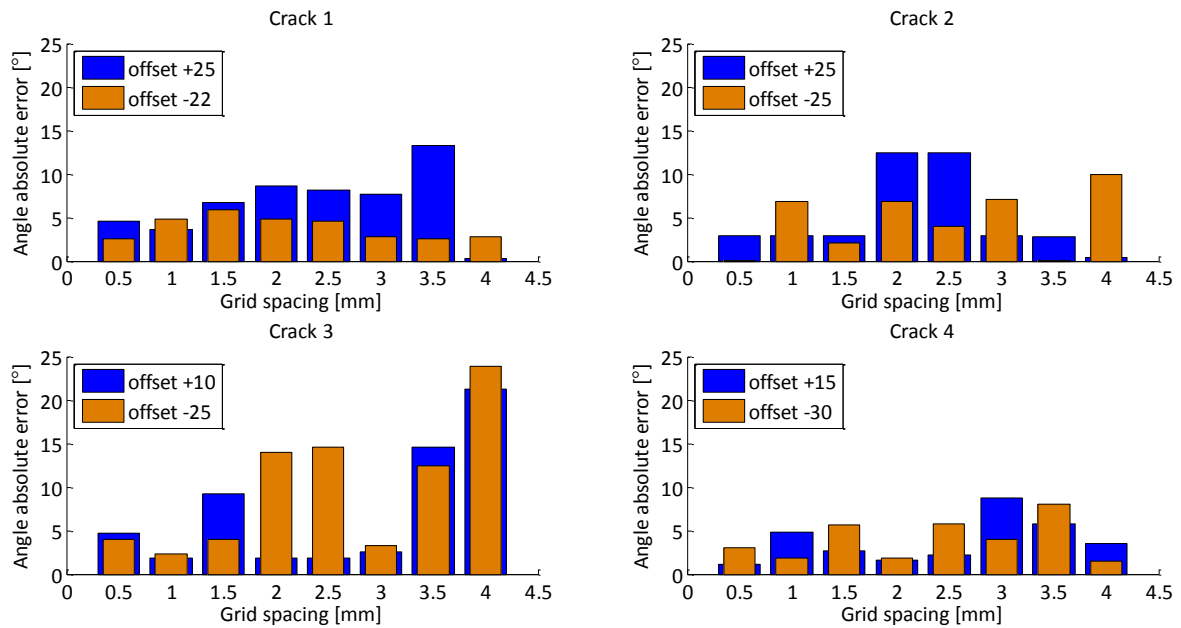


Figure 4.10 Effect of grid spacing on crack angle calculation by the searching algorithm for different probe angle offsets.

4.3.4. Effect of ACFM Sensor Lift-off and Signal to Noise Ratio

The probe's lift-off plays a vital part in the accuracy of crack characterisation. Increasing the sensor lift-off lessens the sensitivity of the B_x signal to a defect, Figure 4.11. It can also be analytically shown [59, 91, 114] that in the frequency domain; a non-zero value of lift-off has a low-pass filtering effect on the crack surface signal (i.e. signal measured at zero lift-off) attenuating sharp variations in the B_x signal due to crack ends. For the scans along the crack opening at a non-zero lift-off, the surface B_x signal may be restored by the following equation:

$$\begin{cases} \tilde{B}_x(m, n, 0) = \tilde{B}_x(m, n, lo) e^{\gamma lo} \\ \gamma = \sqrt{m^2 + n^2} \end{cases} \quad (4.5)$$

where lo is the lift-off, $\tilde{B}_x(m, n, 0)$ is the two dimensional Fourier transform (FT) of the B_x signal at the surface of the specimen, $\tilde{B}_x(m, n, lo)$ is the two dimensional FT of the B_x signal measured along the crack at the lift-off lo while m and n are the Fourier variables corresponding to x and y coordinates, respectively. Therefore the surface B_x signal may be computed by applying an inverse FT to the left hand side of Equation (4.5).

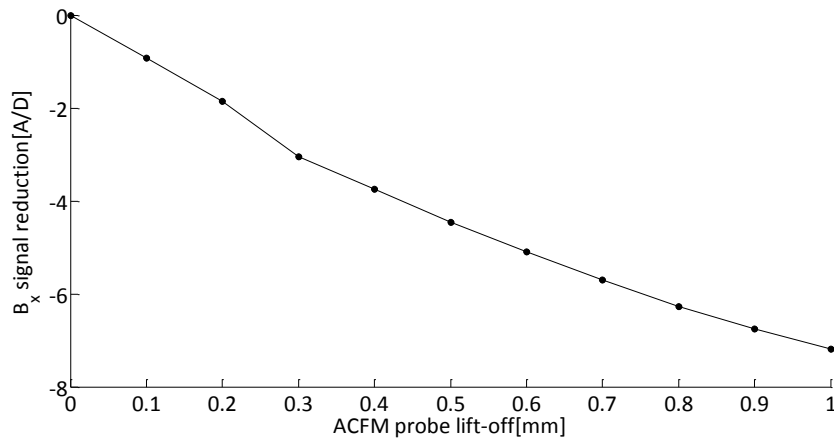


Figure 4.11 Reduction of B_x signal due to increasing probe lift-off. The measurements were taken on UIC54 rail using the robot arm at different probe lift-offs and in the absence of a defect.

Equation (4.5) becomes very helpful in applications where a zero lift-off ACFM scan is not feasible, but for accurate crack sizing it is still required to use zero lift-off as the reference signal. However, in this research, with the aid of the laser sensor and robot arm, the ACFM sensor lift-off can be accurately controlled at a desired value about which a reference signal (calibration curve) is available. Increasing the probe's lift-off is a hardware-based approach in smoothing the data collected at the cost of attenuating the non-noise high frequency components in the B_x signal owing to crack ends where the induced current intensity increases. As the searching algorithm works on the basis of the existence of peaks in the scan lines, the lift-off may be increased to a maximum value where the peaks are still detectable.

For this purpose, a number of transverse ACFM scans across the UIC54 rail head were recorded in order to determine the repeatability and accuracy of the robotic scans. The measurements were taken in the absence of defects at three different locations along the UIC54 rail and repeated three times each. The accuracy of the ACFM point measurements using the robot arm has been found to be 5 A/D units (16 bits resolution) as shown in Figure 4.12. This enabled finding the maximum appropriate value for the probe's lift-off. In doing so, several robotic scans along the opening of a semi-elliptical crack at different lift-off values were taken as shown in Figure 4.13. It is evident that for the first and second crack (10x5 mm and 5x2 mm), the peaks in the B_x signal are still detectable at lift-off value of 3 mm while for the third defect (2x1 mm) they are missed for even 1 mm lift-off as the increment in the B_x signal is close to the measurement accuracy. Therefore, the maximum tolerable lift-off will depend on the crack pocket length. For characterisation of an unknown crack, it is therefore suggested to use the minimum lift-off possible (e.g. 0.2 mm).

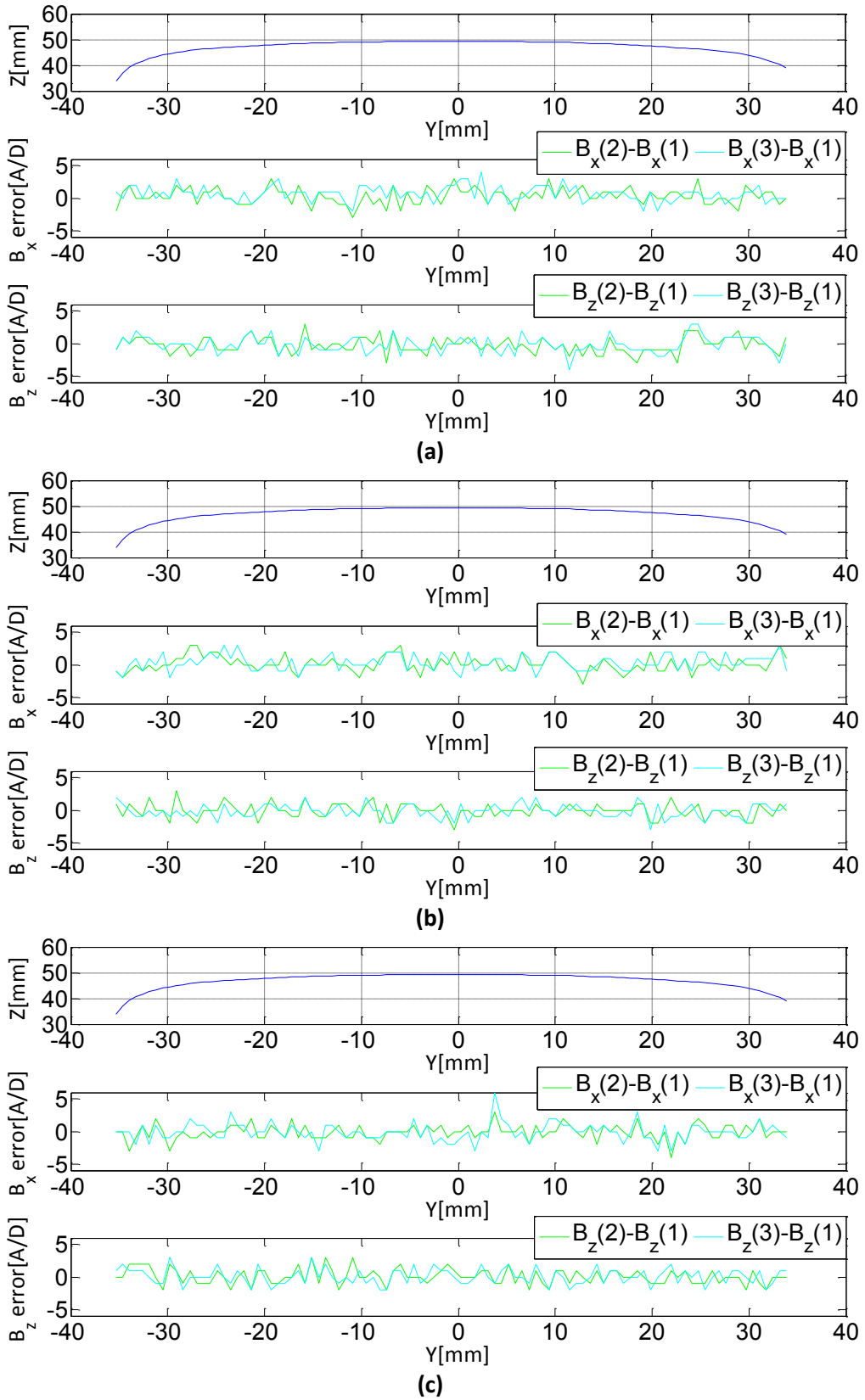


Figure 4.12 Demonstration of the repeatability of the ACFM point measurement (transverse scan from left to right) using the robot arm for three different locations along the UIC54 rail: (a) first (b) second and (c) third location.

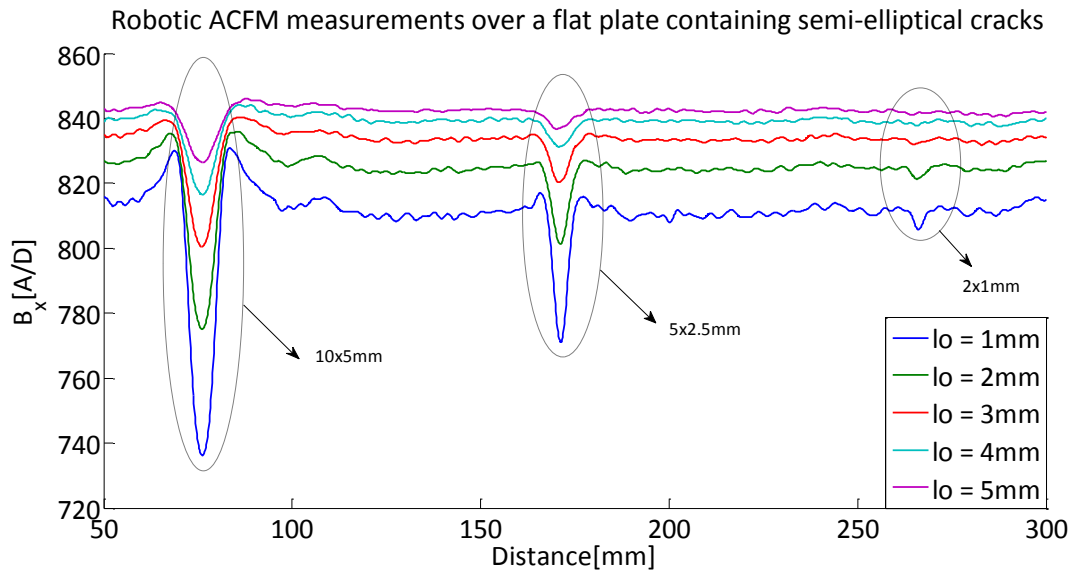


Figure 4.13 Comparison of B_x signal for different lift-off values for robotic scans along the opening of three semi-elliptical cracks having aspect ratio of 1:1.

4.4. Summary

In this chapter the results of static ACFM measurements on series of artificial RCF cracks using the developed robotic system have been discussed. It was shown that the ACFM probe's lift-off and orientation must be controlled in order to accurately size the cracks (within 7% error based on a known crack aspect ratio). It was also demonstrated that the ACFM probe's lift-off and orientation can be accurately controlled by the robot arm through *a priori* rail profile measurement.

In order to mimic the real scenario of an automatic ACFM scan over an unknown RCF crack, different initial ACFM probe angle offsets – based on a reported range of angles for real RCF cracks - were used. It was found that using the B_x signal, the unknown crack surface angle can be approximated to within 10° (where the change of the signal drop ΔB_x due to angle offset is insignificant) by performing constant lift-off grid scans (using random starting points) over the measured rail profile for grid spacings of up to 1.5 mm.

Chapter 5. Case Study: using the Robotic System for Automatic Detection and Characterisation of RCF Cracks

5.1. Introduction

This chapter discusses the second of three case studies that builds on Chapter 4. It is designed to study the dynamic results of trials carried out at the Long Marston Railway line. The trials include both automatic detection runs to locate defects, automatic positioning over the defect and characterisation scans of the defect. Additionally, a combined threshold and signature match (CTSM) algorithm developed for automatic detection of RCF cracks is presented and the results of applying the CTSM algorithm to the field trial results to automatically identify defects are discussed.

At present, the detection of surface breaking defects using ACFM is carried out manually using human operators (see section 2.3.8.3). For example as the ACFM walking stick is pushed along the rail track the output ACFM signal is visually observed and any sudden drop in the ACFM signal (B_x) is detected by human eye and taken as an indication of a defect; the corresponding position along the length of the rail is then recorded. Vehicle mounted deployment of the ACFM technology is still under development where automated defect detections would be required [67].

5.2. CTSM Algorithm

The use of thresholding for automatic defect detection has been very common within the NDT industry [115-134]. The technique is directly applicable on data for which the background level remains fairly steady. In such cases, by setting an appropriate threshold value on the signal of interest, the abnormal event (fault) can be detected once the data exceeds or falls below (depending on the nature of the application) the threshold value. This approach may be used to detect RCF defects from ACFM signal where the lift-off variations are fairly small compared to the crack pocket length (e.g. see results of turning lathe test by Papaalias, et al. [54]). In contrast, in the case of field trials, significant change of background level due to lift-off change (> 2 mm) would render the threshold algorithm ineffective. This is demonstrated in Figure 5.1 where the results correspond to the robotic ACFM detection scans at Long Marston Railway line containing a number of artificial cracks. Different threshold lines indicate deviation from the average B_x signal at different ratios that are multiples of standard deviation (SD) of the B_x signal. As it can be observed from Figure 5.1, setting a low threshold (e.g. 3SD or 4SD on the graph) may result in some defect signals (corresponding to a small signal drop) being missed while a high threshold (e.g. 1SD or 2SD on the graph) generates a lot of false indications. Therefore it is difficult to choose just one threshold that works well. This problem is even more pronounced in the case of high speed ACFM measurements as shown in Figure 5.2.

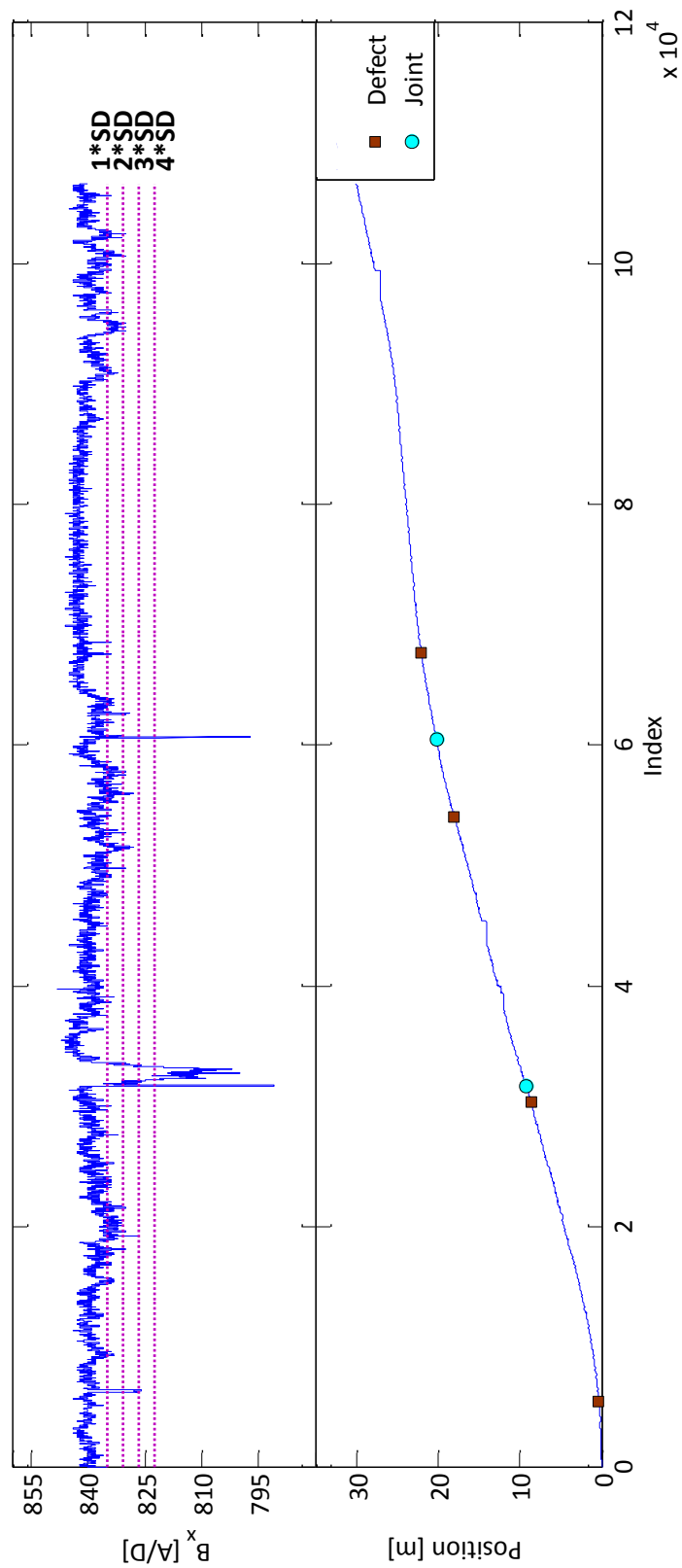


Figure 5.1 Demonstration of thresholding method for low speed detection of defects using the developed robotic system at the Long Marston Railway line. The dashed lines show the thresholds used for defect detection. See Table 5.1 for the detailed explanation of the defects.

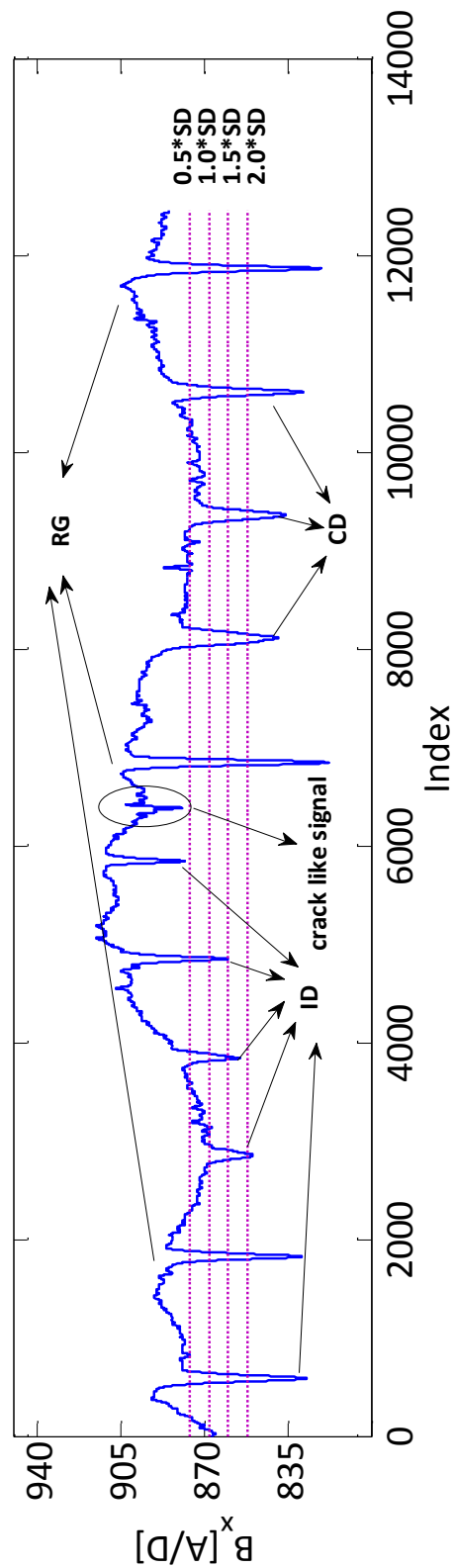


Figure 5.2 Demonstration of thresholding method for detection of defects from high speed ACFM measurements on rotating rail rig at 48 km/h using a 50 kHz probe [54]. Labels: RG → Rail Gap, ID → Isolated Defect, CD → Clustered Defect. The dashed lines show the thresholds used for defect detection.

In the CTSM method, the signal reduction with respect to its local background level is considered. To achieve this, the signal is first smoothed by using a first order low-pass filter (discussed in Chapter 4, section 4.3.1) with a normalised cut-off frequency f_c given by Equation (5.1). The filtered signal is then shifted backward in the time domain by a speed dependent latency parameter τ (integer number) given by Equation (5.2) and subtracted from the original filtered signal. This approach has an advantage of increased sensitivity (i.e. SNR) to defect compared to use of numerical differentiation (based on successive samples) and has been previously employed by Bentoumi, et al. [38] for automatic detection of rail surface defects from EC sensor. Besides, it produces a differential signal for which the background level remains fairly steady (approximately near zero). The differential signal (Equation (5.3)) contains information on the variation of the B_x signal due to the presence of defects or rail joints. It also has a stable background (approximately near zero). Therefore, based on the signal variation from Equation (5.3) the presence of cracks can be detected by setting an appropriate threshold value.

In this research, the novel CTSM method is proposed to improve on the uncertainty introduced in the threshold method. In the CTSM method, candidate crack signals are identified by thresholding the ΔB_x signal. Consequently, the candidate signals are examined by a non-linear curve fitting algorithm which attempts to fit a crack signature to the candidate signal. The crack signature is approximated by an analytical function (Equation (5.4)), which is the negated derivative of the generalised normal distribution function (Figure 5.3 top). The advantage of this approach over a simple threshold method based on the ACFM output signal is discussed in detail when considering the high speed ACFM data in section 5.4.2.

The unknown parameters of the crack signature $a_i > 0$ ($0 \leq i \leq 2$) are found by the least square method using the Levenberg-Marquardt optimisation algorithm on the basis of minimising the cost function J expressed in Equation (5.5). The acceptance of each candidate signal is judged based on the quality of the fit (QOF), which is determined from the normalised norm of residuals (Equation (5.6)).

$$f_c = \alpha \frac{\bar{v}T_s}{d} \quad (5.1)$$

$$\tau = \left[K \frac{d}{\bar{v}T_s} \right] \quad (5.2)$$

$$\Delta B_x(i) = B_x(i) - B_x(i + \tau) \quad (5.3)$$

$$S(i) = a_0(i - a_2)e^{-a_1(i - a_2)^2} \quad (5.4)$$

$$J = \sum_{i=1}^N (S(i) - \Delta B_x(i))^2 \quad (5.5)$$

$$QOF = \left[\left(1 - \frac{J}{\sum_{i=1}^N \Delta B_x(i)^2} \right) * 100 \right] \quad (5.6)$$

where α and K are dimensionless correction factors introduced to improve on the uncertainties due to using an average speed \bar{v} (m/s), d is the signal drop region (m), T_s is the sampling interval (s) and QOF is a dimensionless integer value between 0 and 100 representing the quality of fit after optimisation.

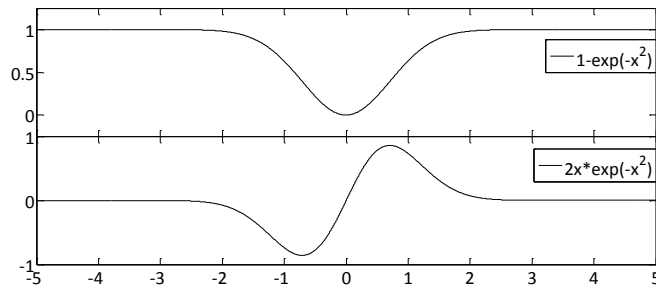


Figure 5.3 Representation of the analytical signature for a B_x signal due to a single RCF type defect (top) and its analytical derivative ΔB_x (bottom).

5.2.1. Avoidance of Local Minima Traps

Due to the non-linear nature of the cost function J , several local minima may exist. If the parameters a_i are not correctly initialised, the algorithm may become trapped in local minima, which would result in misclassification of the candidate signals. In order to avoid this occurrence, prior knowledge about the behaviour of the parameters a_i has been exploited. To this end, the parameter a_0 (used for scaling) is initialised as the maximum value of the ΔB_x signal. The parameter a_1 (used for dilation) controls the location of both the maximum and minimum in the ΔB_x signal and is initialised according to Equation (5.7). Finally, the parameter a_2 (used for shifting in the time domain) is initialised based on Equation (5.8).

$$a_1 = \frac{2}{(x_{max} - x_{min})^2} \quad (5.7)$$

$$a_2 = \frac{x_{max} + x_{min}}{2} \quad (5.8)$$

where x_{min} and x_{max} denote the location of the minimum and maximum in the ΔB_x signal, respectively. Figure 5.4 shows the block diagram of the CTSM algorithm.

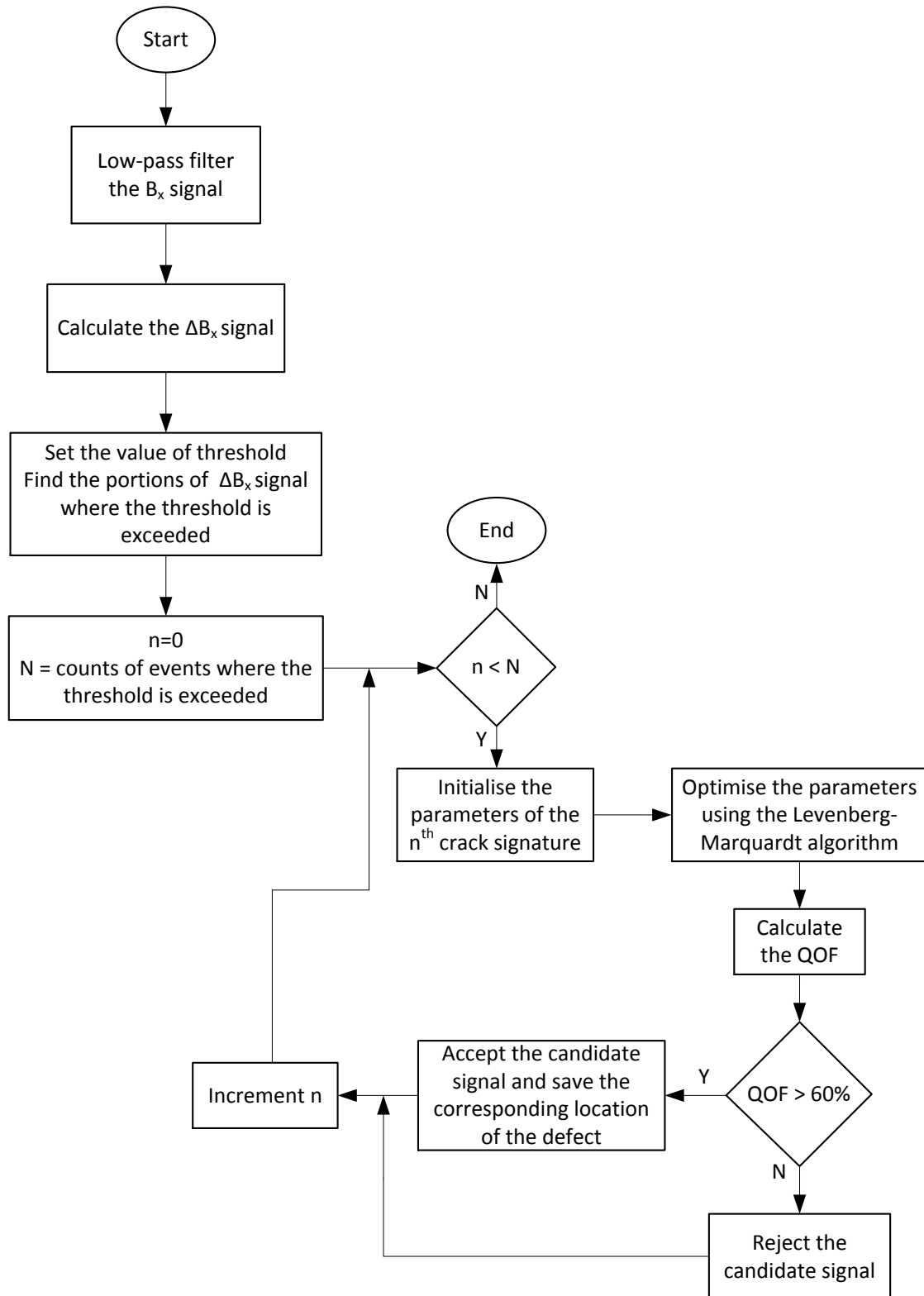


Figure 5.4 The process flow representation of the CTSM algorithm.

5.3. Experimental Setup

For the purpose of this experiment, 30 m of rail track has been used for inspection by the robotic system (Figure 5.5). As there were no known RCF defects in the desired section of the track, several artificial defects of simple geometry were introduced at different positions along the rail track in order to mimic RCF cracks using a hacksaw blade (Figure 5.6). The inspected section also contained two rail joints. The positions of these defects/joints were measured with respect to a fixed datum on the rail track; see Table 5.1.

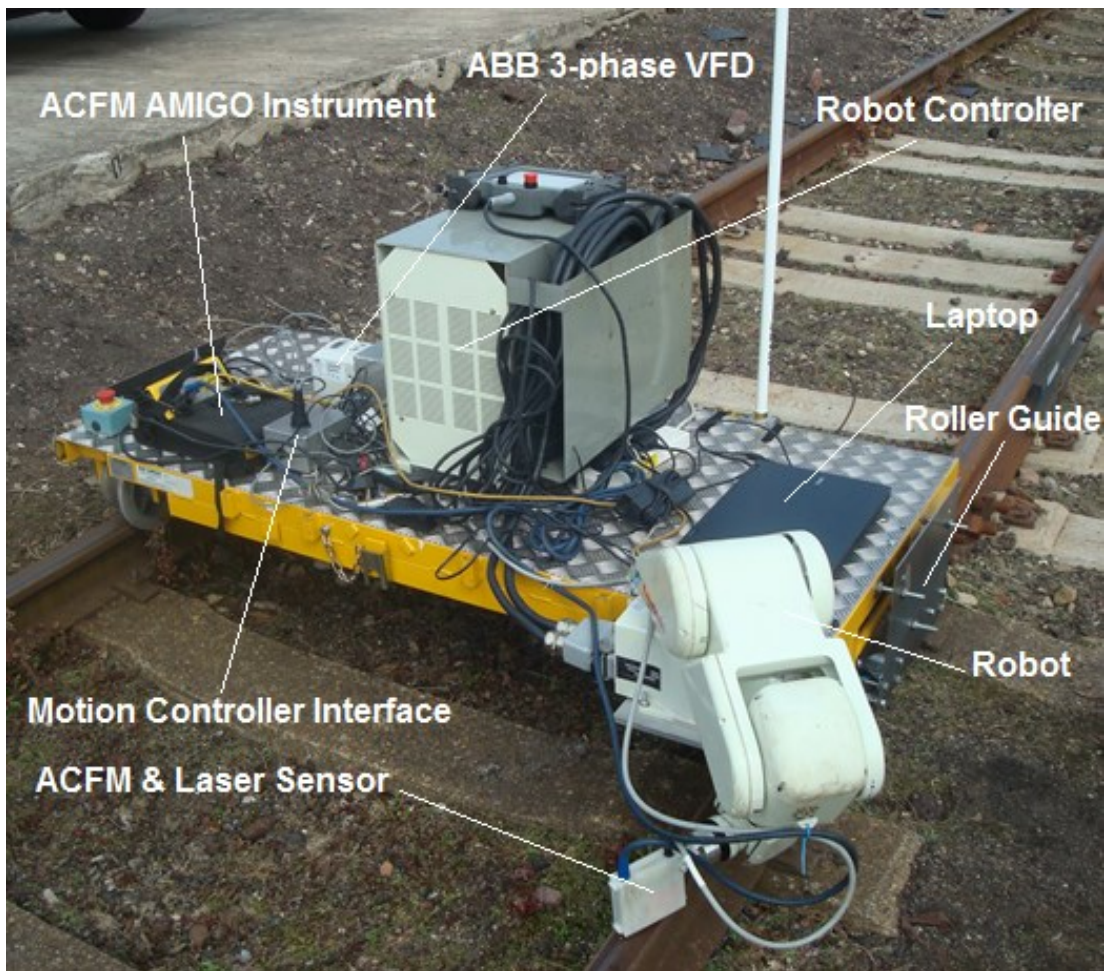






Figure 5.5 Photograph of the developed robotic system at Long Marston Railway.



Figure 5.6 The artificial defects of varying geometries on the rail track. The numbers represent the order in which the defects appear relative to the fixed datum.

Table 5.1 Quantitative information on the artificial defects/rail joints.

Fault type	Position (m)	Surface length (mm)	Maximum depth (mm)	Surface angle (°)	Approx. geometry (cross sectional view)
Defect (Crack 1)	0.365	20	5	90	
Defect (Crack 2)	8.650	30	1.5	35	
Rail Joint	9.240	-	-	-	-
Defect (Crack 3)	18.000	20	2	27	
Rail Joint	20.230	-	-	-	-
Defect (Crack 4)	22.000	30	2	39	

5.4. Results

5.4.1. Low-speed Detection Scans using the Robotic Trolley

The rail was inspected by the robotic system at a speed of 5 km/h while the ACFM probe was held at an initial lift-off of 3 mm and an angle of 52° with respect to the running direction. The results of two trials are shown in Figure 5.7 and Figure 5.8. As can be observed from Figure 5.7, in the first trial, the CTSM algorithm successfully detects three defects and both joints using a QOF $> 60\%$, however, the second defect was missed. Non-fault signals that were above the threshold value (twice the standard deviation of the ΔB_x signal) have been successfully ignored using a QOF $\leq 60\%$. Similarly, in the second trial, run with identical set up parameters, (Figure 5.8), two defects and the two joints were detected; however the second and third defects were missed while some non-fault signals have passed the acceptance criteria. A more detailed plot of the candidate signals (CS) with QOF $> 60\%$ and $\leq 60\%$ is shown in Figure 5.9.

The missed fault signals are due to the lateral movement of the ACFM probe (observed during the field trials) which results in a loss of sensitivity of the ACFM signal to a defect (either due to excessive lift-off taking place when the trolley hunts toward the gauge side or the fact that the ACFM probe didn't pass over the defect – the B_x signal drop falls within the measurement accuracy when the distance from the centre of the probe to the crack end is less than approximately 2 mm). In addition, any sudden up-down movement of the probe either due to mechanical imbalance due to misalignment of the rail tracks at the rail joint or due to random oscillation of the probe during the motion (this was observed during the field

trials) has the potential to develop a crack-like signature as the ACFM signal is lift-off dependent.

There is no fixed rule for choosing a threshold value for the QOF. In this research, an intermediate value of 60% has been chosen experimentally. Generally, using an intermediate threshold value as used here has an advantage that most of the real crack signals can be detected while the number of false indication is kept to a minimum.

It should be noted that even in the case of a using a very low threshold for the QOFs, the CTSM algorithm offers better performance than the simple threshold method. In other words, despite lift-off change, number of misdetection can be reduced to zero provided the ACFM probe passes over defect at the required lift-off. Also, the number of false detections would be comparably smaller than the threshold method as they only contribute to the sudden up-down movement of probe rather than a gradual lift-off change. The performance of the CTSM algorithm is summarised in Table 5.2.

The limitations due to ACFM probe lift-off and trolley hunting could be addressed using ACFM array sensors to cover wider area of the rail head. Further, the number of false detections due to sudden up-down movement of the probe may be largely improved by measuring the ACFM probe's instantaneous lift-off using a low-cost distance laser sensor; the crack-like signatures associated with a sudden up-down movement of the probe would appear as short wavelength laser signals and could therefore be distinguished from the actual crack signals.

Table 5.2 Performance of the CTSM algorithm in automatic detection of faults (i.e. artificial defects and rail joints) based on the ACFM measurements taken at Long Marston Railway line using the robotic system.

	<i>Trial 1</i>	<i>Trial 2</i>
<i>Number of correct detections</i>	5	4
<i>Number of false detections</i>	0	1
<i>Number of misdetections</i>	1	2
<i>Total number of faults</i>	6	6

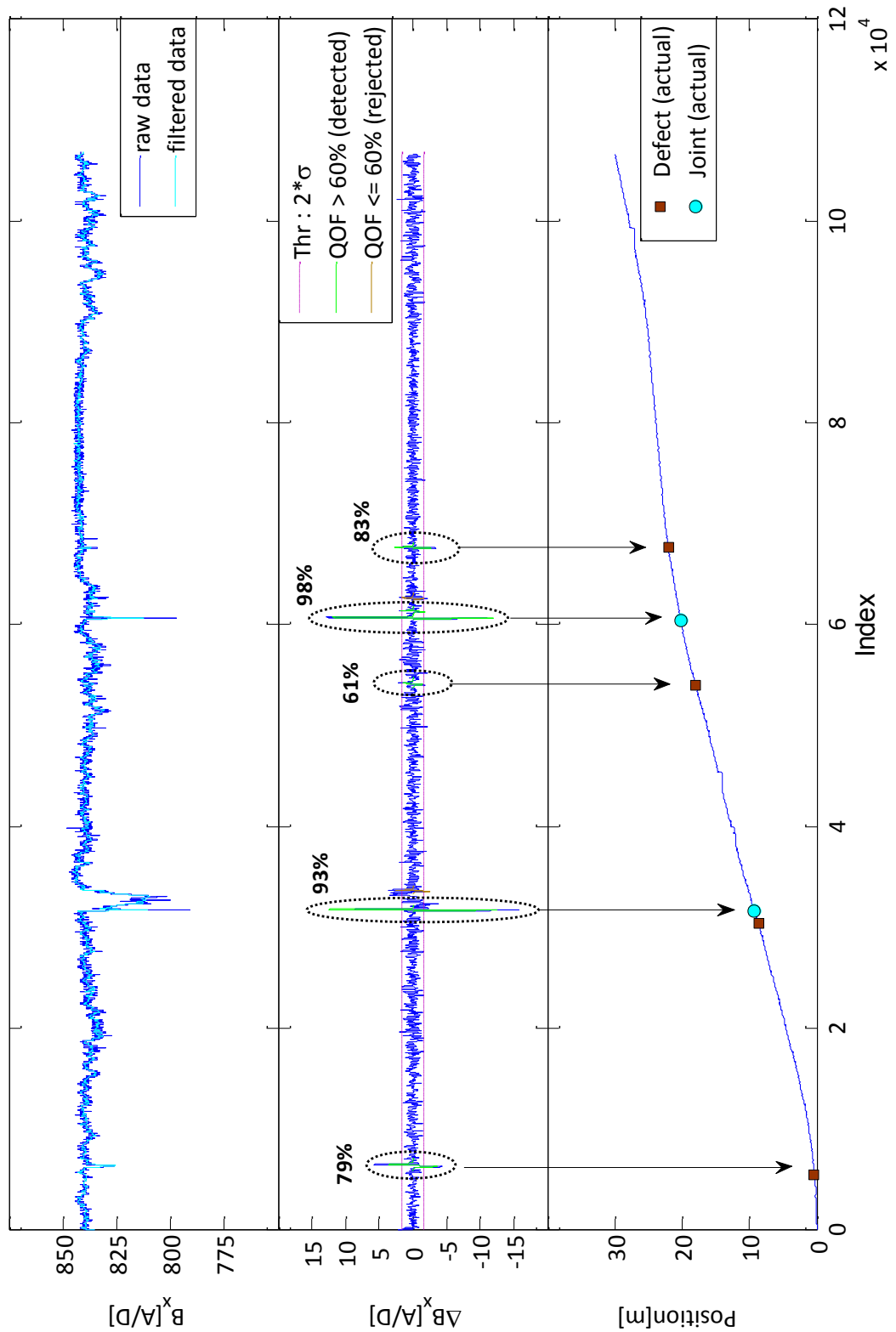


Figure 5.7 The results of detection scan with the robotic system at 5 km/h with an initial ACFM probe lift-off of 3 mm and angle of 52° with respect to the running direction for the first trial. The top graph represents the B_x signal, the middle graph represents the relative change of B_x signal with respect to its local background (ΔB_x) and the bottom graph represents the instantaneous position of the trolley.

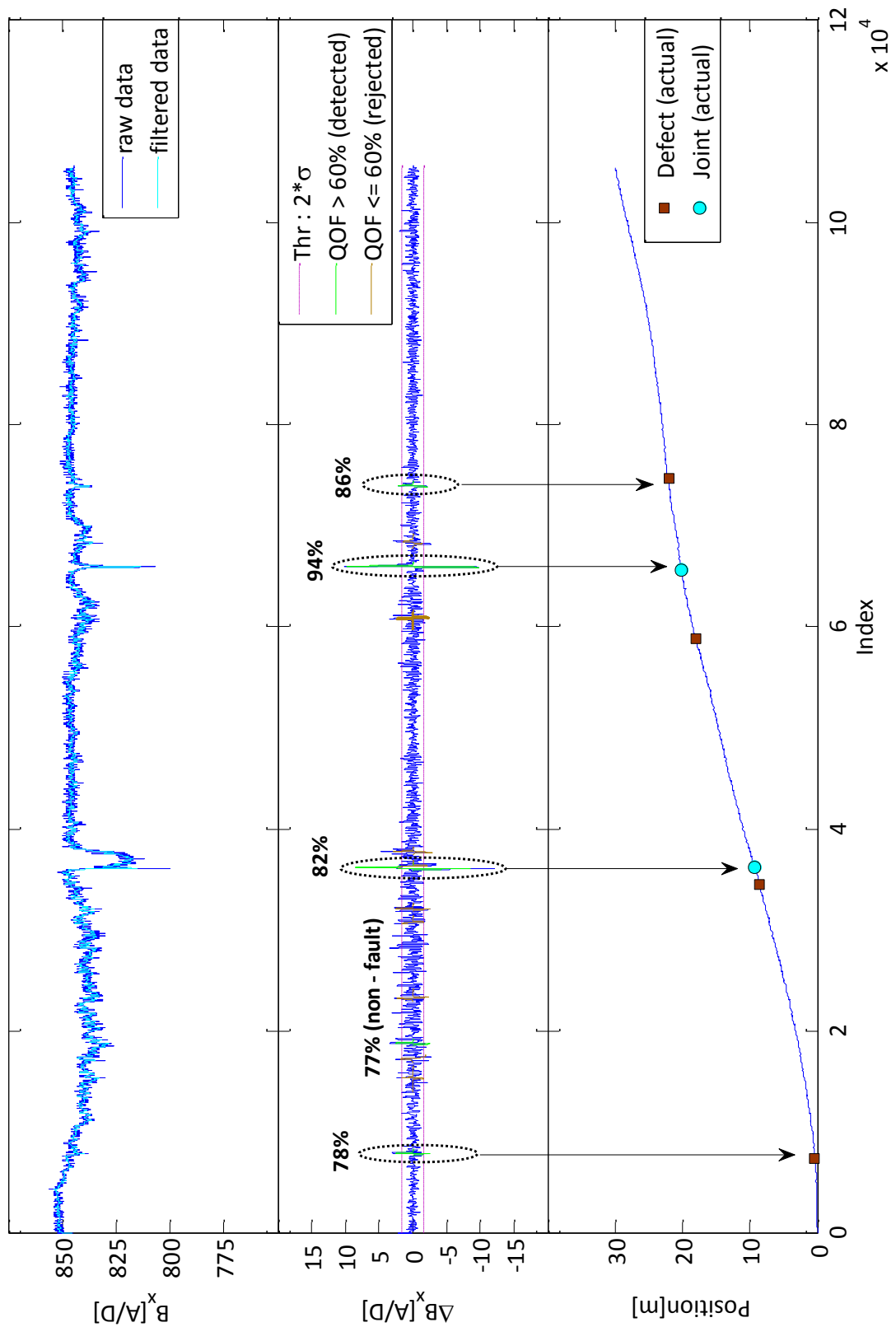


Figure 5.8 The results of the detection scan with the robotic system travelling at 5 km/h with an initial ACFM probe lift-off of 3 mm and angle of 52° with respect to the running direction for the second trial.

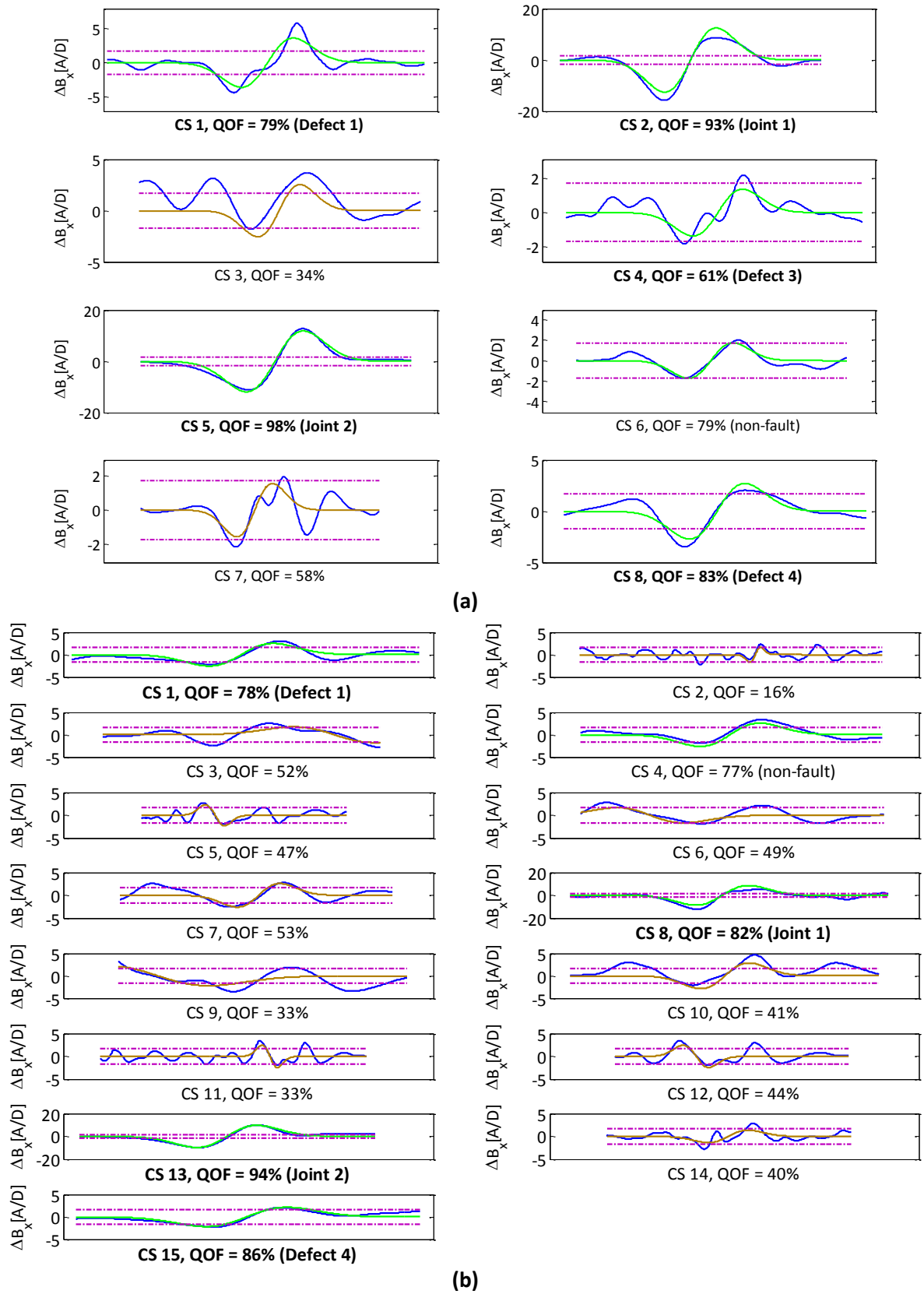


Figure 5.9 Plot of ΔB_x data in the vicinity of each CS for the (a) first and (b) second trials. The accepted and rejected crack candidate signals are marked in green and brown, respectively.

5.4.2. High-speed Detection Scans using Rotary Rail Rig

It was previously demonstrated that a simple threshold method would fail to correctly detect all defects in the case of severe lift-off change (Figure 5.2). To study the robustness of the CTSM algorithm on data obtained at higher inspection speeds, the results of high speed ACFM scans carried out previously by Papaelias, et al. [56] have been re-analysed using the new algorithm. A 1.8 m radius rotary rail rig (Figure 5.10) consisting of eight pieces of curved rail containing a series of artificially induced cracks (isolated slots, clusters of angled defects and semi-elliptical defects representative of RCF defects) machined into the rails' surface (Figure 5.11). The rig is capable of spinning up to 80 km/h. A customised trolley (Figure 2.18) was built to enable a 50 kHz ACFM probe to be held in position and also reduce the lift-off effects when the probe travels from one piece of rail to the other. Despite using the holding mechanism, the lift-off variation was, however, found to vary from 1 to 6 mm where the greatest lift-off was observed in the middle of each rail segment.



Figure 5.10 *Illustration of the rotary rail rig at the University of Birmingham used for high speed ACFM measurements [56].*

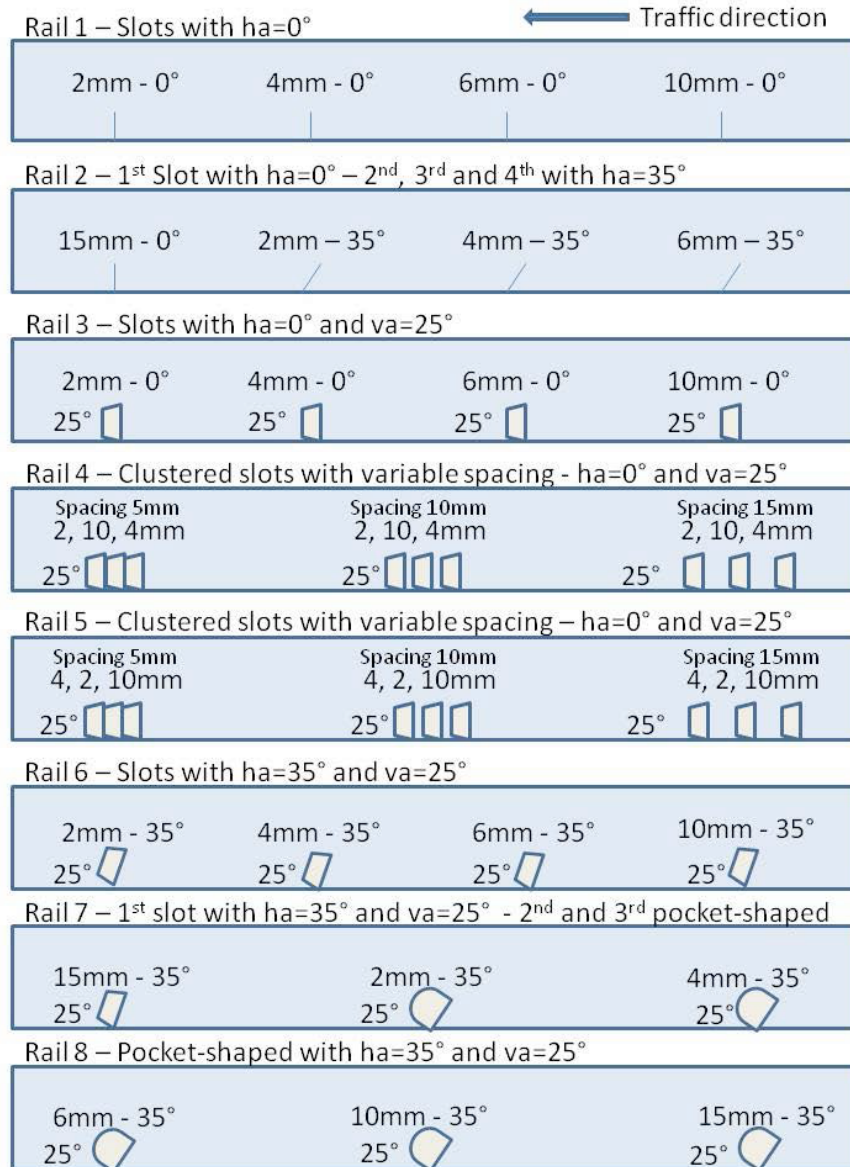


Figure 5.11 Plan view representation of artificially induced defects on rotary rail rig used for the high speed ACFM measurements [56].

Figure 5.12 to Figure 5.14 show the results of high speed ACFM measurements from the rotary rail rig at speeds of 16, 32 and 48 km/h, respectively. It can be observed from the graphs that the experimental data present large variations in the background signal, which is caused by vertical movement of the ACFM probe with respect to the rail during the inspection. This type of lift-off variation is also expected in high-speed survey trains owing to the response of the bogie to track irregularities [135]. This lift-off variation may be alleviated

by mounting the ACFM probe at a location far from the suspension mechanism, where the oscillations are at their lowest.

Figure 5.12 to Figure 5.14 also show the performance of the CTSM algorithm on the high speed ACFM measurements on the rotary rail rig for 16, 32 and 48 km/h, respectively. The results suggest that most defects can be automatically detected with a high QOF (> 90%) using threshold values of 2σ and 0.5σ (a high value is used for high SNR) where the symbol σ denotes the SD of the low-pass filtered ΔB_x signal. It is also evident that signals due to rail gaps produce signatures similar to those of defects and therefore pass the acceptance criterion of the CTSM algorithm. The rail gap signals show a larger signal drop than a typical defect and can be reliably removed from the candidate signals based on their known positions. The value of the threshold relative to the ΔB_x signal contributes a crucial part in the performance of the CTSM algorithm. For inspection data with low lift-off change (e.g. < 3 mm), most of the defect signals can be detected using a high (e.g. 2σ) threshold value (Figure 5.12).

As the speed of inspection increases, so does the vertical movement of the ACFM probe relative to the rail surface that is also accompanied by a reduction in the signal drop over defects (Figure 5.13 and Figure 5.14). This would introduce the risk of missing signatures associated with small signal drops defects that are below the threshold value (i.e. 2σ). Thus, at higher inspection speeds a small threshold (e.g. 0.5σ) is recommended at the cost of picking up extra crack-like signals that may be present in the signal. Nonetheless, this shortcoming may be largely improved by using a low-cost laser sensor as discussed in the previous section.

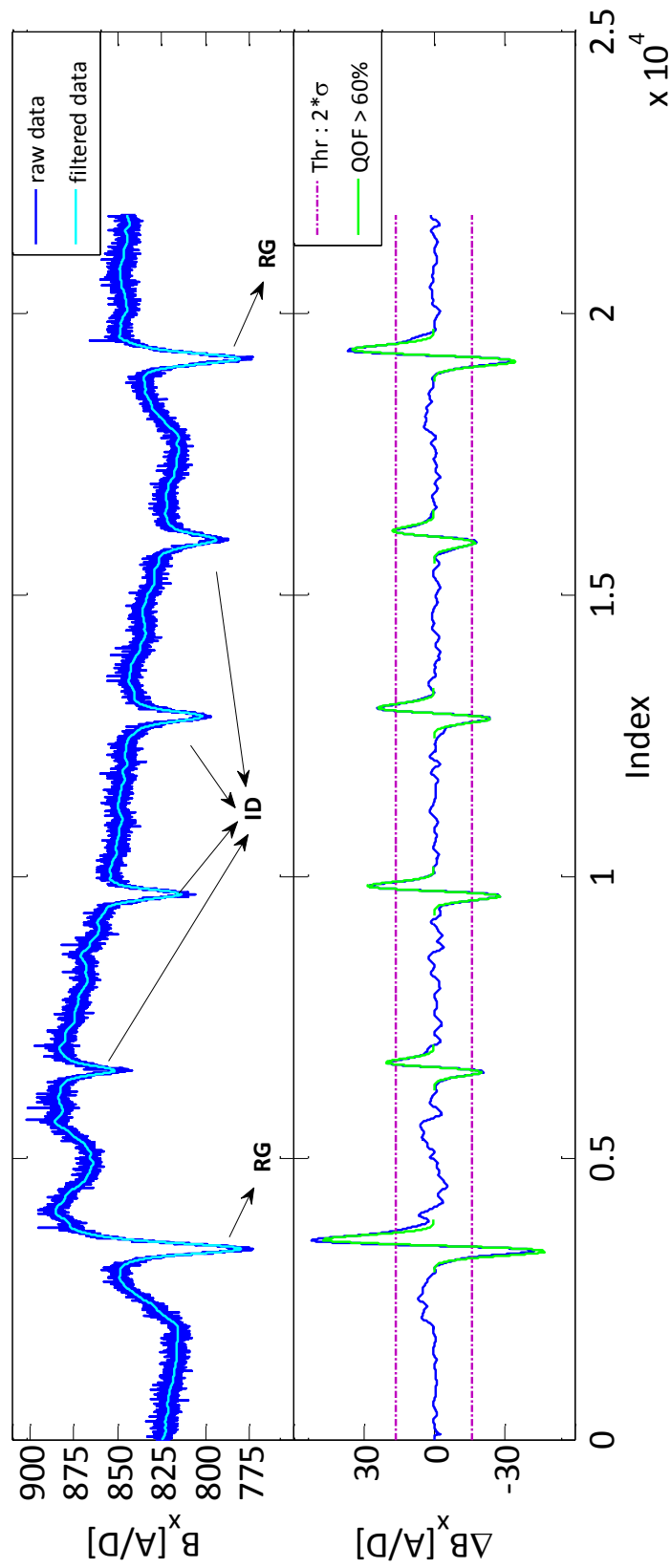


Figure 5.12 Performance of the CTSM algorithm in the detection of artificial defects from high-speed ACFM scans at 16 km/h using a 50 kHz probe. Labels: RG → Rail Gap, ID → Isolated Defect.

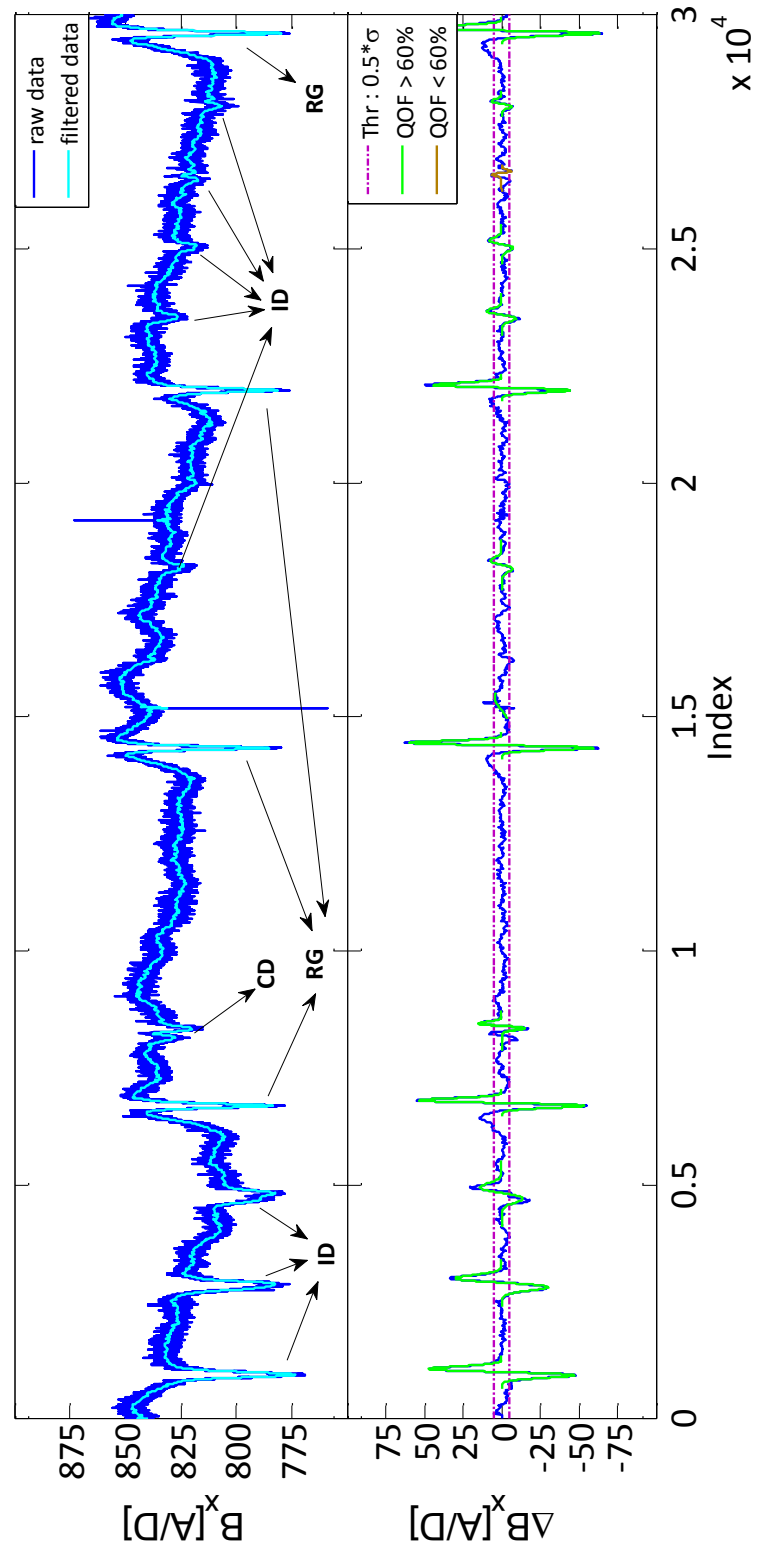


Figure 5.13 Performance of the CTSM algorithm for the detection of artificial defects from high speed ACFM measurements on rotating rail rig at 32 km/h using a 50 kHz probe. Labels: RG → Rail Gap, ID → Isolated Defect, CD → Clustered Defect. Some defects were missed due to excessive lift-off.

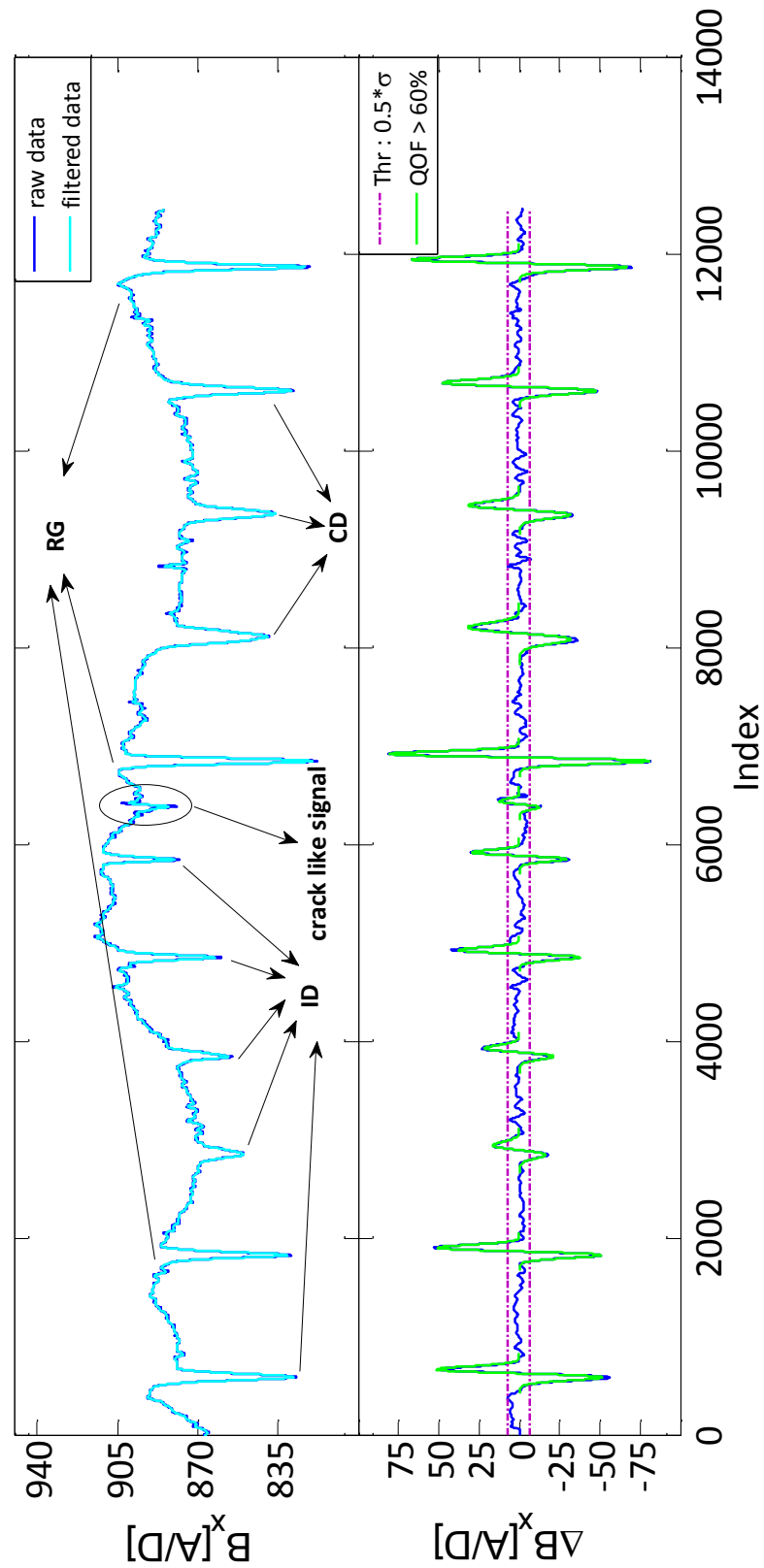


Figure 5.14 Performance of the CTSM algorithm in the detection of artificial defects from high speed ACFM measurements on rotating rail rig at 48 km/h using a 50 kHz probe. Labels: RG → Rail Gap, ID → Isolated Defect, CD → Clustered Defect.

5.4.3. Automatic Characterisation using the Robotic System

The results presented in this section correspond to the field trials on real rail tracks at Long Marston Railway. To study the characterisation scan independently, the known position of the second defect (see Table 5.1) was given to the IUI software. The robotic system was then instructed to move forward at a constant speed and stop in close proximity (within 30 mm) of the second defect, which is located 8.65 m from the datum. The position control mode became active once the absolute position error fell below 1.5 m (this value was determined by try and error; however it has no significance on the accuracy of controller). Figure 5.15 demonstrates the real-time position and speed of the robotic system as recorded by the software until convergence. As can be observed, the robotic system successfully stopped in the vicinity of the defect with a position error of 23 mm. Subsequently, the system was instructed to perform a characterisation scan over the defect. This consists of first a profile measurement, using the laser system, followed by a scan at constant ACFM probe lift-off of 3 mm and orientation angle of 45° with respect to the running direction.

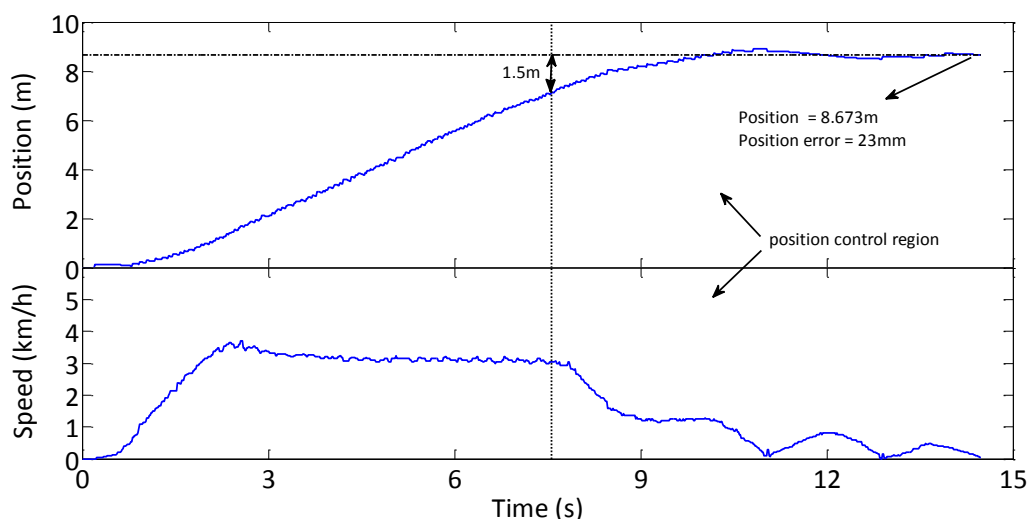


Figure 5.15 The real-time position and velocity plot of the robotic system travelling to the location of the second defect which is 8.65 m relative to the datum.

Figure 5.16a shows the result of a 3D ACFM grid scan over the railhead using the measured profile (Figure 5.16b). The sensor output has been normalised with respect to its background level [136]. The maximum signal reduction scan line has also been compared with COMSOL simulation data for a crack of 1.5 mm depth (details of the COMSOL modelling approach can be found in Nicholson, et al. [3] and is carried out assuming a flat surface rather than the curved rail surface) which shows close agreement (Figure 5.16c). This close agreement indicates that the signal can be used with the sizing information (based on the COMSOL modelling) to give accurate crack sizes. The initial ACFM orientation angle of 45° was chosen to give a 10° angle offset relative to the defect which, if not taken into account, will cause the crack pocket length to be underestimated. Figure 5.16c shows a minimum B_x signal of 98.5% for an angle offset of 10° which suggests an average pocket length of 1.3 mm (i.e. 13.3% error) based on the calibration curve discussed in Chapter 4. When the offset angle is compensated for, the minimum B_x signal is decreased to 97.7% which then suggests an improved average pocket length of 1.6 mm (i.e. 6.7% error). It should be noted that although the underestimation of crack pocket length due to the uncorrected angle offset used here was insignificant, the error would be much higher as the angle offset is further increased. Following the constant lift-off ACFM scan over the measured rail profile, the on-line crack surface angle detection algorithm reported a crack surface angle of 32.5° which, if taken into account, leads to a reduced angle offset of 2.5° . This demonstrates the capability of the developed robotic system to autonomously travel to a desired location and obtain high quality and reliable data on an unknown defect.

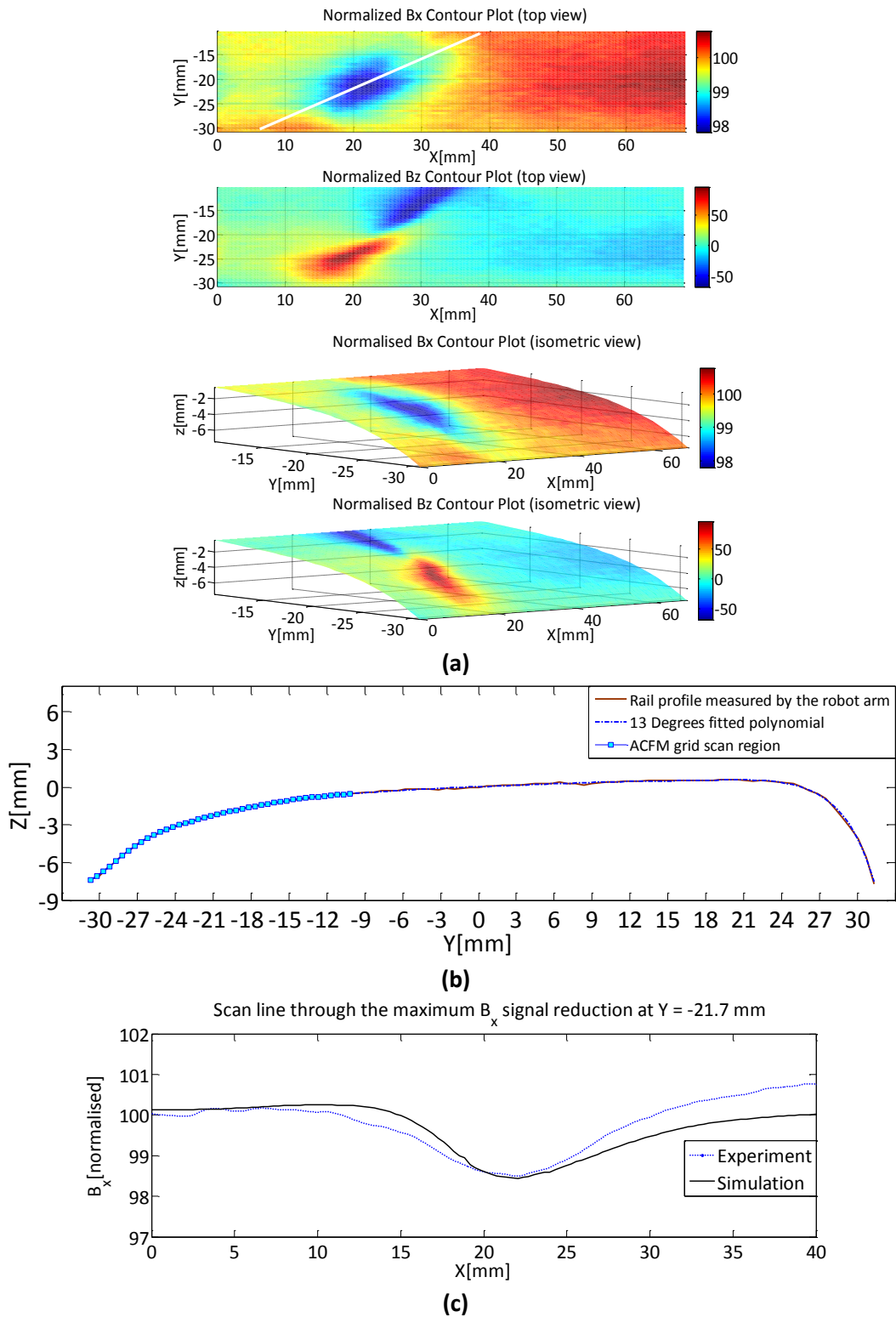


Figure 5.16 (a) The normalised contour plot of automated ACFM scans over the second defect (see Table 5.1) at a constant lift-off of 3 mm and orientation angle of 45° relative to the running direction. The white line shows the crack orientation (32.5°) as calculated by the automatic crack surface angle detection algorithm. (b) The rail profile measured by the robot arm using the laser distance sensor in the vicinity of the second defect. (c) Comparison of the COMSOL simulation and experimental result of the ACFM scan over the second defect at 3 mm lift-off and relative angle offset of 10° .

5.5. Summary

The proposed CTSM algorithm leads to more reliable detection of defects in that they are automatically detected using AI rather than skilled operators. Apart from saving human effort, the main advantage of the algorithm is the ability to detect defects from noisy data in the presence of severe lift-off change where the existing simple threshold method cannot reliably detect defects. This has been confirmed by assessing the performance of the CTSM algorithm on both low speed field trials on real rail tracks using the developed robotic system and also by re-analysing high speed ACFM measurement data (from tests carried out by Papaalias, et al. [56] at the University of Birmingham) using the CTSM algorithm.

The results from the automatic characterisation test also suggest that the robotic system can take reliable and high quality ACFM measurements over an unknown RCF crack which can be used for accurate crack sizing.

Chapter 6. Case Study: Extension of the CTSM Algorithm for Automatic Detection of Multiple-RCF Cracks

6.1. Introduction

This chapter presents the last of three case studies that builds on Chapter 5. It has been demonstrated in the previous chapter that the CTSM algorithm is able to reliably detect isolated RCF cracks automatically. However, the ACFM response to clustered defects, that are more typical of RCF cracks in rails [113], is different to that of an isolated RCF crack (depending on the spacing between individual cracks), as discussed in Chapter 4. This means that the mathematical model developed for an isolated defect would not provide the best fit in the case of multiple-RCF cracks; they would be rejected by the CTSM algorithm due to likely poor QOF contribution, this is demonstrated in the next section.

In this chapter, the CTSM algorithm is extended to overcome this shortcoming. The performance of the extended CTSM algorithm is then evaluated on both simulated and experimental ACFM measurements for several sets of clustered RCF cracks.

6.2. ACFM Response to Multiple-RCF Cracks

Figure 6.1 shows the simulation result of the ACFM response (using a 5 kHz probe at zero lift-off) to four closely spaced RCF cracks (each of surface length 10 mm, pocket length 4 mm and width 0.5 mm) at different crack spacings [113]. It is evident that for a crack spacing of less than 5 mm the individual characteristic troughs are not distinguishable from the B_x

signal owing to the inability of the induced eddy current to flow in between the individual cracks as most of the current density will be concentrated near the crack ends. This is in agreement with the findings from the experimental robotic ACFM measurements over the multiple artificial cracks on the calibration block that has been previously discussed in Chapter 4 (Figure 4.5). In this case, using the signature for an isolated defect with the CTSM algorithm will produce a high QOF and therefore the cracks can be reliably detected.

In contrast, as the crack spacing is increased, the presence of the individual troughs is more pronounced in the B_x signal. Thus, using the signature for an isolated defect will result in a reduced QOF and thus, reduced reliability of crack detection. This is demonstrated in Figure 6.2.

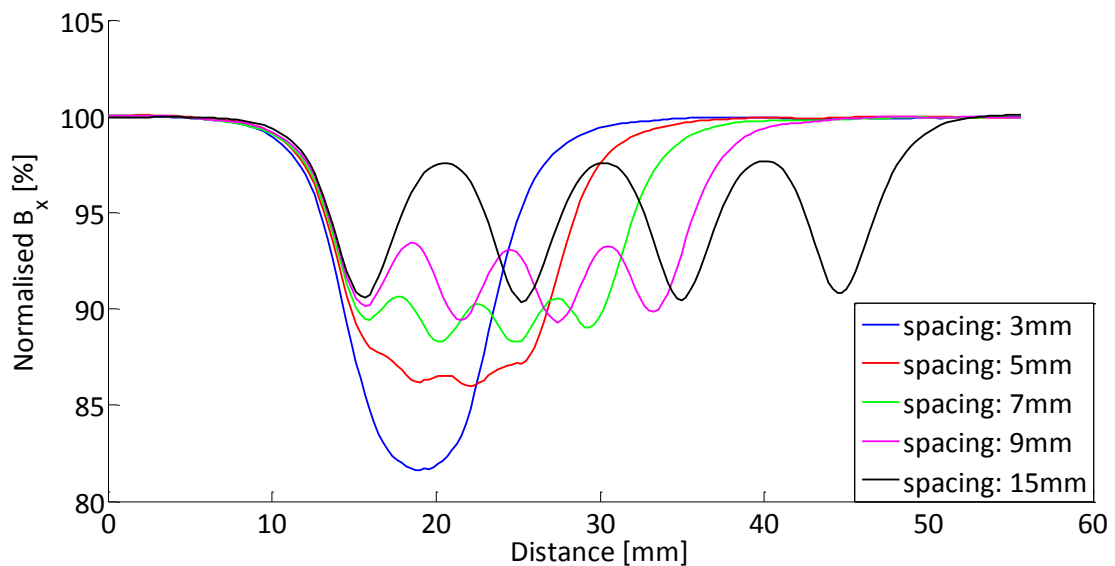


Figure 6.1 COMSOL simulation results of ACFM response to multiple-RCF cracks at different crack spacing using 5 kHz probe at zero lift-off [113].

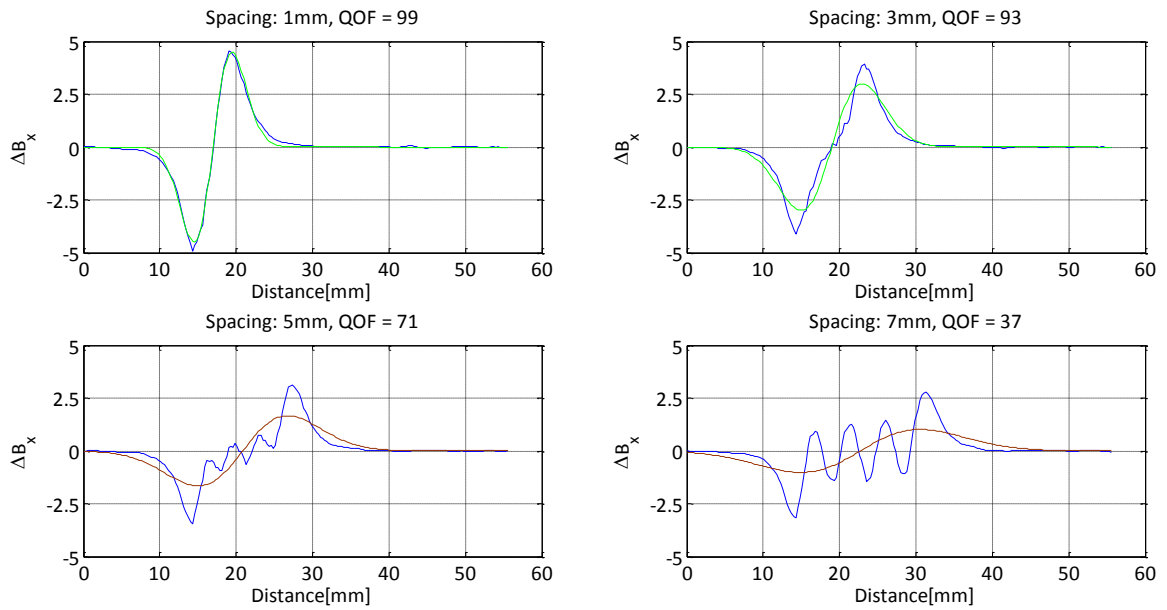


Figure 6.2 Result of CTSM algorithm on the ACFM measurements over multiple-RCF cracks at a range of crack spacings based on an isolated crack signature. In each graph, the blue curve represents the derivative of the normalised B_x signal while the green/brown curve represents the best fit after optimisation.

6.3. Extended CTSM Algorithm

In the extended CTSM algorithm, the signature S which corresponds to the derivative of multiple-RCF crack signal (ΔB_x) is modelled as the derivative of sum of a finite number of Gaussian functions (with positive unknown parameters) corresponding to the individual troughs in the B_x signal (Equation (6.1)). For every trough (local minimum) in the B_x signal there is a zero crossing in the ΔB_x signal where the derivative of the B_x signal is zero (Figure 6.3). Therefore, the number of troughs may be obtained from the zero crossings in the ΔB_x signal. It must be noted that only those zero crossings corresponding to minima should be considered; they can be distinguished from other zero crossings (corresponding to local maxima) using a second-derivative check on the B_x signal. At local minima the signal B_x is convex hence its second derivative is positive. The unknown parameters are then optimised

using the Levenberg-Marquardt method in a least square sense on the basis of minimisation of the cost function J as defined by Equation (5.5).

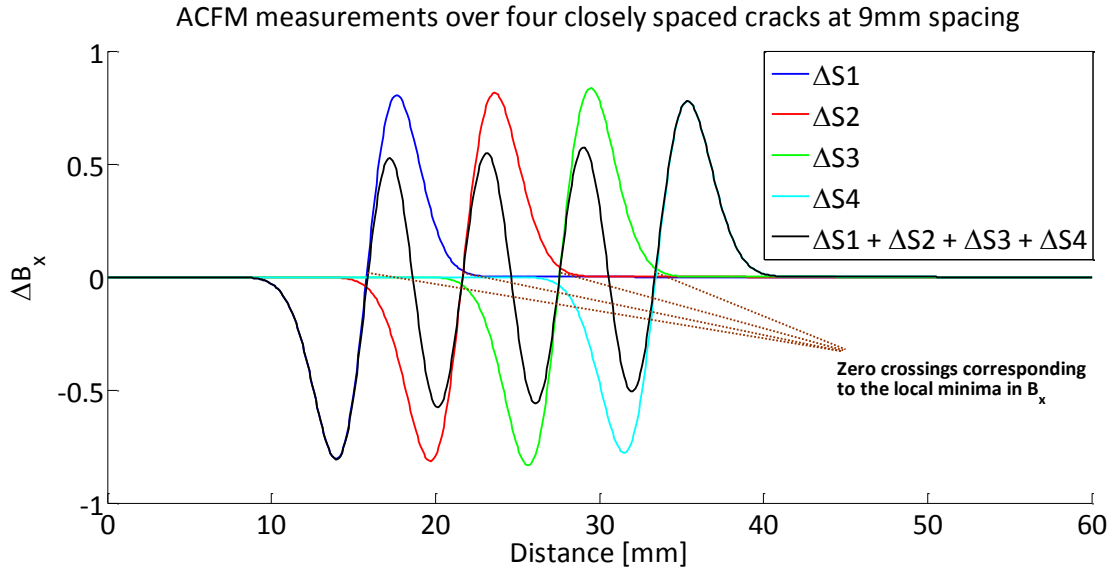


Figure 6.3 Demonstration of the first derivative of the B_x signal and the zero crossings.

$$S(i) = \sum_{j=1}^m a_{0,j} (i - a_{2,j}) e^{-a_{1,j}(i - a_{2,j})^2} \quad (6.1)$$

where $a_{k,j}$'s ($k = 0,1,2$ and $j = 1, \dots, m$) are the positive unknown parameters to be optimised and m is the number of zero crossings corresponding to local minima in the B_x signal. As for the CTSM algorithm, due to the nonlinearity of the signature S (and thus the cost function J), the optimisation algorithm may be trapped in local minima. In order to avoid this phenomenon, the parameters $a_{k,j}$ are initialised near the expected global minimum, as described below. Applying the chain rule, the first derivative of the signature S is given by Equation (6.2).

$$\frac{\partial}{\partial i} S(i) = \sum_{j=1}^m a_{0,j} e^{-a_{1,j}(i - a_{2,j})^2} (1 - 2a_{1,j}(i - a_{2,j})^2) \quad (6.2)$$

Neglecting other terms, at a given zero crossing $i = a_{2,j}$, the first derivative may be approximated as:

$$\frac{\partial}{\partial i} S(i)_{i=a_{2,j}} \cong a_{0,j}$$

Therefore $a_{0,j}$'s may be initialised to the second derivative of the B_x signal at its local minima. The parameters $a_{1,j}$ were found to have a negligible effect on the convergence of the algorithm and therefore may be initialised as positive random numbers. The parameters $a_{2,j}$'s are, however, initialised as the location of zero crossings in the ΔB_x signal where the function is increasing. This is made possible by using a first-order (linear) approximation of the ΔB_x signal near its zero crossing points. The true zero crossings may then be distinguished from others through the slope of the line (at local minima, the slope of the signal ΔB_x is positive). Subsequently, the recognition of multiple-RCF cracks is based on the QOF of the signature S after optimisation (Equation (5.6)).

6.4. Results

6.4.1. Automatic Detection from Simulated ACFM Response to Multiple-RCF Cracks

Figure 6.4 shows the results of using the extended CTSM algorithm with the simulated ACFM signals (generated using the COMSOL model approach) for multiple-RCF cracks of varying spacing. It can be observed that the algorithm has been able to detect most of the RCF crack signals with high reliability (QOF > 90%). However, for the RCF cracks of less than 7 mm spacing, despite the high QOF, the algorithm was unable to recognise all four crack features. This drawback, however, is due to the inability of the ACFM sensor used in this work to detect individual cracks from very closely spaced RCF cracks.

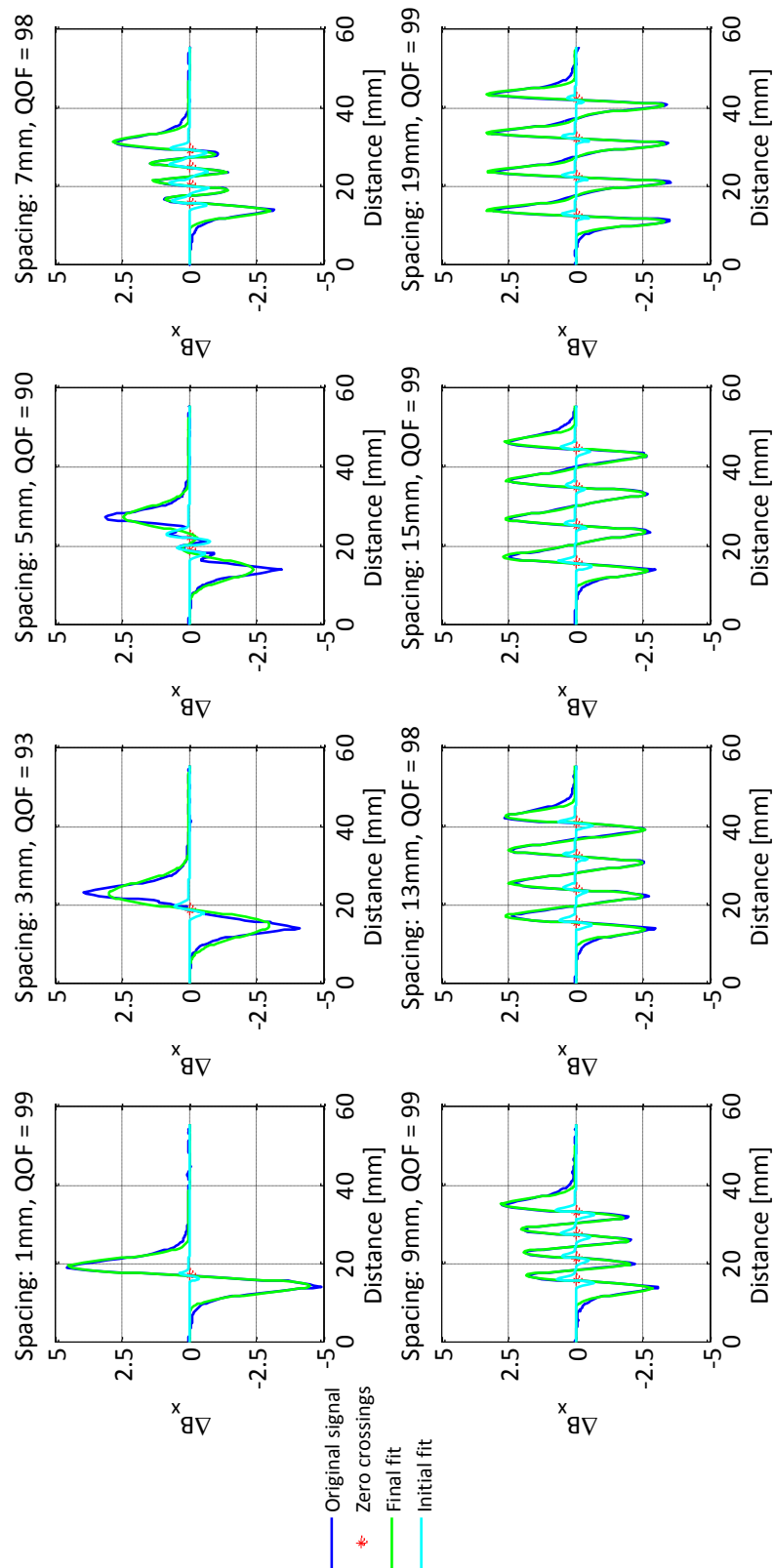


Figure 6.4 Result of using the extended CTSM algorithm on simulated ACFM responses to multiple-RCF cracks of varying spacing.

6.4.1.1. Performance Evaluation on Noisy Measurements

In order to assess the robustness of the extended CTSM algorithm, the ACFM measurements were superposed by additive white Gaussian noise at a range of SNRs. The data was then low-pass filtered using a fixed normalised cut-off frequency (independent of the noise) of 0.28 in each case to smooth the data. It should be emphasised that, in the case of experimental measurements, the use of low-pass filtering is essential for the CTSM algorithm in that it uses the derivative signal (ΔB_x) for the optimisation which is very sensitive to high frequency harmonics in the B_x signal.

The results for SNRs of 10 and 5 dB are shown in Figure 6.5 and Figure 6.6, respectively. These values were found to be adequate enough (i.e. qualitatively) to model the noise observed during the field trials, however, the exact value of the SNR has not been considered here as this demands the knowledge about the source of the noise which is difficult to obtain. It can be seen from the graphs that the extended CTSM algorithm can detect the multiple-RCF crack signals with high QOF even in the case of noisy data.

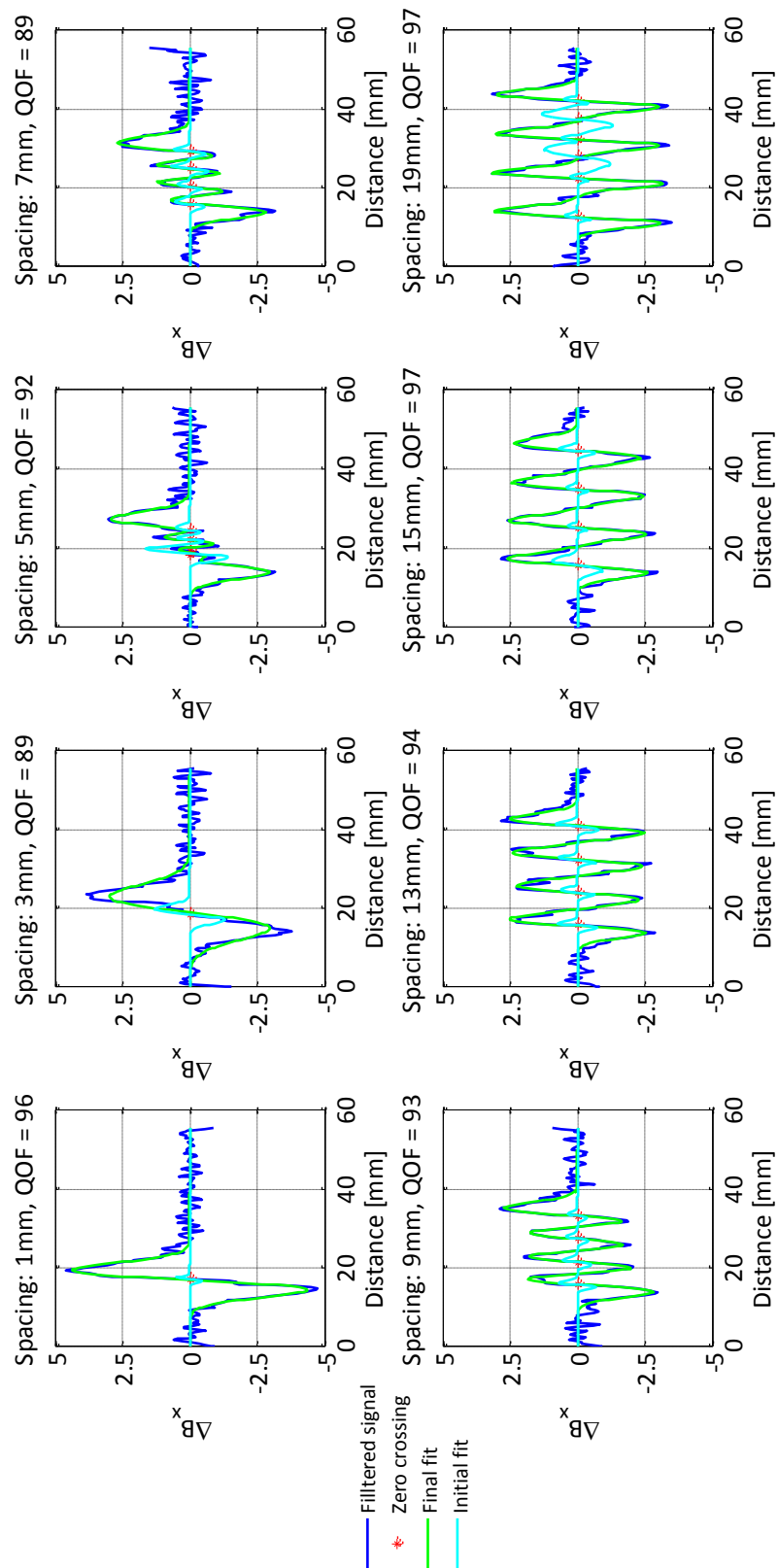


Figure 6.5 Result of the extended CTSM algorithm for the simulated ACFM response to multiple-RCF cracks of varying spacing. The data were superposed by additive white Gaussian noise of SNR of 10 dB.

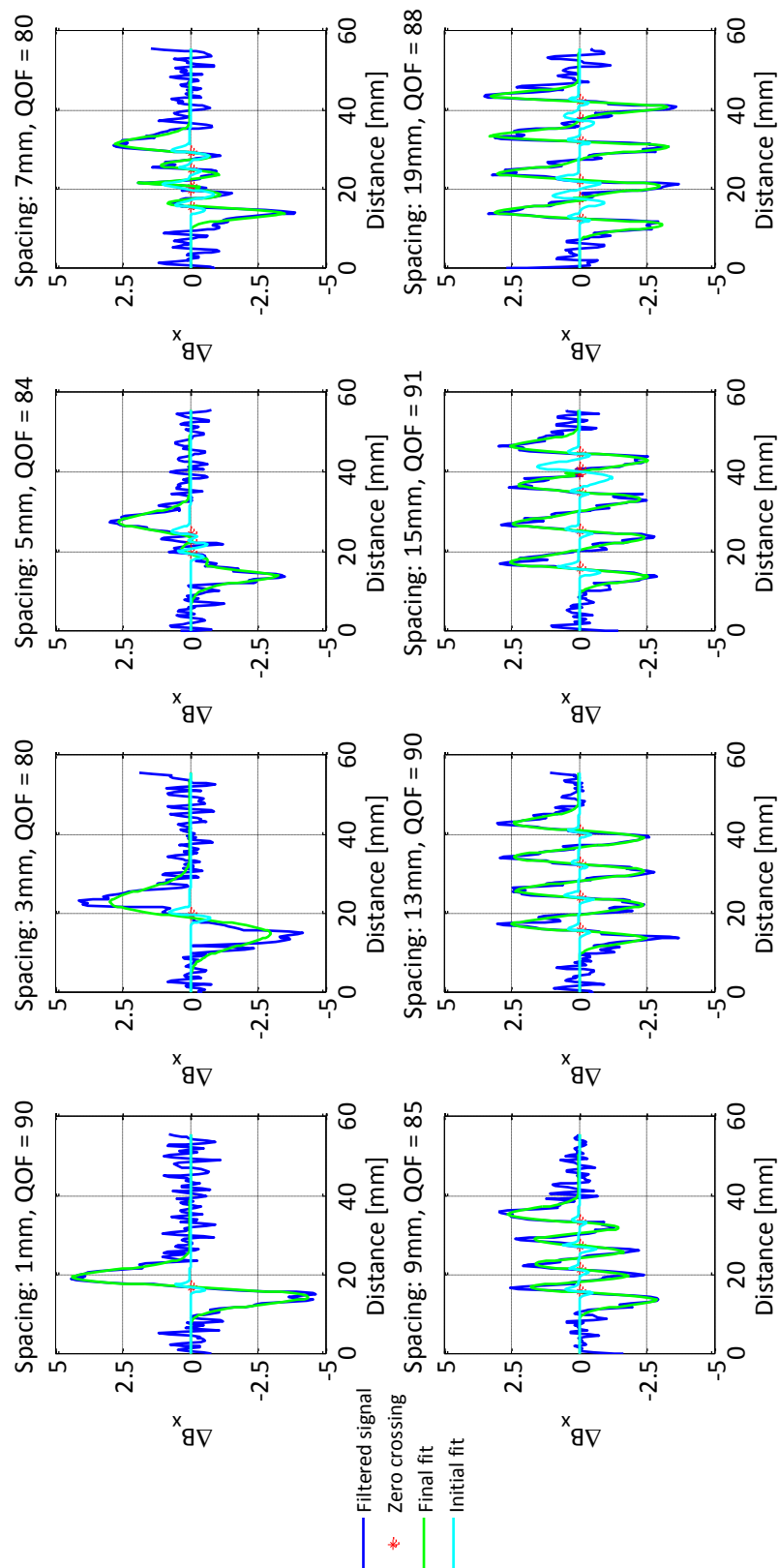


Figure 6.6 Result of the extended CTSM algorithm for the simulated ACFM response to multiple-RCF cracks of varying spacing. The data were superposed by additive white Gaussian noise of SNR of 5 dB.

6.4.2. Automatic Detection from Experimental ACFM Response to Multiple-RCF Cracks








To further examine the reliability of the extended CTSM algorithm, it has been applied to the experimental ACFM signals taken from real RCF cracks. Seven rail samples taken from in-service rails containing a number of RCF cracks at a range of spacings and surface angles were used. Detailed explanations of the RCF cracks are given in Table 6.1.

Using the robot arm and the laser sensor, the rail samples' profiles were measured. The angles of the cracks in the clusters were manually recorded and the average value used as the initial ACFM probe angle. Subsequently, a number of ACFM grid scans at a constant lift-off of 2 mm and matching probe angle following the rail profile were taken. In each case, the scan data corresponding to the maximum reduction in B_x signal were extracted from the grid scan lines and plotted against the distance along the rail length. The trailing and leading portions of the B_x signal were ignored due to edge effects from the ends of the rails. The results are shown in Figure 6.7. It can be observed that the waveforms corresponding to the experimental data show a similar pattern as the simulation results (individual troughs corresponding to the defects).

The experimental data were then examined blindly using the extended CTSM algorithm with neither any prior knowledge about the number of cracks nor the spacing between them. The results are shown in Figure 6.8; the graphs confirm that the algorithm can automatically detect the multiple-RCF crack signatures from the experimental data with high QOF (> 90%) for most of the rail samples. However, for rail sample 2, the result shows a slightly lower, yet high enough, QOF (76%) owing to reduced B_x signal drop over the cluster of defects, compared to other rail samples (Figure 6.7). In other words, for smaller RCF crack size (based on surface length) the reduced signal drop (hence SNR) leads to a reduction of the QOF. It

should be noted that, as for some rail samples the spacing between the cracks in cluster varied, the number of real cracks may be more than the number of troughs observed in the B_x signal. For example, for rail sample 1, three defects were identified by the CTSM algorithm and this corresponds to visual observation of five cracks where two cracks were in a closely spaced cluster (spacing < 5 mm).

Table 6.1 The rail samples taken from in-service rails containing a number of real RCF cracks at a range of spacings and surface angles. The rail profiles were measured prior to ACFM grid scans.

Name	Condition	
Rail 1	<i>Contains five light multiple-RCF cracks at an average crack surface angle of 35° and 5-15 mm spacing. It also contains five isolated RCF cracks.</i>	
Rail 2	<i>Contains three light multiple-RCF cracks at 5-10 mm spacing at an average crack surface angle of 90°.</i>	
Rail 3	<i>Contains five light-moderate multiple-RCF cracks at 3-10 mm spacing at an average crack surface angle of 31°. It also contains four isolated RCF cracks.</i>	
Rail 4	<i>Contains three multiple-RCF cracks at 2-10mm spacing at an average crack surface angle of 36°.</i>	
Rail 5	<i>Contains three moderate multiple-RCF cracks at 10-15 mm spacing at an average crack surface angle of 30°. It also contains one isolated RCF crack.</i>	
Rail 6	<i>Contains two multiple-RCF cracks at 15-20 mm spacing at an average crack surface angle of 33°. It also contains four isolated RCF cracks.</i>	
Rail 7	<i>Contains four heavy-severe multiple-RCF cracks at 2-15 mm spacing at an average crack surface angle of 17°. It also contains four isolated RCF cracks.</i>	

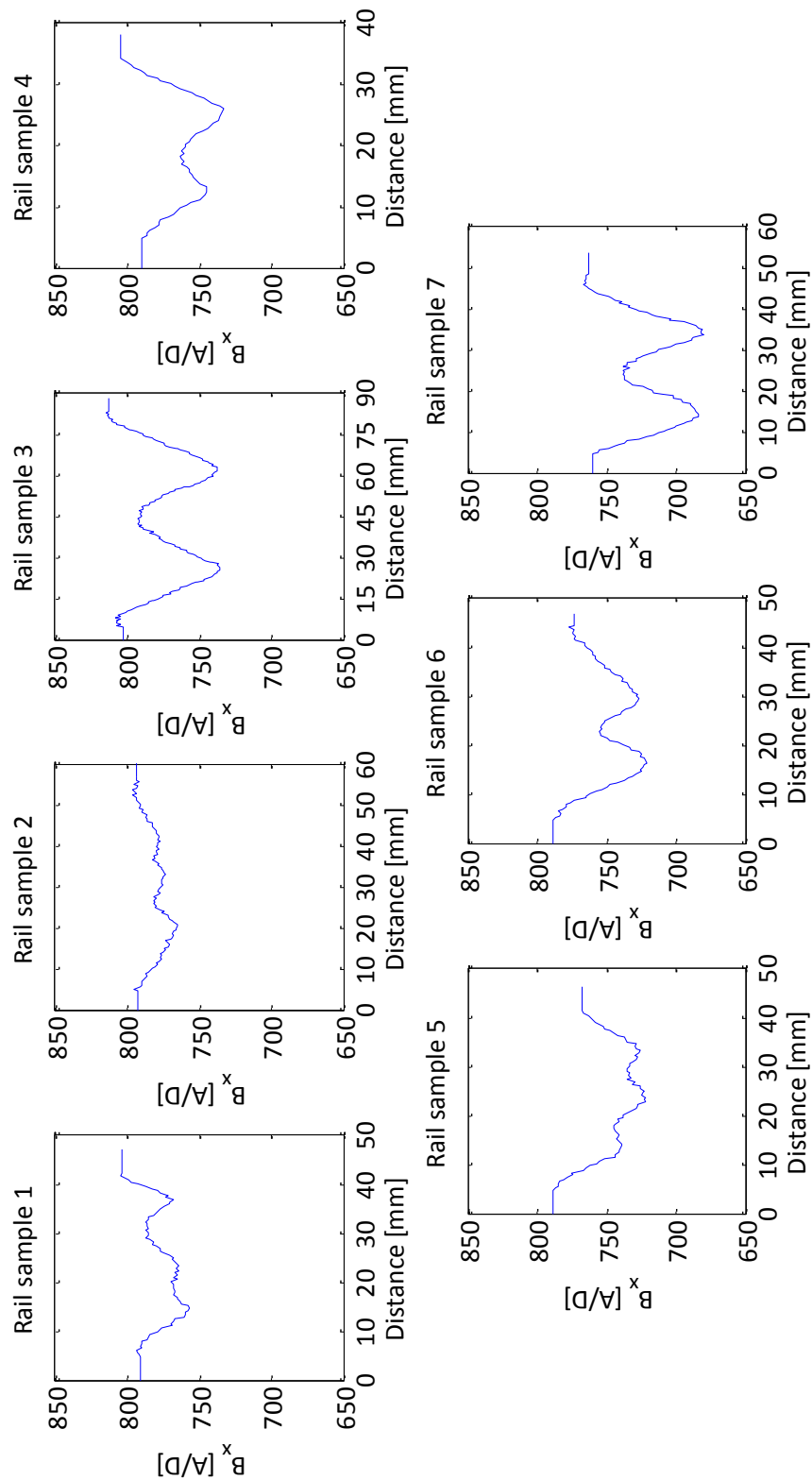


Figure 6.7 Results of the robotic ACFM measurements over rail samples 1-7 at constant lift-off of 2 mm and matching probe angle. The data shown correspond to scan lines where the B_x signal reduction is a maximum. Only the portion of the scan lines containing multiple-RCF crack signatures have been used for the analysis.

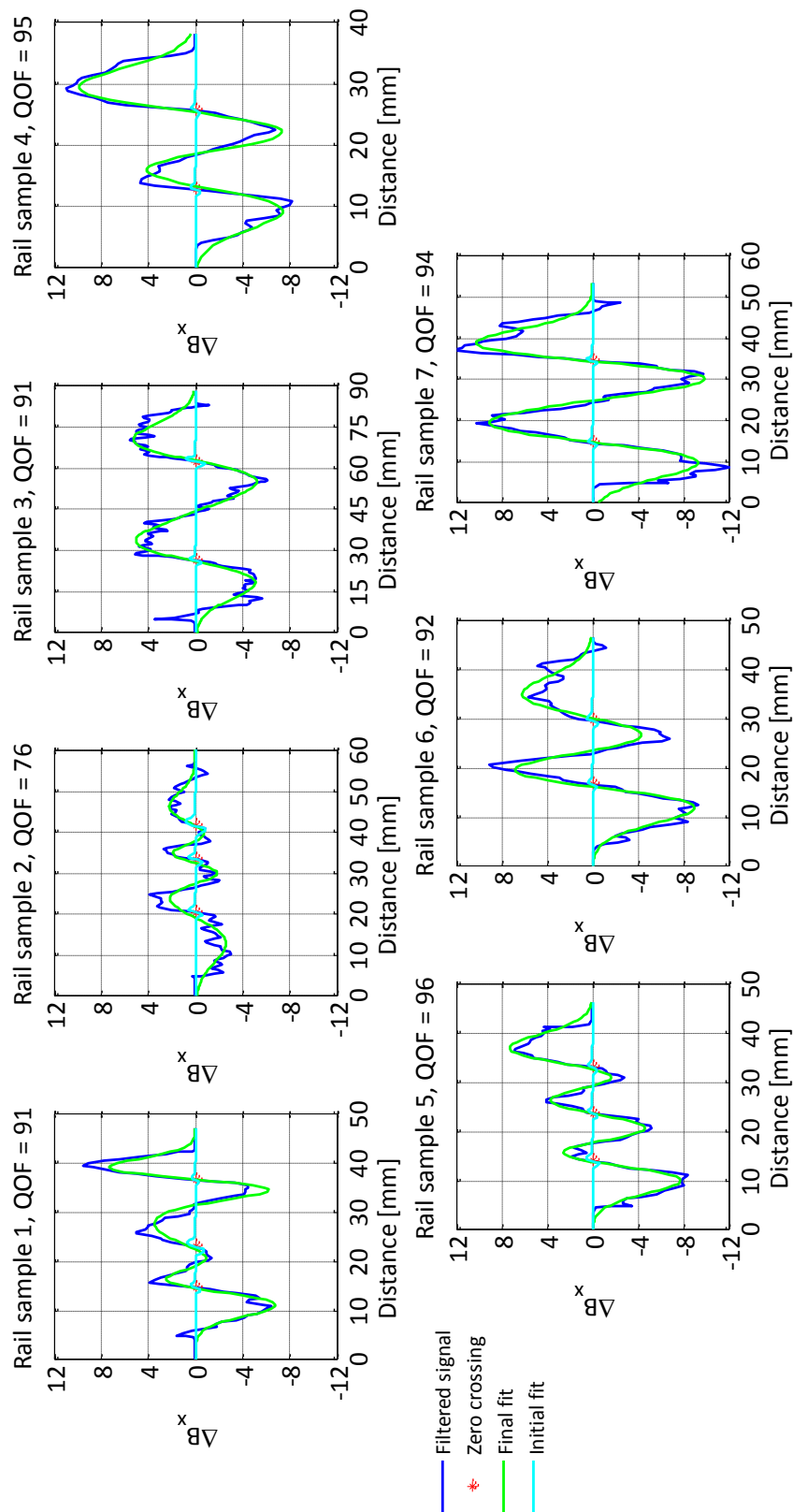


Figure 6.8 Result of the extended CTSM algorithm on robotic ACFM measurements over rail samples 1-7 at constant lift-off of 2 mm and matching probe angle. In each graph, the data shown correspond to the scan line where the B_x signal reduction is a maximum.

6.5. Summary

In this chapter the robustness of the CTSM algorithm for detection of multiple-RCF cracks has been studied. It was shown that the signals associated with multiple-RCF cracks may be rejected by the CTSM algorithm due to poor QOF contribution.

To circumvent this drawback, an extension of the CTSM algorithm has been proposed whereby the multiple-RCF crack signature is modelled as the sum of a finite number of isolated RCF crack signatures where the number of cracks in a cluster can be distinguished by the number of zero crossings associated with the derivative of the B_x signal.

Consequently, the result of the extended CTSM algorithm on both experimental and simulation results of ACFM response to multiple-RCF cracks has been considered. It was shown that the extended algorithm can automatically detect the multiple-RCF crack signatures by high QOF (> 90% for most of defects) even in the presence of lift-off change and noise, however, the number of defects in a cluster could be misidentified when the defects are too close (spacing < 5 mm). This difficulty is owing to the inability of the ACFM technique rather than the algorithm and has been previously reported in the literature [113].

Therefore, it can be concluded that the detection of both isolated and multiple-RCF cracks can be performed by the extended CTSM algorithm which subsequently suggests that the detection and characterisation of RCF cracks may be performed as one continuous process where the human interaction is largely minimised.

Chapter 7. Conclusions and Future Work

7.1. Conclusions

This thesis presents a methodology on how AI and robotic NDT are combined together to minimise the inefficiencies and enhance the speed, reliability and accuracy of manual inspection of RCF cracks in rails by the ACFM technique. Particularly, using AI based on a conventional RBES architecture along with robotics, an autonomous inspection trolley has been developed to accurately and reliably detect and size the RCF cracks. This work was in line with an industrial need identified by the rail industry and has been supported by the European FP7 INTERAIL project.

In this chapter, the key findings of the developed robotic system based on three case studies presented in chapters 4, 5 and 6 are reviewed, giving details of its strength and limitations. Subsequently, the future path of this research and also recommendations for further work in terms of both software and hardware enhancements are outlined.

7.2. Achievements and Key Findings

7.2.1. Case Study 1

In this case study the challenge introduced to the robotic system is of sizing an unknown RCF crack in a rail which may be subject to an unpredicted level of wear. Solutions have been proposed and applied to tackle these challenges. These are summarised as the following:

7.2.1.1. Uncertainties due to Rail Misalignment and Lift-off Change

While the inspection trolley travels towards the location of an RCF crack for detailed characterisation, the robot arm may experience misalignment with respect to the rail either due to likely hunting of the trolley or due to the physical misalignment of the rails at the joints (assuming the defect is located near the joint). This could result in sizing inaccuracies, if not taken into account. Using a laser distance sensor and robot arm, a two-point based calibration method was proposed and implemented in the IUI that can automatically re-align the robot arm end-effector (the ACFM probe) along the rail track (see section 3.4.1).

Similarly, the ACFM probe lift-off change due to unpredicted wear of rail could significantly lessen the sizing accuracy depending on its severity. This shortcoming was addressed by a non-contact rail profile measurement (followed by calibration of alignment) prior to the characterisation process. The results were validated against the existing “MiniProf” systems (see section 3.4.2).

7.2.1.2. Uncertainties due to Unknown RCF Crack

Study of the ACFM response to RCF cracks at non-matching probe angles has revealed that for angle offsets beyond 10° the reduced B_x signal drop causes significant sizing inaccuracy, if not taken into account [65]. This intensifies the need for measuring the RCF crack surface angle so that the sizing scan along the crack opening is performed at close to the optimum condition (i.e. the induced eddy current flows normal to the crack opening). Based on the results of both experiments using the robot arm and simulation of 2D ACFM grid scans over RCF cracks at a range of non-matching probe angles representing typical deviations of real RCF crack surface angles from its average value (see section 4.3.2), it was demonstrated that

the crack surface angle may be closely approximated within 10° by finding the crack ends based on the location of peaks in the B_x scan lines. This was facilitated by a fast searching algorithm implemented in the IUI. The effect of grid spacing and probe lift-off on accuracy of the searching algorithm was also quantified (see sections 4.3.3 and 4.3.4).

The results of the searching algorithm exhibited a dependency between the minimum grid spacing and the crack surface length. Using 0.5 mm grid spacing, the characterisation scan over a single crack takes approximately 240 s. An initial guess for the crack surface length may help choose the optimum grid spacing which results in reduced characterisation time; this may be achieved by approximating the surface length based on the initial detection results obtained using the ACFM array sensors.

7.2.2. Case Study 2

In this case study, the performance of the robotic system for both detection and characterisation of RCF cracks based on a number of field trials carried out at Long Marston Railway line was investigated. These are summarised in the following sub-sections.

7.2.2.1. Automatic Detection

For the detection test, the robotic system was configured to inspect the rails containing a series of artificial cracks, at walking speed. The data collected were initially post-processed offline using the simple threshold method to automatically find the defects. It was found that due to variable B_x background signal owing to ACFM probe lift-off change (> 2 mm) during the motion of the trolley, some defect signals went undetected. Besides, many false indications were generated. This type of lift-off variations was also observed in the case of high speed ACFM data [54, 56] and is also expected in the case of real rail inspection due to significant (up to 6 mm) vertical displacement caused by bogie dynamics [135].

The CTSM algorithm has been proposed to alleviate this shortcoming by computing the differential of the B_x signal (ΔB_x) with respect to its local background resulting in a stable background for the ΔB_x signal (approximately near zero) and hence, the defects can be detected by an appropriate threshold value. Further, the CS are examined by a non-linear curve fitting algorithm finding the best match of an isolated RCF crack signature to the CS by a non-linear optimisation method (see section 5.2).

It was shown that this method was effective in both detecting the defects and also greatly reducing the number of false indications as they possessed poor QOF contributions. The algorithm also revealed high detectability (i.e. QOF $> 90\%$) on high speed ACFM measurements carried out previously at the University of Birmingham [54, 56]. The effect of different threshold value for QOF in acceptance of the candidate signals has been also studied.

During the field trials, a number of crack-like signals developed due to sudden up-down vertical movement of the probe and passed the acceptance criteria of the CTSM algorithm.

This problem can be addressed by simultaneously recording the ACFM probe's lift-off by a laser sensor; the crack-like signals are associated with short wavelength laser signals and can be therefore distinguished from the real crack signals. It was also evident that a number of real crack signals were missed due to hunting of the trolley; this can be avoided by using ACFM array sensors surveying wider area of the rail head which offer superior performance than the single probe sensor used in this research.

7.2.2.2. Automatic Characterisation

The process of automatic characterisation involves travelling of the trolley to a defect location and deploying the robot arm to collect high quality data over the defect for accurate sizing. To evaluate this functionality independently, the location of a specific crack having a surface angle of 35° with respect to the rail length were given to the robotic system while the initial ACFM probe angle was intentionally set at 45° to mimic the uncertainty due to unknown RCF crack. The position signal recorded in the IUI during the motion of the trolley showed that the robotic system successfully stopped in the vicinity of the defect with an error of 23 mm which was then compensated for by the robot arm.

Following an automatic calibration of alignment and rail profile measurement, a series of constant lift-off 3D ACFM grid scans over the defective region were initiated. Subsequently, the searching algorithm reported an approximated crack surface angle of 32.5° which verifies the ability of the robotic system in correcting the ACFM probe's initial angle for an unknown RCF crack.

Moreover, the scan line corresponding to the maximum B_x signal reduction was compared with that of a COMSOL simulation of ACFM response to the crack used in the experiment. A

close agreement was found between both data demonstrating the capability of the robotic system in automatically collecting high quality data over an unknown RCF crack that can be later used to accurately size it.

7.2.3. Case Study 3

In this case study, an extension of the CTSM algorithm has been proposed to deal with clustered defects (that are more typical of real RCF cracks) which may generate a different ACFM response than that of an isolated RCF crack, depending on the crack spacings in the cluster. For crack spacing < 5 mm the signal resembles that of a wide isolated RCF crack which showed to pass the acceptance criteria of the initial CTSM algorithm. Conversely, for wider spacings, the ACFM response showed to be different as the signal contains multiple troughs that are associated with the cracks in the cluster. In this case, the crack signals failed the acceptance criteria due to poor QOF contributions as the crack spacing increased.

To overcome this drawback, in the extended CTSM algorithm, the multiple-RCF crack signature has been modelled as sum of finite number of isolated RCF cracks where the number of cracks in the cluster equals to the number of zero crossings in the ΔB_x signal (derivative signal). Similarly, the best match to the candidate signal is obtained using the non-linear optimisation method as discussed in section 5.2. The extended CTSM algorithm was then evaluated on several simulated and experimental ACFM response to multiple-RCF cracks.

In the case of simulations, ACFM responses to four closely spaced semi-elliptical RCF cracks of varying spacing were used. The results showed a high QOF ($> 80\%$) in the case of low SNR

(i.e. 5 dB) while a better QOF (> 89%) were achieved when a higher SNR (i.e. 10 dB) was used.

In the case of real experimental measurements, constant lift-off ACFM measurements over a number of samples taken from in-service rails containing a number of multiple-RCF cracks (including light, moderate and severe cracks) were considered. The results also showed a high QOF (> 90%) for most of the samples. However, one of the samples which contained smaller RCF cracks (less deep), a lower, yet high enough, QOF (76%) owing to reduced B_x signal drop over the cluster of defects, was obtained.

These results recommend that the extended CTSM algorithm has potential to automate the detection of RCF cracks from the ACFM measurements; hence, in inspection of rails for RCF cracks, the detection and characterisation may be performed as one continuous process.

7.3. Future Work and Recommendations

The future path of this research may be continued in certain ways to improve on the limitations reported earlier. These are divided into hardware and software enhancements summarised as the following:

7.3.1. Hardware Enhancements

In this research some of the components used in the developed robotic system were to facilitate the experiments and not necessarily fit for purpose. For instance, the commercial trolley used is primarily designed for manual operation at walking speed and may not function correctly over curves or at crossings. Similarly, the robot arm used is a general purpose robot and can be replaced by a customised robot specifically designed for the rail

inspection which demands less work space and payload characteristics resulting in a more compact and light-weight unit. This also makes it worthwhile to be used for real rail inspection.

It is also suggested that a high speed ACFM array sensor be used for detection of defects (this could be fixed as in the walking stick ACFM systems) while a low-speed single probe sensor be integrated to the customised robotic unit for detailed characterisation.

A secondary laser sensor for monitoring the ACFM probe's lift-off during the detection process is highly recommended to reduce false crack-like signals as discussed previously. This would require less accuracy (e.g. 0.5 mm) than that of profile measurements and may be achieved by a cheaper laser sensor attached to field side of the ACFM array sensor.

7.3.2. Software Enhancements

The IUI may be reprogrammed (redesigned) to allow running on customised high-performance hardware in the loop (HIL) platforms. This helps increase its overall efficiency and reduce the latency caused by running in non-real-time operating systems.

Future research may also include sophisticated signal processing of multiple-RCF crack signals for accurate characterisation. Recent modelling work at the University of Birmingham showed that sizing of multiple-RCF cracks based on the signal of an isolated RCF crack results in overestimation of pocket length [113], depending on the crack spacing. This inaccuracy may be possibly enhanced by training an ANN so as to estimate the correction factor needed for the B_x signal drops corresponding to the individual cracks in the cluster enabling their accurate sizing based on the existing calibration curve used for sizing of isolated RCF cracks.

References

- [1] M. P. Papaelias, C. Roberts, and C. L. Davis, "A review on non-destructive evaluation of rails: state-of-the-art and future development," *Proceedings of the Institution of Mechanical Engineers, Part F: Journal of Rail and Rapid Transit*, vol. 222, pp. 367-384, 2008.
- [2] D. F. Cannon, K. O. Edel, S. L. Grassie, and K. Sawley, "Rail defects: An overview," *Fatigue and Fracture of Engineering Materials and Structures*, vol. 26, pp. 865-886, 2003.
- [3] G. L. Nicholson and C. L. Davis, "Modelling of the response of an ACFM sensor to rail and rail wheel RCF cracks," *NDT & E International*, vol. 46, pp. 107-114, 2012.
- [4] S. L. Grassie, "Rolling contact fatigue on the British railway system: treatment," *Wear*, vol. 258, pp. 1310-1318, 2005.
- [5] R. Spoors, "Railway Group Standard," Safety & Standards Directorate, Railtrack PLC GC/RT5019, 1998.
- [6] D. Topp and M. Smith, "Application of the ACFM inspection method to rail and rail vehicles," *Insight - Non-Destructive Testing and Condition Monitoring*, vol. 47, pp. 354-357, 2005.
- [7] R. Clark, "Rail flaw detection: overview and needs for future developments," *NDT & E International*, vol. 37, pp. 111-118, 2004.
- [8] H. Grohmann, K. Hempelmann, and A. Groß-Thebing, "A new type of RCF, experimental investigations and theoretical modelling," *Wear*, vol. 253, pp. 67-74, 2002.
- [9] J. E. Garnham, D. I. Fletcher, C. L. Davis, and F. J. Franklin, "Visualization and modelling to understand rail rolling contact fatigue cracks in three dimensions," *Proceedings of the Institution of Mechanical Engineers, Part F: Journal of Rail and Rapid Transit*, vol. 225, pp. 165-178, 2011.
- [10] W. Zhong, J. Hu, Z. Li, Q. Liu, and Z. Zhou, "A study of rolling contact fatigue crack growth in U75V and U71Mn rails," *Wear*, vol. 271, pp. 388-392, 2011.
- [11] M. P. Papaelias, C. Roberts, C. L. Davis, M. Lugg, and M. Smith, "Detection and quantification of rail contact fatigue cracks in rails using ACFM technology," *Insight - Non-Destructive Testing and Condition Monitoring*, vol. 50, pp. 364-368, 2008.

- [12] Railtrack, "Permanent Way Special Instruction No. 4, Issue 2," ed, 2002.
- [13] S. Grassie, "Squats and squat-type defects in rails: the understanding to date," *Proceedings of the Institution of Mechanical Engineers, Part F: Journal of Rail and Rapid Transit*, vol. 226, pp. 235-242, 2012.
- [14] C. Mair and S. Fararooy, "Practice and potential of computer vision for railways," in *Condition Monitoring for Rail Transport Systems (Ref. No. 1998/501)*, IEE Seminar on, 1998, pp. 10/1-10/3.
- [15] F. Marino, A. Distanto, M. Nitti, and E. Stella, "A real-time visual inspection system for railway maintenance: Automatic rail detection and tracking," *Politecnico di Bari, Italy, Intern. Rep. DEE*, 2005.
- [16] E. Stella, P. Mazzeo, M. Nitti, G. Cicirelli, A. Distanto, and T. D'Orazio, "Visual recognition of missing fastening elements for railroad maintenance," in *Intelligent Transportation Systems, 2002. Proceedings. The IEEE 5th International Conference on*, 2002, pp. 94-99.
- [17] P. L. Mazzeo, M. Nitti, E. Stella, and A. Distanto, "Visual recognition of fastening bolts for railroad maintenance," *Pattern Recognition Letters*, vol. 25, pp. 669-677, 2004.
- [18] L. Qingyong and R. Shengwei, "A Real-Time Visual Inspection System for Discrete Surface Defects of Rail Heads," *Instrumentation and Measurement, IEEE Transactions on*, vol. 61, pp. 2189-2199, 2012.
- [19] M. Singh, S. Singh, J. Jaiswal, and J. Hempshall, "Autonomous Rail Track Inspection using Vision Based System," in *Computational Intelligence for Homeland Security and Personal Safety, Proceedings of the 2006 IEEE International Conference on*, 2006, pp. 56-59.
- [20] Y. Li, C. Otto, N. Haas, Y. Fujiki, and S. Pankanti, "Component-based track inspection using machine-vision technology," presented at the Proceedings of the 1st ACM International Conference on Multimedia Retrieval, Trento, Italy, 2011.
- [21] W. Boyes, "Instrumentation Reference Book (3rd Edition)," ed: Elsevier, 2003, pp. 566-595.
- [22] S. Peter and T. Bernard, "Ultrasound," in *Nondestructive Evaluation*, ed: CRC Press, 2002.
- [23] D. E. Bray, "Detection of flaws in used railroad rail by ultrasonic inspection techniques," *NDT International*, vol. 12, pp. 217-223, 1979.

- [24] K. Sridhar, "Theory and Applications of Laser-Ultrasonic Techniques," in *Ultrasonic Nondestructive Evaluation*, ed: CRC Press, 2003.
- [25] S. Kenderian, B. B. Djordjevic, D. Cerniglia, and G. Garcia, "Dynamic railroad inspection using the laser-air hybrid ultrasonic technique," *Insight - Non-Destructive Testing and Condition Monitoring*, vol. 48, pp. 336-341, 2006.
- [26] X. E. Gros, "NDT Data Fusion," ed: Elsevier, 1997, pp. 59-66.
- [27] S. Dixon, R. Edwards, and X. Jian, "Inspection of rail track head surfaces using electromagnetic acoustic transducers (EMATs)," *Insight-Non-Destructive Testing and Condition Monitoring*, vol. 46, pp. 326-330, 2004.
- [28] J. L. Rose, M. J. Avioli, P. Mudge, and R. Sanderson, "Guided wave inspection potential of defects in rail," *NDT & E International*, vol. 37, pp. 153-161, 2004.
- [29] J. Rose, M. Avioli, and W. Song, "Application and potential of guided wave rail inspection," *Insight*, vol. 44, pp. 353-358, 2002.
- [30] R. S. Edwards, C. Holmes, Y. Fan, M. Papaelias, S. Dixon, C. L. Davis, B. W. Drinkwater, and C. Roberts, "Ultrasonic detection of surface-breaking railhead defects," *Insight - Non-Destructive Testing and Condition Monitoring*, vol. 50, pp. 369-373, 2008.
- [31] P. Cawley, P. Wilcox, D. Alleyne, B. Pavlakovic, M. Evans, K. Vine, and M. Lowe, "Long range inspection of rail using guided waves-field experience," in *Proceedings of the 16th World Conference on Non-Destructive Testing, Montreal, Canada, 2004*.
- [32] P. Wilcox, B. Pavlakovic, M. Evans, K. Vine, P. Cawley, M. Lowe, and D. Alleyne, "Long Range Inspection of Rail Using Guided Waves," *AIP Conference Proceedings*, vol. 657, pp. 236-243, 2003.
- [33] I. Bartoli, F. Lanza di Scalea, M. Fateh, and E. Viola, "Modeling guided wave propagation with application to the long-range defect detection in railroad tracks," *NDT & E International*, vol. 38, pp. 325-334, 2005.
- [34] F. Lanza di Scalea, P. Rizzo, S. Coccia, I. Bartoli, M. Fateh, E. Viola, and G. Pascale, "Non-contact ultrasonic inspection of rails and signal processing for automatic defect detection and classification," *Insight-Non-Destructive Testing and Condition Monitoring*, vol. 47, pp. 346-353, 2005.
- [35] J. D. McNamara, F. L. di Scalea, and M. Fateh, "Automatic defect classification in long-range ultrasonic rail inspection using a support vector machine-based smart system," *Insight - Non-Destructive Testing and Condition Monitoring*, vol. 46, pp. 331-337, 2004.

- [36] S. Peter, "Eddy Current," in *Nondestructive Evaluation*, ed: CRC Press, 2002.
- [37] R. Pohl, A. Erhard, H. J. Montag, H. M. Thomas, and H. Wüstenberg, "NDT techniques for railroad wheel and gauge corner inspection," *NDT & E International*, vol. 37, pp. 89-94, 2004.
- [38] M. Bentoumi, P. Aknin, and G. Bloch, "On-line rail defect diagnosis with differential eddy current probes and specific detection processing," *The European Physical Journal Applied Physics*, vol. 23, pp. 227-233, 2003.
- [39] P. Rainer, B. BAM, and D. Germany Ronald KRULL, "A new Eddy Current Instrument in a Grinding Train."
- [40] H. Thomas, M. Junger, H. Hintze, R. Krull, and S. Rühle, "Pioneering inspection of railroad rails with eddy currents," in *Proceedings of the 15th World Conference on Non-Destructive Testing, Rome, Italy, 2000*.
- [41] M. Junger, H. Thomas, R. Krull, and S. Rühle, "The potential of eddy current technology regarding railroad inspection and its implementation," in *the Proceedings of the 16th World Conference on Non-Destructive Testing, Montreal, Canada, 2004*.
- [42] H. Thomas, T. Heckel, and G. Hanspach, "Advantage of a combined ultrasonic and eddy current examination for railway inspection trains," *Insight-Non-Destructive Testing and Condition Monitoring*, vol. 49, pp. 341-344, 2007.
- [43] R. Smid, A. Docekal, and M. Kreidl, "Automated classification of eddy current signatures during manual inspection," *NDT & E International*, vol. 38, pp. 462-470, 2005.
- [44] D. E. Bray and R. K. Stanley, *Nondestructive evaluation: a tool in design, manufacturing, and service*: CRC press, 1997.
- [45] K. Miya, "Recent advancement of electromagnetic nondestructive inspection technology in Japan," *Magnetics, IEEE Transactions on*, vol. 38, pp. 321-326, 2002.
- [46] J. Drury and N. Pearson, "Corrosion detection in Ferrite Steels using Magnetic Flux Leakage," in *Proceedings of Magnetics in Non-Destructive Testing, 2005*, pp. 14-19.
- [47] D. C. Jiles, "Review of magnetic methods for nondestructive evaluation (Part 2)," *NDT International*, vol. 23, pp. 83-92, 1990.
- [48] M. Afzal and S. Udpa, "Advanced signal processing of magnetic flux leakage data obtained from seamless gas pipeline," *Ndt & E International*, vol. 35, pp. 449-457, 2002.

- [49] Y. Li, G. Y. Tian, and S. Ward, "Numerical simulation on magnetic flux leakage evaluation at high speed," *NDT & E International*, vol. 39, pp. 367-373, 2006.
- [50] D. Minkov and T. Shoji, "Method for sizing of 3-D surface breaking flaws by leakage flux," *NDT & E International*, vol. 31, pp. 317-324, 1998.
- [51] M. Ravan, R. K. Amineh, S. Koziel, N. K. Nikolova, and J. P. Reilly, "Sizing of 3-D arbitrary defects using magnetic flux leakage measurements," *Magnetics, IEEE Transactions on*, vol. 46, pp. 1024-1033, 2010.
- [52] R. Collins, "The development of the ACPD and ACFM techniques at UCL," *Nondestructive Testing of Materials*, vol. 8, pp. 65-74, 1995.
- [53] M. Lugg, D. Topp, and M. Keynes, "Recent developments and applications of the ACFM inspection method and ACSM stress measurement method," in *Proceedings of ECNDT*, Berlin, Germany, 2006.
- [54] M. P. Papaelias, M. C. Lugg, C. Roberts, and C. L. Davis, "High-speed inspection of rails using ACFM techniques," *NDT & E International*, vol. 42, pp. 328-335, 2009.
- [55] M. P. Papaelias, C. Roberts, C. L. Davis, B. Blakeley, and M. Lugg, "Further developments in high-speed detection of rail rolling contact fatigue using ACFM techniques," *Insight - Non-Destructive Testing and Condition Monitoring*, vol. 52, pp. 358-360, 2010.
- [56] M. P. Papaelias, C. Roberts, C. L. Davis, B. Blakeley, and M. Lugg, "High-speed inspection of rolling contact fatigue in rails using ACFM sensors," *Insight - Non-Destructive Testing and Condition Monitoring*, vol. 51, pp. 366-369, 2009.
- [57] A. M. Lewis, D. H. Michael, M. C. Lugg, and R. Collins, "Thin-skin electromagnetic fields around surface-breaking cracks in metals," *Journal of Applied Physics*, vol. 64, pp. 3777-3784, 1988.
- [58] D. H. Michael, A. M. Lewis, M. McIver, and R. Collins, "Thin-Skin Electromagnetic Fields in the Neighbourhood of Surface-Breaking Cracks in Metals," *Proceedings of the Royal Society of London. Series A: Mathematical and Physical Sciences*, vol. 434, pp. 587-603, 1991.
- [59] R. K. Amineh, M. Ravan, S. Sadeghi, and R. Moini, "Removal of probe liftoff effects on crack detection and sizing in metals by the AC field measurement technique," *Magnetics, IEEE Transactions on*, vol. 44, pp. 2066-2073, 2008.
- [60] R. K. Amineh, M. Ravan, S. H. H. Sadeghi, and R. Moini, "Using AC field measurement data at an arbitrary liftoff distance to size long surface-breaking cracks in ferrous metals," *NDT & E International*, vol. 41, pp. 169-177, 2008.

- [61] S. H. H. Sadeghi and D. Mirshekar-Syahkal, "Surface potential distributions due to eddy currents around long cracks in metals, induced by U-shaped current-carrying wires," *Magnetics, IEEE Transactions on*, vol. 27, pp. 674-679, 1991.
- [62] M. Ravan, S. H. H. Sadeghi, and R. Moini, "Neural network approach for determination of fatigue crack depth profile in a metal, using alternating current field measurement data," *Science, Measurement & Technology, IET*, vol. 2, pp. 32-38, 2008.
- [63] R. P. R. Hasanzadeh, S. H. H. Sadeghi, M. Ravan, A. R. Moghaddamjoo, and R. Moini, "A fuzzy alignment approach to sizing surface cracks by the AC field measurement technique," *NDT & E International*, vol. 44, pp. 75-83, 2011.
- [64] G. L. Nicholson, A. G. Kostryzhev, X. J. Hao, and C. L. Davis, "Modelling and experimental measurements of idealised and light-moderate RCF cracks in rails using an ACFM sensor," *NDT & E International*, vol. 44, pp. 427-437, 2011.
- [65] G. L. Nicholson, A. G. Kostryzhev, H. Rowshandel, M. P. Papaelias, C. L. Davis, and C. Roberts, "Sizing and tomography of rolling contact fatigue cracks in rails using NDT technology - potential for high speed application," in *Proceedings of the 9th World Conference on Railway Research*, Lille, France, 2011.
- [66] M. Howitt, "Bombardier brings ACFM into the rail industry," *Insight*, vol. 44, pp. 379-382, 2002.
- [67] M. Papaelias, S. Kerkyras, F. Papaelias, and K. Graham, "The future of rail inspection technology and the INTERAIL FP7 project."
- [68] B. Bridge, H. Leon Rodriguez, S. Mondal, and T. Sattar, "Field trials of a cell of climbing cooperating robots for fast and flexible manufacturing of large scale engineering structures," in *Proc. of the 12th International Conference on Climbing and Walking Robots and the Support Technologies for Mobile Machines (CLAWAR)*, Istanbul, Turkey, 2009.
- [69] B. Bridge, T. Sattar, S. Chen, and A. Khalid, "On the design of multi-task, compact, climbing robotic NDT systems for remote operation on large surfaces and in hazardous environments," *Nondestructive Testing and Evaluation*, vol. 13, pp. 85-111, 1997.
- [70] B. Bridge, T. Sattar, and H. Leon, "Climbing robot cell for fast and flexible manufacture of large scale structures," in *22nd International Conference, CAD/CAM Robotics and Factories of the Future (CARS & FOF 2006)*, 2006, pp. 584-597.

- [71] T. Kang, H. Kim, T. Son, and H. Choi, "Design of quadruped walking and climbing robot," in *Intelligent Robots and Systems, 2003.(IROS 2003). Proceedings. 2003 IEEE/RSJ International Conference on, 2003*, pp. 619-624.
- [72] G. La Rosa, M. Messina, G. Muscato, and R. Sinatra, "A low-cost lightweight climbing robot for the inspection of vertical surfaces," *Mechatronics*, vol. 12, pp. 71-96, 2002.
- [73] S. Mondal, T. Sattar, and B. Bridge, "Tofd inspection of v-groove butt welds on the hull of a container ship with a magnetically adhering wall climbing robot," in *5th International Conference on Climbing and Walking Robots and the Support Technologies for Mobile Machines, 2002*, pp. 955-961.
- [74] T. Sattar, M. Alaoui, S. Chen, and B. Bridge, "A magnetically adhering wall climbing robot to perform continuous welding of long seams and non-destructively test the welds on the hull of a container ship," in *Proceedings of the 8th IEEE Conference on Mechatronics and Machine Vision in Practice, Hong Kong, 27-29 August, 2001*, pp. 408-14.
- [75] T. Sattar, Z. Zhao, J. Feng, B. Bridge, S. Mondal, and S. Chen, "Internal in-service inspection of the floor and walls of oil, petroleum, and chemical storage tanks with a mobile robot," in *5th International Conference on Climbing and Walking Robots and the Support Technologies for Mobile Machines, 2002*, p. 380.
- [76] T. P. Sattar and A.-A. Brenner, "Robotic system for inspection of test objects with unknown geometry using NDT methods," *Industrial Robot: An International Journal*, vol. 36, pp. 340-343, 2009.
- [77] T. P. Sattar, H. E. Leon-Rodriguez, and J. Shang, "Amphibious NDT Robots," in *Climbing & Walking Robots, Towards New Applications*, H. Zhang, Ed., ed Vienna, Austria: Itech Education and Publishing, 2007, p. 546.
- [78] T. P. Sattar, H. L. Rodriguez, and B. Bridge, "Climbing ring robot for inspection of offshore wind turbines," *Industrial Robot: An International Journal*, vol. 36, pp. 326-330, 2009.
- [79] T. P. Sattar, H. L. Rodriguez, J. Shang, and B. Bridge, "Automated NDT of floating production storage oil tanks with a swimming and climbing robot," in *Climbing and Walking Robots*, ed: Springer, 2006, pp. 935-942.
- [80] J. Shang, B. Bridge, T. Sattar, S. Mondal, and A. Brenner, "Development of a climbing robot for inspection of long weld lines," *Industrial Robot: An International Journal*, vol. 35, pp. 217-223, 2008.
- [81] J. Shang, B. Bridge, T. Sattar, S. Mondal, and A. Brenner, "Development of a Climbing Robot for Weld Inspection," in *Proceedings of the 10th International Conference on*

- Climbing and Walking Robots and Supporting Technologies for Mobile Machines*, 2007.
- [82] J. Shang, T. Sattar, S. Chen, and B. Bridge, "Design of a climbing robot for inspecting aircraft wings and fuselage," *Industrial Robot: An International Journal*, vol. 34, pp. 495-502, 2007.
- [83] I. N. Ismail, A. Anuar, K. S. M. Sahari, M. Z. Baharuddin, M. Fairuz, A. Jalal, and J. M. Saad, "Development of in-pipe inspection robot: A review," in *Sustainable Utilization and Development in Engineering and Technology (STUDENT), 2012 IEEE Conference on*, 2012, pp. 310-315.
- [84] H. R. Choi and S. M. Ryew, "Robotic system with active steering capability for internal inspection of urban gas pipelines," *Mechatronics*, vol. 12, pp. 713-736, 2002.
- [85] M. Miller, B. Mi, A. Kita, and I. C. Ume, "Development of automated real-time data acquisition system for robotic weld quality monitoring," *Mechatronics*, vol. 12, pp. 1259-1269, 2002.
- [86] X. E. Gros, *Applications of NDT data fusion*: Springer, 2001.
- [87] F. L. di Scalea and J. McNamara, "Ultrasonic NDE of railroad tracks: air-coupled cross-sectional inspection and long-range inspection," *Insight-Non-Destructive Testing and Condition Monitoring*, vol. 45, pp. 394-401, 2003.
- [88] G. Y. Tian, A. Sophian, D. Taylor, and J. Rudlin, "Pulsed eddy current system for dynamic inspection of defects," *Insight - Non-Destructive Testing and Condition Monitoring*, vol. 46, pp. 256-259, 2004.
- [89] H. A. Toliyat, K. Abbaszadeh, M. M. Rahimian, and L. E. Olson, "Rail defect diagnosis using wavelet packet decomposition," *Industry Applications, IEEE Transactions on*, vol. 39, pp. 1454-1461, 2003.
- [90] K. Abbaszadeh, M. Rahimian, H. Toliyat, and L. Olson, "Rail defect diagnosis using wavelet packet decomposition," in *Industry Applications Conference, 2002. 37th IAS Annual Meeting. Conference Record of the*, 2002, pp. 478-484.
- [91] M. Ravan, S. H. H. Sadeghi, and R. Moini, "Using a wavelet network for reconstruction of fatigue crack depth profile from AC field measurement signals," *NDT & E International*, vol. 40, pp. 537-544, 2007.
- [92] M. Negnevitsky, *Artificial intelligence: a guide to intelligent systems*: Addison-Wesley Longman, 2005.

- [93] K. Hamada, T. Baba, K. i. Sato, and M. Yufu, "Hybridizing a genetic algorithm with rule-based reasoning for production planning," *IEEE Expert*, vol. 10, pp. 60-67, 1995.
- [94] L. Sabourin and F. Villeneuve, "OMEGA, an expert CAPP system," *Advances in Engineering Software*, vol. 25, pp. 51-59, 1996.
- [95] D. Mulvaney and C. Bristow, "A Rule - based Extension to the C++ Language," *Software: Practice and Experience*, vol. 27, pp. 747-761, 1997.
- [96] I. Hatzilygeroudis and J. Prentzas, "Using a hybrid rule-based approach in developing an intelligent tutoring system with knowledge acquisition and update capabilities," *Expert systems with applications*, vol. 26, pp. 477-492, 2004.
- [97] D. Leung and J. Romagnoli, "Dynamic probabilistic model-based expert system for fault diagnosis," *Computers & Chemical Engineering*, vol. 24, pp. 2473-2492, 2000.
- [98] J.-H. Kim, H.-S. Shim, H.-S. Kim, M.-J. Jung, I.-H. Choi, and J.-O. Kim, "A cooperative multi-agent system and its real time application to robot soccer," in *Robotics and Automation, 1997. Proceedings., 1997 IEEE International Conference on*, 1997, pp. 638-643.
- [99] TSC Inspection Systems. (2009). *ACFM pencil probe*.
- [100] P. Brockerhoff and M. Schulz, "Direct measuring position encoder for axial transversal flux machine," in *Energy Conversion Congress and Exposition (ECCE), 2010 IEEE*, 2010, pp. 1766-1771.
- [101] R. M. Kennel, "Encoders for simultaneous sensing of position and speed in electrical drives with digital control," in *Industry Applications Conference, 2005. Fourtieth IAS Annual Meeting. Conference Record of the 2005*, 2005, pp. 731-736 Vol. 1.
- [102] B. He, W. Danwei, P. Minhtuan, and Y. Tieniu, "GPS/encoder based precise navigation for a 4WS mobile robot," in *Control, Automation, Robotics and Vision, 2002. ICARCV 2002. 7th International Conference on*, 2002, pp. 1256-1261 vol.3.
- [103] J. J. Blakley, "Two-dimensional position sensing using absolute-type encoder scheme employing pseudorandom binary arrays," *Electronics Letters*, vol. 36, pp. 1277-1278, 2000.
- [104] L. Haoxiang, W. Ying, and C. W. de Silva, "Mobile robot localization and object pose estimation using optical encoder, vision and laser sensors," in *Automation and Logistics, 2008. ICAL 2008. IEEE International Conference on*, 2008, pp. 617-622.
- [105] H. Bistry, D. Westhoff, and Z. Jianwei, "A smart interface-unit for the integration of pre-processed laser range measurements into robotic systems and sensor networks,"

- in *Intelligent Robots and Systems, 2007. IROS 2007. IEEE/RSJ International Conference on, 2007*, pp. 358-363.
- [106] Micro-Epsilon. (2010). *ILD 1302-20*.
- [107] Y. Sakamoto, K. Kodaka, T. Ebinuma, K. Fujii, and S. Sugano, "Active-localization methods for mobile robots in a coarsely structured environment with floor-embedded RFID tags and indoor GPS," in *Mechatronics and Automation (ICMA), 2012 International Conference on, 2012*, pp. 539-545.
- [108] Michrochip Technology Inc, "Measuring Speed and Position with the QEI Module," 2005.
- [109] J. G. Ziegler and N. B. Nichols, "Optimum Settings for Automatic Controllers," *Journal of Dynamic Systems, Measurement, and Control*, vol. 115, pp. 220-222, 1993.
- [110] F. J. Franklin, J. E. Garnham, D. I. Fletcher, C. L. Davis, and A. Kapoor, "Modelling rail steel microstructure and its effect on crack initiation," *Wear*, vol. 265, pp. 1332-1341, 2008.
- [111] G. L. Nicholson, 2011, "Study of effect of angle offset between ACFM sensor and RCF crack," University of Birmingham, Birmingham Centre for Railway Research and Education, unpublished.
- [112] A. Raine and M. Lugg, "A review of the alternating current field measurement inspection technique," *Sensor Review*, vol. 19, pp. 207-213, 1999.
- [113] G. L. Nicholson, H. Rowshandel, X. J. Hao, and C. L. Davis, "Measurement and modelling of ACFM response to multiple RCF cracks in rail and wheels," *Ironmaking & Steelmaking*, vol. 40, pp. 87-91, 2013.
- [114] A. H. Salemi, S. H. H. Sadeghi, and R. Moini, "The effect of sensor lift-off on crack depth measurement by the Surface Magnetic Field Measurement technique," *AIP Conference Proceedings*, vol. 615, pp. 977-983, 2002.
- [115] O. Zahran, H. Kasban, M. El-Kordy, and F. E. A. El-Samie, "Automatic weld defect identification from radiographic images," *NDT & E International*, vol. 57, pp. 26-35, 2013.
- [116] H. Yazid, H. Arof, H. Yazid, S. Ahmad, A. A. Mohamed, and F. Ahmad, "Discontinuities detection in welded joints based on inverse surface thresholding," *NDT & E International*, vol. 44, pp. 563-570, 2011.

- [117] H. Kasban, O. Zahran, H. Arafa, M. El-Kordy, S. M. S. Elaraby, and F. E. Abd El-Samie, "Welding defect detection from radiography images with a cepstral approach," *NDT & E International*, vol. 44, pp. 226-231, 2011.
- [118] J. Zapata, R. Vilar, and R. Ruiz, "An adaptive-network-based fuzzy inference system for classification of welding defects," *NDT & E International*, vol. 43, pp. 191-199, 2010.
- [119] J. P. Yun, S. Choi, J.-W. Kim, and S. W. Kim, "Automatic detection of cracks in raw steel block using Gabor filter optimized by univariate dynamic encoding algorithm for searches (uDEAS)," *NDT & E International*, vol. 42, pp. 389-397, 2009.
- [120] R. Vilar, J. Zapata, and R. Ruiz, "An automatic system of classification of weld defects in radiographic images," *NDT & E International*, vol. 42, pp. 467-476, 2009.
- [121] R. Heriansyah and S. A. R. Abu-Bakar, "Defect detection in thermal image for nondestructive evaluation of petrochemical equipments," *NDT & E International*, vol. 42, pp. 729-740, 2009.
- [122] J. Baili, S. Lahouar, M. Hergli, I. L. Al-Qadi, and K. Besbes, "GPR signal de-noising by discrete wavelet transform," *NDT & E International*, vol. 42, pp. 696-703, 2009.
- [123] Y. Wang, Y. Sun, P. Lv, and H. Wang, "Detection of line weld defects based on multiple thresholds and support vector machine," *NDT & E International*, vol. 41, pp. 517-524, 2008.
- [124] T. D'Orazio, M. Leo, A. Distanto, C. Guaragnella, V. Pianese, and G. Cavaccini, "Automatic ultrasonic inspection for internal defect detection in composite materials," *NDT & E International*, vol. 41, pp. 145-154, 2008.
- [125] H. P. R. Reza, A. H. Rezaie, S. H. H. Sadeghi, M. H. Moradi, and M. Ahmadi, "A density-based fuzzy clustering technique for non-destructive detection of defects in materials," *NDT & E International*, vol. 40, pp. 337-346, 2007.
- [126] Alaknanda, R. S. Anand, and P. Kumar, "Flaw detection in radiographic weld images using morphological approach," *NDT & E International*, vol. 39, pp. 29-33, 2006.
- [127] Y. Sun, P. Bai, H.-y. Sun, and P. Zhou, "Real-time automatic detection of weld defects in steel pipe," *NDT & E International*, vol. 38, pp. 522-528, 2005.
- [128] F. Pernkopf and P. O'Leary, "Image acquisition techniques for automatic visual inspection of metallic surfaces," *NDT & E International*, vol. 36, pp. 609-617, 2003.
- [129] G. Wang and T. W. Liao, "Automatic identification of different types of welding defects in radiographic images," *NDT & E International*, vol. 35, pp. 519-528, 2002.

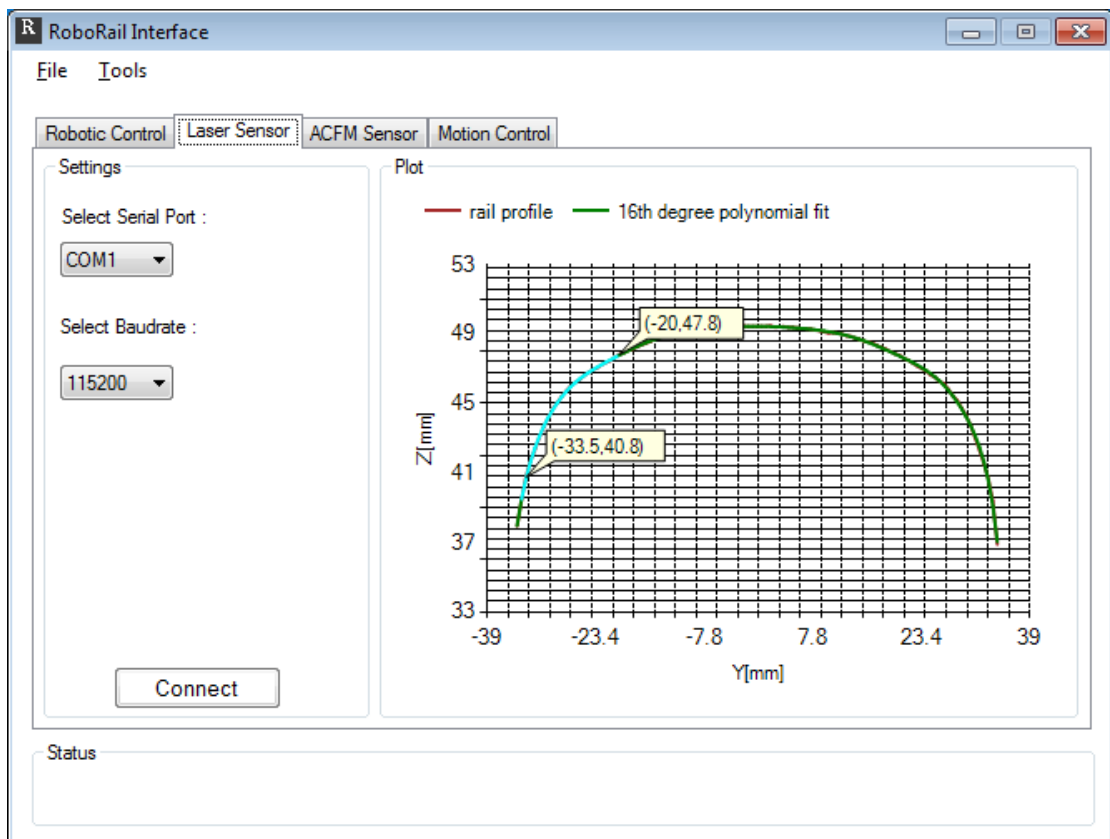
- [130] A. C. Legrand, F. Meriaudeau, and P. Gorria, "Active infrared non-destructive testing for glue occlusion detection within plastic lids," *NDT & E International*, vol. 35, pp. 177-187, 2002.
- [131] F. Lingvall and T. Stepinski, "Automatic detecting and classifying defects during eddy current inspection of riveted lap-joints," *NDT & E International*, vol. 33, pp. 47-55, 2000.
- [132] J. Moysan, G. Corneloup, and T. Sollier, "Adapting an ultrasonic image threshold method to eddy current images and defining a validation domain of the thresholding method," *NDT & E International*, vol. 32, pp. 79-84, 1999.
- [133] T. W. Liao and Y. Li, "An automated radiographic NDT system for weld inspection: Part II—Flaw detection," *NDT & E International*, vol. 31, pp. 183-192, 1998.
- [134] J. Moysan, G. Corneloup, I. Magnin, and P. Benoist, "Definition of a new measure based on the co-occurrence matrix for the threshold selection of ultrasonic images in the nuclear NDT field," *NDT & E International*, vol. 25, p. 219, 1992.
- [135] P. Weston, C. Ling, C. Roberts, C. Goodman, P. Li, and R. Goodall, "Monitoring vertical track irregularity from in-service railway vehicles," *Proceedings of the Institution of Mechanical Engineers, Part F: Journal of Rail and Rapid Transit*, vol. 221, pp. 75-88, 2007.
- [136] H. Rowshandel, G. L. Nicholson, C. L. Davis, and C. Roberts, "A robotic approach for NDT of RCF cracks in rails using an ACFM sensor," *Insight - Non-Destructive Testing and Condition Monitoring*, vol. 53, pp. 368-376, 2011.

Publications

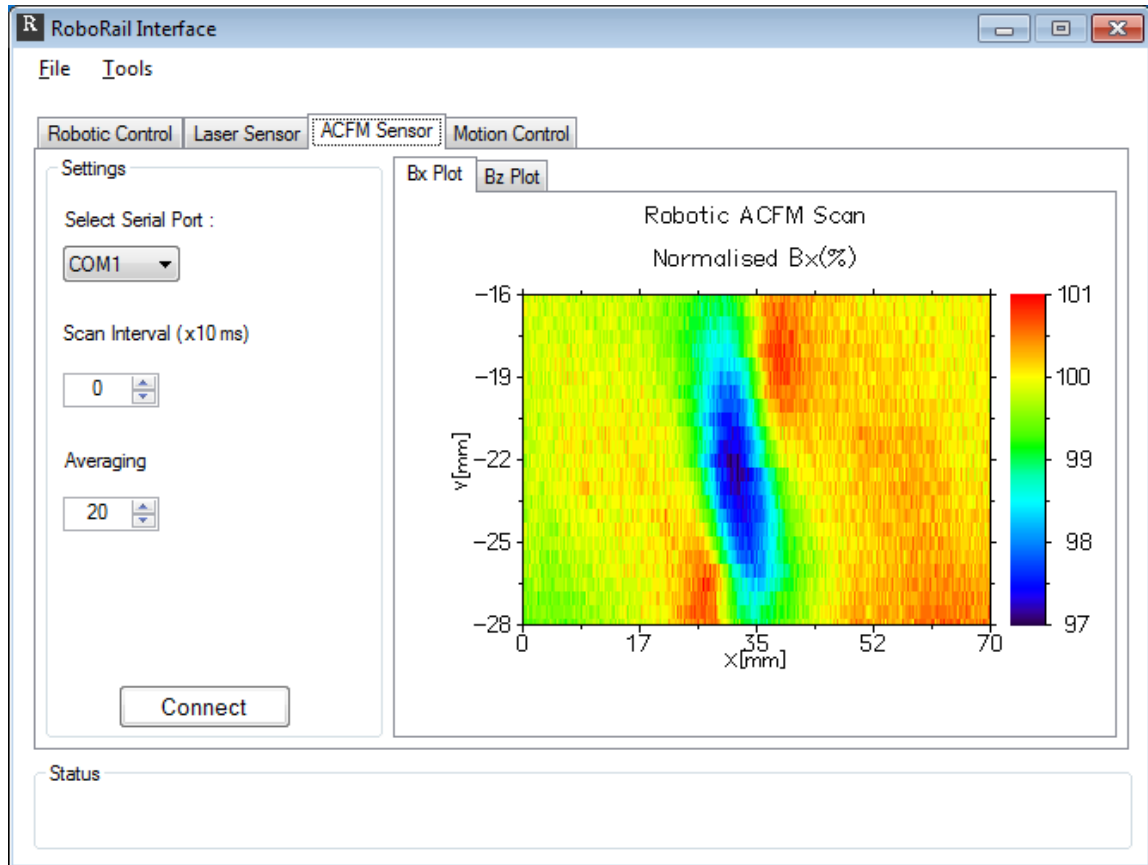
1. **H. Rowshandel**, G. L. Nicholson, C. L. Davis, and C. Roberts, "An integrated robotic system for automatic detection and characterisation of rolling contact fatigue cracks in rails using an alternating current field measurement sensor," *Proceedings of the Institution of Mechanical Engineers, Part F: Journal of Rail and Rapid Transit*, 2013.
2. G. L. Nicholson, **H. Rowshandel**, X. J. Hao, and C. L. Davis, "Measurement and modelling of ACFM response to multiple RCF cracks in rail and wheels," *Ironmaking & Steelmaking*, vol. 40, pp. 87-91, 2013.
3. **H. Rowshandel**, G. L. Nicholson, C. L. Davis, and C. Roberts, "A robotic system for non-destructive evaluation of RCF cracks in rails using an ACFM sensor," in *5th IET Conference on Railway Condition Monitoring and Non-Destructive Testing (RCM 2011)*, 2011, pp. 1-6.
4. **H. Rowshandel**, G. L. Nicholson, C. L. Davis, and C. Roberts, "A robotic approach for NDT of RCF cracks in rails using an ACFM sensor," *Insight - Non-Destructive Testing and Condition Monitoring*, vol. 53, pp. 368-376, 2011.
5. **H. Rowshandel**, M. Papaelias, C. Roberts, and C. Davis, "Development of autonomous ACFM rail inspection techniques," *Insight - Non-Destructive Testing and Condition Monitoring*, vol. 53, pp. 85-89, 2011.

Appendix. Screenshot of the IUI Software

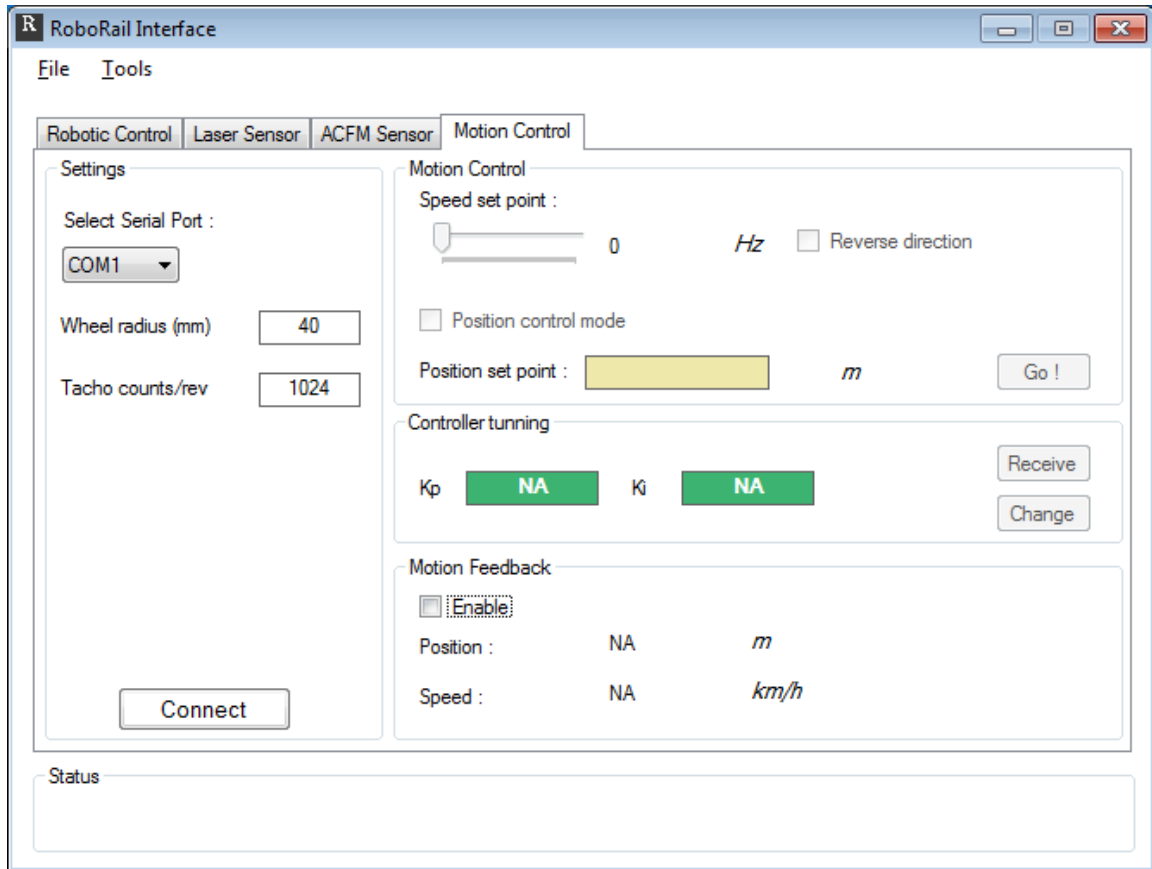
Laser Sensor Interface



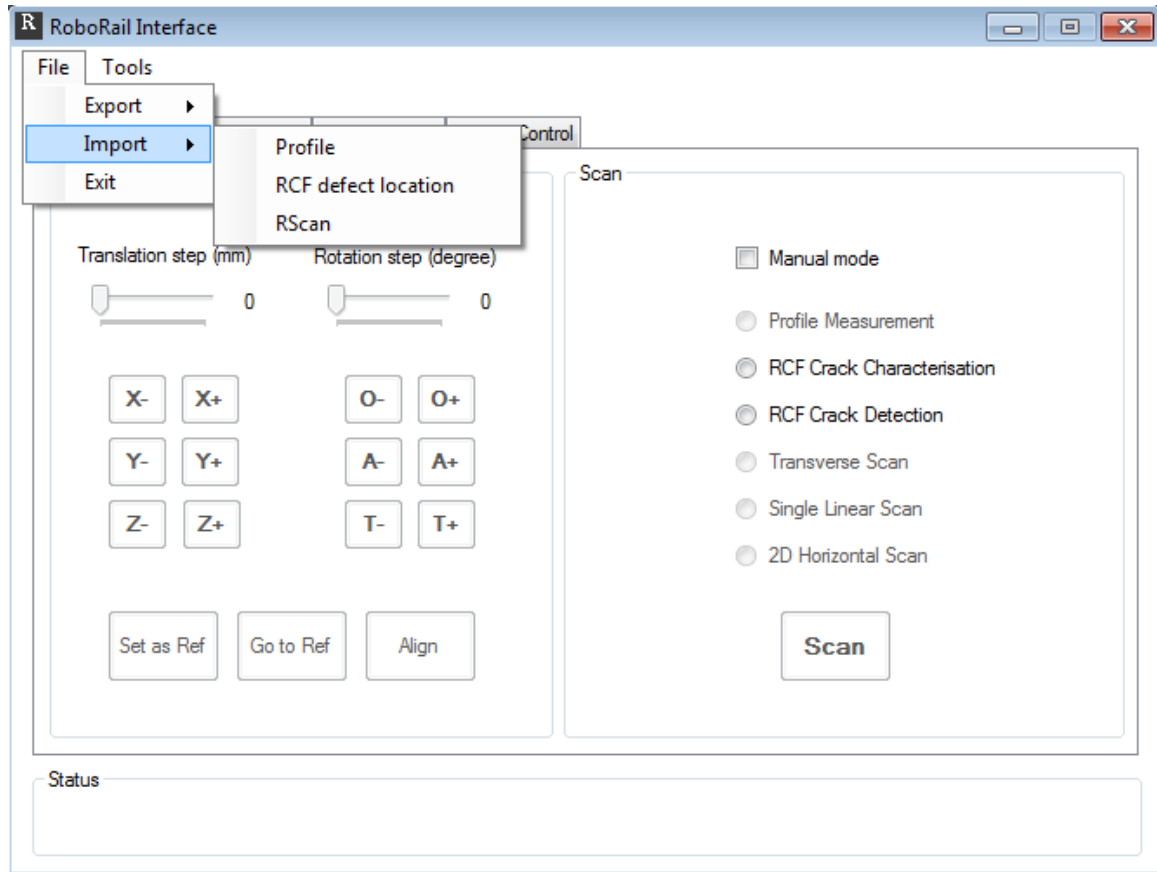
ACFM Sensor Interface



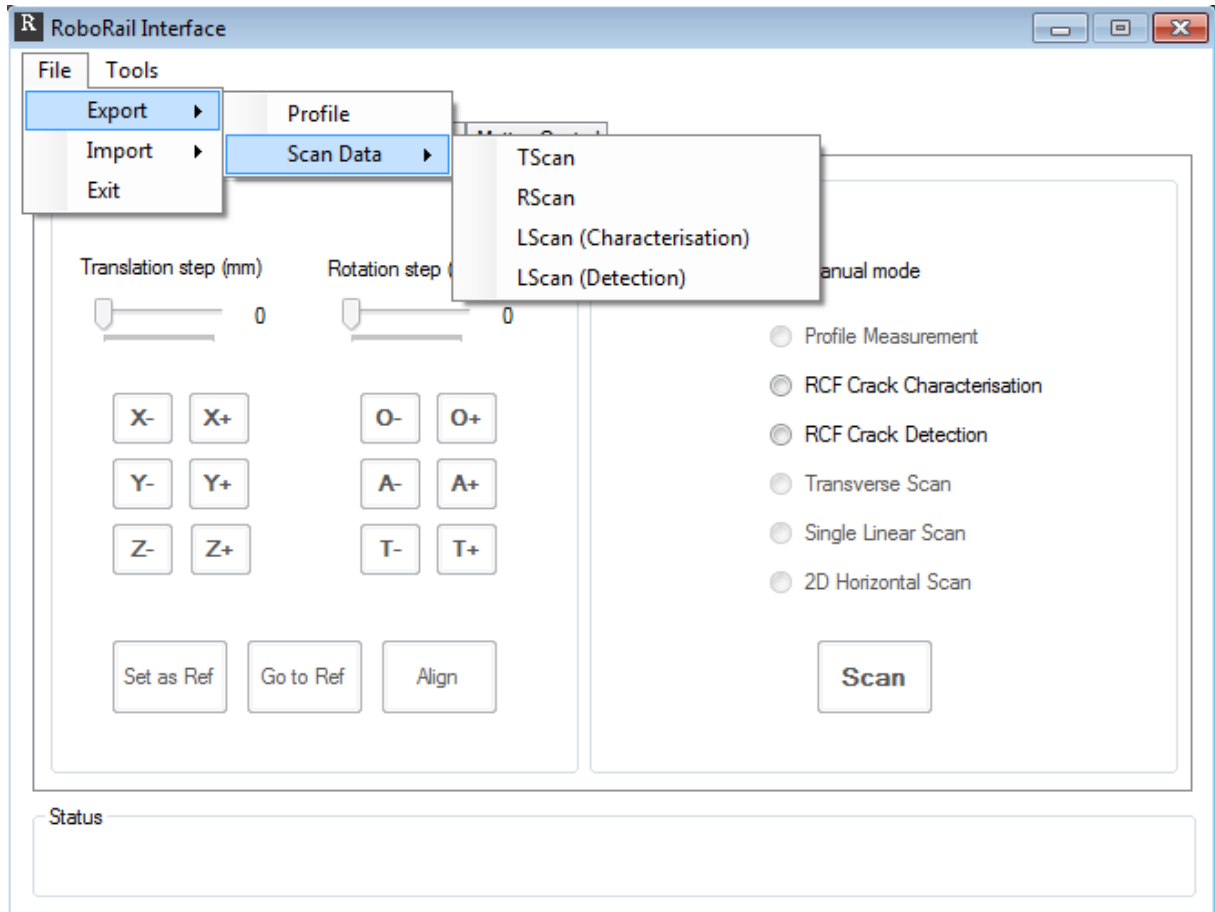
Motion Controller Interface



Import Utilities



Export Utilities



Auxiliary Tools

